

PhD Thesis

Polarization dependence of optical absorption and
Raman spectra for atomic layer materials

(原子層物質の光吸収及びラマンスペクトルの偏光特性)

Yuki Tatsumi

Department of Physics, Graduate School of Science
Tohoku University

September, 2017

Acknowledgements

I am extremely grateful to Prof. Riichiro Saito for giving me the direction of research. His education not only for research, but also the department as a member of laboratory is very efficient to continue my life in any environment. I also thank a lot to Prof. Wataru Izumida who is the supervisor of me in my master course. My basic point to do the research is constructed by his kind direction. I also thank to the collaborator of experimenters in MIT, late Prof. Mildred Dresselhaus, Dr. Xi Ling, Ms. Shengxi Fuang, and Ms. Lin Zhou. Especially the discussion with Prof. Dresselhaus when she visited Sendai in 2016 is one of my great memory in my life. I also thank to the collaborator of theoretical work, Prof. Teng Yang, Prof. Lichang Yin, and Prof. Huaihong Guo. The discussion with them is effective very much for my progress of the research. I also would like to say thank you to the members in the laboratory, Prof. Kentaro Sato, Prof. A. R. T. Nugraha, Dr. Rin Okuyama, Dr. Tomoaki Kaneko, Dr. E. H. Hasdeo, Dr. P. Ayria, Mr. Masashi Mizuno, Mr. Toshiya Shirakura, Mr. Yuya Inoue, Mr. M. S. Ukhtary, Mr. N. T. Hung, Mr. P. Tapsanit, Mr. K. Ghalamkari, Mr. Takeshi Shirosaki, Mr. F. Pratama, Mr. Daiki Sato, and Mr. Yuya Iwasaki. Especially, I learned a lot of things from two Indonesian members, Prof. Nugraha and Dr. Hasdeo. They helped me a lot and I can say they are emotional support of me in the laboratory. I also thank to the secretary in the laboratory, Ms. Yoko Wako, Ms. Setsuko Sumino, Ms. Mari Sato, and Ms. Junko Sasaki. Finally, I also thank to my family to support me a lot.

Abstract

Atomic layer materials are two-dimensional (2D) materials which show unique optical properties due to their in-plane structures. One of the promised applications of 2D materials are optoelectronic devices due to their transparency and flexibility. In this thesis, we discuss the behavior of optical absorption and Raman spectra for 2D materials by using linearly- or circularly-polarized light.

Transition metal dichalcogenides (TMDs) with hexagonal lattice structure constructed by metal and chalcogen atoms, one of the atomic layer materials, have two independent valleys called K and K' which are the region of the small energy near the local minimum of conduction band in k -space at the corners of the hexagonal Brillouin zone. By using left-handed (σ_+) and right-handed (σ_-) circular polarized light with the helicity +1 and -1, respectively, we can control the optical transitions at the K and K' valleys. The σ_+ (σ_-) light excites the electron at the K (K') valley which is known as the optical valley polarization. The valley polarization can be observed only in the material without inversion symmetry because optical matrix elements at the K and K' point must be the same if there is inversion symmetry in the material. Graphene, which has inversion symmetry, thus does not have valley polarization even though graphene also has hexagonal lattice structure similar with TMDs. Such a valley-selective optical transition by circular polarized light has a potential for the application to utilize the degree of the freedom of valley for devices, or the so-called "valleytronics". According to the two band $\mathbf{k} \cdot \mathbf{p}$ Hamiltonian model [Phys. Rev. Lett. 108, 196802 (2012)], valley polarization monotonically decreases with distance from K or K' point. However, such a simple model cannot express the complicated electronic structure of TMDs and the valley polarization for high energy region is not clear. We need first-principles calculations to quantitatively evaluate the valley polarization for the complicated energy bands. In order to utilize the valley polarization for the applications, 100 % valley polarization with strong intensity is required ideally. We find the optimum condition to obtain the good condition of optical valley polarization by tuning the laser excitation energy which becomes one of the subjects of this thesis.

Unique optical properties in 2D materials can be also found in Raman spectroscopy which is a conventional technique to characterize materials. Raman scattering is an inelastic scattering of light. The energy difference between the incident and scattered light, known as the Raman shift, corresponds to the emission or absorption of phonon. From the Raman spectra, we can obtain rich information of the material, such as its electronic structure, crystal structure, vibration, defect, and so on. In this thesis, we focus on the Raman spectra that are obtained by shedding linearly- or circularly-polarized light. In gallium telluride (GaTe) and black phosphorus (BP) which have lower symmetry than graphene, we can observe the characteristic polar plot of Raman intensity for the direction of polarization, depending on the phonon modes (A_g or B_g

mode), in which A_g mode has a polarization for x- or y-direction while B_g mode has a polarization for the direction of 45° from x- or y-direction. This phenomenon is explained by Raman tensor which is a classical theory based on the symmetry of phonon. However, it is also reported that the Raman spectra as a function of the polarization direction for linearly-polarized light depend on the sample thickness and laser excitation energy, which cannot be explained by Raman tensor. We thus give the explanation of such a problem in this thesis. Furthermore, Chen *et al.* [Nano Lett. 15, 2526 (2015)] experimentally reported that some phonon modes in TMDs change the helicity of photon after the Raman scattering by using the circularly-polarized light (helicity-resolved Raman spectroscopy). The IMC (in-plane vibration of metal and chalcogen atoms) mode at $\sim 390 \text{ cm}^{-1}$ changes the helicity while OC (out-of-plane vibration of chalcogen atom) mode $\sim 410 \text{ cm}^{-1}$ does not change the helicity in Raman scattering process for monolayer MoS₂. Such a helicity-selection rule is basically explained by the Raman tensor. However, Raman tensor cannot explain the laser energy dependence of Raman intensity nor the mechanism of helicity-resolved Raman spectra. Furthermore, according to the discussion of the conservation of angular momentum [Phys. Rev. Lett. 115, 115502 (2015)], only the degenerate phonon mode can change the helicity of photon by exchanging the angular momentum to the phonon since the degenerate phonon can have the angular momentum by expressing the eigen vector as the superposition of degenerate eigen vectors. We are interested in the behavior of helicity-resolved Raman spectra when we lift the degeneracy by strain-induction. Purposes of this thesis are as follows: (1) to investigate the valley polarization of TMDs as a function of the excitation laser energy, and (2) to explain the observed Raman spectra of GaTe and BP for linearly-polarized light which depend on the excitation laser energy and the thickness of the sample, (3) to explain the helicity-exchange of photon in helicity-resolved Raman spectra in TMDs and strain-induced graphene. To investigate the behavior of Raman spectra is essential since Raman spectroscopy is commonly used in the experiment to know the electronic structure of a sample.

In order to calculate the optical valley polarization and Raman spectra in 2D materials, we obtain the electron-photon and electron-phonon matrix elements based on the first-principles calculations. The electron-photon matrix element is given within the dipole approximation by $\mathbf{D}^{fi} \cdot \mathbf{P}_\sigma$ where $\mathbf{D}^{fi} = \langle f | \nabla | i \rangle$ and \mathbf{P}_σ are the dipole vector and the polarization vector with the helicity σ , respectively. We use Quantum Espresso package to obtain the electronic structures and wave functions. For the calculation of the electron-phonon matrix elements, we modify the EPW package and extract the information of the electron-phonon matrix element for the Γ point phonon. Using the electron-photon and electron-phonon matrix elements, we developed a program to calculate first-order resonant Raman spectra for linearly- or circularly-polarized light. The analysis for angle-dependent polarized Raman spectra is also given by the group theory

along with the calculation of transfer matrix and the Raman enhancement factor.

In Chapter 3, we discuss the optical valley polarization of six kinds of TMD materials (MoS₂, MoSe₂, MoTe₂, WS₂, WSe₂, and WTe₂). We firstly show the behavior of dipole vectors near the K and K' points by analytical tight-binding calculation in order to know the origin of the valley polarization. We show that the dipole vector at the K (K') point is written by $(1, -i, 0)$ [$(1, i, 0)$] and couples only with the polarization vector of σ_- (σ_+) light $\mathbf{P}_{\sigma_-} = (1, -i, 0)$ [$\mathbf{P}_{\sigma_+} = (1, i, 0)$] which is the reason why the optical valley polarization appears. From our numerical calculation, we show that the valley polarizations of TMDs do not monotonically decrease by increasing the laser excitation energy E_L , but rather there exist other k -points with strong valley polarization called the Λ and Λ' points at the center of the Γ -K (Γ -K') line. The σ_- (σ_+) light excites the electron around the Λ (Λ') point which is the optical valley polarization. The optical absorption for the energy gap around the Λ point is strong because of the nesting of the energy bands. Thus the advantage of the Λ valley for the optical valley polarization is the strong intensity that we can excite many valley polarized electrons by circular polarized light. On the other hand, the M point at the center of the K-K' line does not have the valley polarization that both σ_- and σ_+ light are absorbed same for all M points. Among the six TMD materials calculated in this thesis, MoS₂ has the strongest nesting effect of the energy bands and thus MoS₂ is the best material to get the largest difference of the intensity between σ_+ and σ_- light for each valley.

In Chapter 4, we discuss the polarized Raman spectroscopy of GaTe and BP. The dependence of the laser excitation energy E_L for polarized Raman intensity in GaTe and BP is understood by considering the electronic structure with the symmetry of wave function and the electron-photon matrix element. The polarization direction of electron-photon matrix element is determined by the symmetry of the wave function and thus the polarization direction of optical absorption and Raman spectra depends on the laser energy since the contribution of energy bands changes if we change the laser energy. In the case of GaTe and BP, the electron-photon matrix elements near the energy gap have x-polarization. The y-polarized electron-photon matrix elements appear for higher energy bands. Therefore, the optical absorption and Raman Ag mode of GaTe and BP have tendencies of x-polarization near the gap energy and the polarization becomes weak if we increase the laser energy. To explain the dependences of the sample thickness for optical absorption and Raman spectra, we also need to consider the interference effect with the substrate. Interference effect of the sample on the substrate is taken into account by using the transfer matrix method and the Raman enhancement factor, and gives the significant contribution to flip the polarization direction in different thickness. The quantitative discussion of polarized Raman spectra should be done by considering symmetry of phonon, laser energy and band structure, and interference effect.

In Chapter 5, we discuss the helicity-resolved Raman spectra of TMDs and strain-induced graphene. Our calculated results for monolayer MoS₂ reproduce the helicity-selection rule, in which the IMC (OC) mode changes (does not change) the helicity, as reported by Chen and co-workers. Raman intensity becomes strong around the gap energy of the Λ point because of the nesting of the energy bands and furthermore, IMC mode is more enhanced for the gap energy of the M point and OC modes is more enhanced for the gap energy of the Λ point. This can be understood by the existence of valley polarization, that is, the optical transition around the Λ point has optical valley polarization which only σ_- light can be absorbed or scattered, and thus the helicity-conserving mode is only enhanced. On the other hand, the M point does not have the valley polarization which both σ_- and σ_+ light can be absorbed and scattered, and thus helicity-changing Raman peak is enhanced. From our numerical calculation, our results also show that the helicity-exchange occurs in the G band which is the typical Raman peak of graphene. G band is degenerate mode and helicity-changing is in good agreement with the conservation of angular momentum. The degeneracy of G band can be lifted to G^+ and G^- bands by uniaxial strain and we investigate the behavior of helicity-resolved Raman spectra of strain-induced graphene. By the numerical calculation, we found that the G^+ band keeps the selection rule same with G band which changes the helicity of light. However, G^- band changes the helicity-selection rule with increasing the strain from helicity-changing to helicity-conserving. The helicity-changing in nondegenerate G^+ or G^- band is inconsistent with the conservation of angular momentum if we assume that the angular momentum of photon is exchanged to phonon. However, we insist that the conservation of angular momentum can be broken since the crystal only has discrete rotational symmetry and angular momentum would be able to exchange to the rotation around the center of mass. This can be confirmed by experiments for strain-induced graphene or BP which has same symmetry with strain-induced graphene.

Contents

1	Introduction	1
1.1	Purposes of the study	1
1.2	Organization of thesis	2
1.3	Background	2
1.3.1	Rise of atomic layer materials	2
1.3.2	Optical valley polarization of TMDs	5
1.3.3	Polarized and helicity-resolved Raman spectroscopy in atomic layer materials	11
2	Methods to calculate optical absorption and Raman spectra	23
2.1	Time-dependent perturbation theory	23
2.1.1	Time-dependent perturbation theory	23
2.1.2	Time-dependent periodic perturbation	26
2.1.3	Second- and third-order time-dependent perturbation theory	27
2.2	Electron-photon interaction	29
2.2.1	Derivation of electron-photon matrix element	30
2.2.2	Polarization vector (the Jones vector)	32
2.3	Optical absorption	32
2.3.1	Absorption coefficient and Fermi's Golden rule	32
2.3.2	Relationship between optical absorption, refractive index, and dielectric constant	34
2.4	Electron-phonon interaction	36
2.5	Raman spectroscopy	38
2.5.1	Classical description of Raman scattering and Raman tensor	38
2.5.2	Quantum mechanical description of Raman scattering	43
3	Valley polarization in transition metal dichalcogenides	45
3.1	Dipole vector of hexagonal lattice	45
3.2	Laser energy dependence of valley polarization in TMDs	54
3.2.1	Electronic structure of TMDs	54
3.2.2	Absorption spectra of TMDs	55

3.2.3	Degree of valley polarization	57
4	Optical anisotropy of Gallium telluride and Black phosphorus	61
4.1	Gallium telluride	61
4.1.1	Crystal, electronic and phonon structure of bulk GaTe	62
4.1.2	Optical absorption	63
4.1.3	Raman spectra	67
4.2	Black phosphorus	73
4.2.1	Crystal structure of black phosphorus	73
4.2.2	Optical absorption of black phosphorus	74
4.2.3	Raman spectra of black phosphorus	77
5	Helicity exchange in the first-order Raman scattering for graphene and TMDs	81
5.1	Helicity-resolved Raman spectra	81
5.1.1	Electronic and phonon structure of graphene and TMDs	81
5.1.2	Helicity-resolved Raman spectra of graphene and MoS ₂	84
5.2	Raman matrix element	86
5.3	Discussion by group theory	88
5.4	Raman spectra in strain-induced graphene	90
6	Conclusions	93
A	Selection rule for optical dipole transition	95
A.1	Transition Dipole moment	95
A.2	Dipole selection rule under the rotational symmetry	101
B	Interference effect of optical absorption and Raman scattering	103
B.1	Interference effect of optical measurements	103
B.1.1	Interference effect for optical absorption	103
B.1.2	Interference effect of Raman scattering	106
C	Character table	109
D	Details of numerical calculations	113
D.1	Optical absorption in TMDs (Chap. 3)	113
D.2	Helicity-resolved Raman spectra (Chap. 5)	114
E	Program	117
E.1	Electron-photon matrix element and optical absorption	117
E.2	Phonon	122
E.3	Electron-phonon matrix element	123

E.4	First-order resonant Raman spectra	124
-----	--	-----

Chapter 1

Introduction

1.1 Purposes of the study

After the successful mechanical exfoliation of graphene in 2004,¹⁾ atomic layer materials have attracted a lot of interests for their unique properties. One of the promising applications for these two dimensional (2D) materials is in optoelectronics such as for photodetectors,²⁻⁴⁾ photodiodes,⁵⁾ phototransistors,^{6,7)} and light emitting diodes⁸⁾. In particular, for the monolayer transition metal dichalcogenides (TMDs) which have two independent valleys (K and K') in the electronic energy band structure, it is known that right- (or left-) handed circular polarized light can excite the electrons only at the K (or K') valley.^{9,10)} Such a valley-selective optical transition allows us to utilize the degree of freedom of the valley for the applications of optical and electronic devices, the so-called *valleytronics*. Optical valley polarizations of TMDs have been observed in photoluminescence spectroscopy,¹¹⁻²³⁾ optical Stark effect,²⁴⁾ and electroluminescence.²⁵⁾ However, we can not get 100 % valley polarization even when we use 100% polarized circular polarized light because the valley polarization depends on the electronic structure and incident laser energy. Therefore, we need to investigate the optimum condition for high valley polarization for the application of valleytronics, which becomes one of the subjects of this thesis.

Another subject of this thesis is Raman scattering of atomic layer materials. Raman spectroscopy is a conventional technique to characterize materials that are frequently measured for 2D materials. Recent studies report that Raman spectra of atomic layer materials also strongly depend on the circular or linear polarization of light. Atomic layer materials with low symmetry such as black phosphorus (BP) and gallium telluride (GaTe) have anisotropy of Raman intensity as a function of polarization direction of linear polarized light. As for the high symmetric materials which do not show any anisotropy for linear polarized light such like TMDs, it is reported that circular polarized light can observe the so-called helicity-resolved Raman peak by selecting the polarization for incident and scattered light.²⁶⁾ In order to understand those phenomena

(anisotropy and helicity-resolved Raman spectroscopy), the theoretical investigation is necessary to understand the electronic and geometrical structure of the material.

The purposes of this study are: (1) to investigate valley polarization in atomic layer materials for future application, and (2) to explain the observed Raman spectra for atomic layer materials by changing the polarization of light. We perform first-principles calculations based on the density functional theory (DFT) to calculate the optical absorption and Raman spectra. We also use group theory, tight-binding analytical calculation, and transfer matrix method to interpret the results of first-principles calculation.

1.2 Organization of thesis

This thesis is organized as follows. In the remaining part of Chapter 1, we introduce the atomic layer materials that are studied in this thesis. We also present the background of this study, including experimental results of valley polarization in TMDs, polarized Raman spectroscopy for BP and GaTe, and helicity-resolved Raman spectroscopy for TMDs. In Chapter 2, we explain the method to calculate optical absorption and Raman spectra. In Chapter 3, we present the calculated results and give discussion on the optical valley polarization for TMDs. In Chapter 4, we present the calculation and group theory analysis for the polarized Raman spectroscopy for BP and GaTe. In Chapter 5, we present the calculated results of helicity-resolved Raman spectra for circular polarized light in graphene and TMDs. In Chapter 6, we summarize the main results of the present thesis and give the conclusion.

1.3 Background

In this section, we introduce the background of the research in this thesis.

1.3.1 Rise of atomic layer materials

Recently, many researchers are interested in atomic layer material families which consist of graphene, transition metal dichalcogenides (TMDs), hexagonal boron nitride (hBN), black phosphorus (BP), gallium telluride (GaTe), etc. In Fig. 1-1, we show the crystal structures of the atomic layer materials which we discuss in this thesis.

Graphene, as shown in Fig. 1-1(a), is the most studied atomic layer material constituted by carbon atoms in the hexagonal lattice. Many researchers are interested in graphene because of its large electrical mobility and high mechanical strength. In

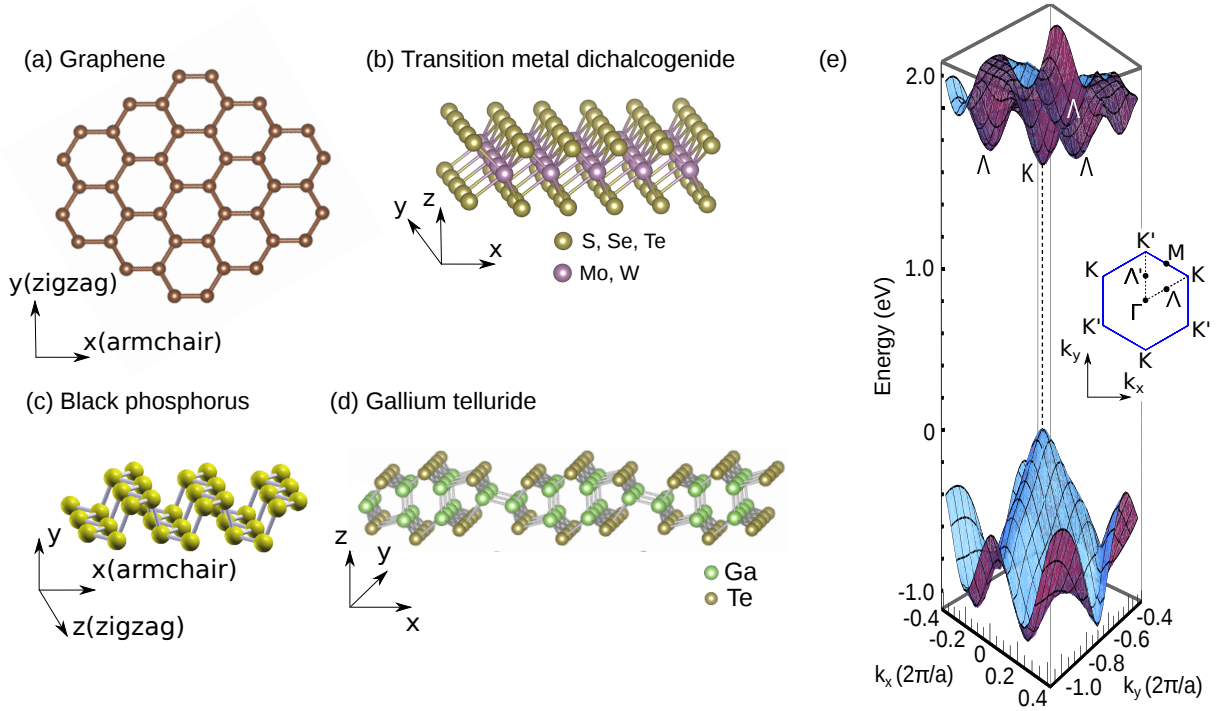


Figure 1-1: Crystal structures of some atomic layer materials: (a) graphene, (b) TMDs, (c) black phosphorus, and (d) gallium telluride. (e) The three dimensional plot of the electronic energy bands near the K and Λ points. The Brillouin zone and the typical high-symmetry points are shown in the inset of (e).

2004, Geim and Novoselov found a method to exfoliate graphene from graphite to one atomic layer of graphene using a Scotch tape.¹⁾ Since then, graphene sparked active researches of atomic layer materials. Due to the linear electronic energy dispersion near the Fermi energy, electrons in graphene behave as massless Dirac fermions. The absolute value of group velocity $v_g = \frac{1}{\hbar} \frac{\partial E}{\partial k}$ of the electron in the electronic energy dispersion does not change despite of the existence of the defects in the crystal. Graphene has a high electrical mobility because the v_g at the Fermi energy (Fermi velocity) v_F is large ($v_F \sim c/300$, c is the velocity of light).

There is one fundamental problem for the application of graphene to electronic devices; that is, graphene is a semimetal without an energy gap. Many studies have tried to open the energy gap for graphene, but it is still difficult for the industrial application to adopt graphene. Six transition metal dichalcogenides [TMDs, MX_2 ($\text{M} = \text{Mo}, \text{W}$, and $\text{X} = \text{S}, \text{Se}, \text{Te}$)], as shown in Fig. 1-1(b), are also recently studied for avoiding the problem of graphene since TMDs are semiconductors with hexagonal lattice structures like graphene. The reason why TMDs are semiconductors is that the three atoms in the unit cells are different from one another (transition metal and

Table 1.1: Optical energy band gap, mobility, photo-responsivity, and response time of graphene, TMDs, BP, and GaTe.

		Energy gap (eV)	mobility ($\text{cm}^2\text{V}^{-1}\text{s}^{-1}$)	responsivity (A/W)	response time (s)
graphene		semi-metal		0.01 ^{m)}	1.5×10^{-12} m)
MoS ₂	Monolayer	1.83 ^{a),1.90^{b)}}		880 ⁿ⁾	4 ⁿ⁾
	Bulk	1.23 ^{c), 1.29^{d)}}		0.1 ^{o)} (multilayer)	
MoSe ₂	Monolayer	1.58 ^{e)}			
	Bulk	1.09 ^{e), 1.1^{d)}}			
MoTe ₂	Monolayer	1.10 ^{f)}			
	Bulk	1.0 ^{d)}			
WS ₂	Monolayer	1.96 ^{e)}			
	Bulk	1.35 ^{c)}		9.2×10^{-5} p) (multilayer)	5×10^{-3} p)
WSe ₂	Monolayer	1.65 ^{g)}			
	Bulk	1.20 ^{c)}			
BP	Bilayer	1.60 ^{h)}			
	Bulk	0.33 ^{i,j)}	45000 ^{l)} (few layer)		
GaTe	Bulk	1.796 ^{k)}		274.3 ^{q), 10⁴ r)} (multilayer)	6×10^{-3} r)

a) Ref. 27, b) Ref. 28, c) Ref. 29, d) Ref. 30, e) Ref. 31 f) Ref. 32, g) Ref. 33, h) Ref. 34, i) Ref. 35, j) Ref. 36, k) Ref. 37, l) Ref. 38, m) Ref. 39, n) Ref. 3, o) Ref. 40, p) Ref. 41, q) Ref. 42, r) Ref. 43,

chalcogens). MoS₂, abundantly existing TMD in nature, is commercially available as a lubricant. As shown in Table 1.1, monolayer TMDs have various values (1-2 eV) of the energy gaps depending on the combination of the constituent atoms. It is known that the monolayer TMDs have a direct energy gap while the bulk TMDs have an indirect energy gap because the bottom of the conduction band shifts from the top of the valence band in bulk TMDs by the interlayer interaction. Interlayer interaction strongly affects the conduction band since the conduction bands of TMDs consist of the d_{z^2} orbital, which are delocalized in the z direction (see Fig. 1-2).

In Figs. 1-1(c) and (d), we show the structure of BP and GaTe, respectively. These two materials are also more recent and attracting atomic layer materials. BP belongs to D_{2h}^7 (D_{2h}^{11}) space group for odd (even) number of layers with AB stacking⁴⁴⁾ (AB stacking is one of stacking atomic layers in which a center of a hexagon of one layer is put above an atom of the nearest neighbor layer).

The most interesting point of BP is in-plane anisotropic property of its electronic

structure. Due to the anisotropic structure in the directions of x (zigzag) and y (arm-chair) as shown in Fig. 1-1(c), BP shows an anisotropic properties such as in its electrical conductivity⁴⁵⁾ as a tensor form, thermal transport,⁴⁶⁾ photo-current,⁴⁷⁾ optical absorption,^{45,48-50)} and polarized Raman intensity,^{45,51-53)} which can be observed by changing the direction of the polarization of light. The energy gap of BP monotonically decreases from 1.5 to 0.3 eV with increasing the number of layers. Thus, BP covers a smaller energy gap region than TMDs which is suitable for IR-THz optics. In fact, BP has a high mobility ($45000 \text{ cm}^2\text{V}^{-1}\text{s}^{-1}$)³⁸⁾ compared with TMDs. However, BP is chemically reactive and easily oxidized in the atmosphere, which makes device application difficult.

On the other hand, GaTe, which is a monoclinic structure with C_{2h}^3 symmetry shown in Fig. 1-1(d), is less-reactive and can exist relatively stably in the atmosphere. The advantage of GaTe is its high photo-responsivity⁴³⁾ (see Table 1.1), which can be a candidate of optoelectronic and photosensitive device applications. There are not so many works for the anisotropic properties of GaTe.⁵⁴⁾ However, a low symmetry structure of GaTe compared with other atomic layer materials has a potential to show the interesting anisotropic properties, for example, electrical conductivity and Raman intensity like BP.

1.3.2 Optical valley polarization of TMDs

The hexagonal lattice structure such as graphene and TMDs has two independent valleys (K and K') at the corner of the hexagonal Brillouin zone as shown in the inset of Fig. 1-1 (e). There is time reversal symmetry between the K and K' points. Valleytronics is an attempt to control the degree of freedom of the valleys. One possible way to select an independent valley (or valley polarization) is optical valley polarization by using left- and right-handed circular polarized light as is denoted by (σ_+ and σ_- respectively, which is reported by Yao *et al.* in 2008.⁵⁵⁾ The right- (left-) handed circular polarized light which has mirror symmetry on a mirror parallel to the propagation direction of light, can excite only the electron at the K (K') point⁵⁵⁾ (see Chapter 3-1). Such a valley-selective optical transition occurs in the hexagonal structures that does not have inversion symmetry since the inversion symmetry would request that a Bloch state at \mathbf{k} has a counterpart at $-\mathbf{k}$ in which same optical transition occurs for \mathbf{k} and $-\mathbf{k}$ states. For example, graphene does not show valley polarization.

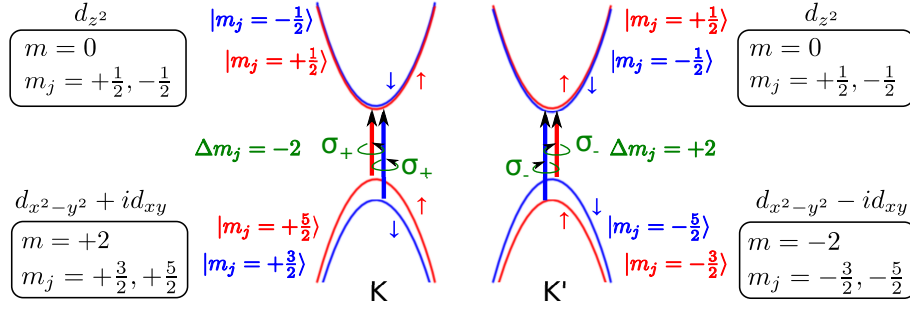


Figure 1-2: Schematic figure of valley polarization in TMDs. The m_j is the z -component of total angular momentum for spin-split valence and conduction bands, contributed by d orbital of transition metal (Mo or W). Right- (Left-) handed circular polarized light σ_+ (σ_-) excites the electron at the K' (K) point by following the selection rule of circular polarized light under the three-fold rotation symmetry $\Delta m_j = -2$ ($+2$).

Selection rule of optical transition at K (K') valley

The optical selection rule for circular polarized light in TMDs can be understood by the conservation of total angular momentum in the electric dipole transition. The selection rule of the electric dipole transition is $\delta \ell = \pm 1$ and $\Delta m = 0, \pm 1$, where ℓ and m are, respectively, azimuthal and magnetic angular momenta. The valence bands of TMDs near the K (K') point consists of $d_{x^2-y^2} \pm id_{xy}$ orbital ($\ell = 2, m = \pm 2$) of transition metal atom and the small contribution of $p_x \pm ip_y$ orbital ($\ell = 1, m = \pm 1$) of chalcogen atoms, while the conduction bands consist of d_{z^2} orbital ($\ell = 2, m = 0$) of transition metal atom and the small contribution of $p_x \pm ip_y$ orbital ($\ell = 1, m = \pm 1$) of chalcogen atoms, where the plus (minus) sign is taken for the K (K') point. Due to the lack of inversion symmetry, the electronic energy bands of TMDs are splitted by the spin-orbit interaction.⁵⁶⁻⁶¹ Then, by considering the z -component of the total angular momentum $m_j = m + s_z$ is given as shown in Fig. 1-2, where s_z is z component of $1/2$ spin of an electron. Generally, the selection rule of optical transition for Δm_j by circular polarized light σ_+ (σ_-) is given by $\Delta m_j = +1$ (-1). However, in the case of TMDs, we have to consider the selection rule under the 3-fold rotational symmetry at the K and K' point around the z axis.⁵⁵ The Bloch states of TMDs at the K (K') point are invariant for the 3-fold rotation $R\left(\frac{2\pi}{3}\right)$, in which we can write for the wave function $|\psi_{c(v)}(\mathbf{k})\rangle$ as follows⁵⁵;

$$R\left(\frac{2\pi}{3}, \hat{z}\right) |\psi_{c(v)}(\mathbf{k})\rangle = e^{-i\frac{2\pi}{3}m_j^{c(v)}} |\psi_{j,c(v)}(\mathbf{k})\rangle. \quad (1.1)$$

Then, the selection rule of the optical transition for circular polarized light is given by⁵⁵⁾ (see Appendix A),

$$\Delta m_j = m_j^c - m_j^v = \pm 1 + 3N, \quad (1.2)$$

where $N = 0, \pm 1, \pm 2, \dots$ is the integer and the $+$ ($-$) sign in Eq. (1.2) indicates σ_+ (σ_-). Eventually, we can obtain the optical selection rule for σ_+ (σ_-) in TMDs: $\Delta m_j = -2$ ($+2$) at the K (K') point with $N = -1$ ($+1$). Note that the spin quantum number s_z is conserved for the electric dipole transition ($\Delta s_z = 0$).

k -dependence of valley polarization

The valley and spin are independent variables that both have two degrees of freedom (K and K', up and down), which can be coupled with each other in TMDs. Xiao *et al.* discuss the valley-spin coupling in TMDs and derive an analytical formula for the interband matrix element⁵⁷⁾. They consider the $\mathbf{k} \cdot \mathbf{p}$ Hamiltonian by taking spin-orbit coupling into account in the two bands model of TMDs, expressed as follows,

$$\hat{H} = at (\tau k_x \hat{\sigma}_x + k_y \hat{\sigma}_y) + \frac{\Delta}{2} \hat{\sigma}_z - \lambda \tau \frac{\hat{\sigma}_z - 1}{2} \hat{s}_z, \quad (1.3)$$

where a , t , Δ , and λ are the lattice constant, effective hopping integral, energy gap, and spin splitting, respectively. The $\hat{\sigma}$ and \hat{s}_z are the Pauli matrices for the two basis functions and spin, respectively. The variable τ is the so-called valley spin ($\tau = +1$ for K and $\tau = -1$ for K'). The wave numbers k_x and k_y are measured from the K or K' points. From Eq. (1.3), they derive the matrix element $M_{\pm}(\mathbf{k})$ of electric dipole transition for the σ_{\pm} light as a function of \mathbf{k} around the K (K') point as follows⁵⁷⁾;

$$|M_{\pm}(\mathbf{k})|^2 = \frac{m_0^2 a^2 t^2}{\hbar^2} \left(1 \mp \tau \frac{\Delta^2}{\sqrt{\Delta^2 + 4a^2 t^2 k^2}} \right)^2. \quad (1.4)$$

When we put $k = 0$ for the K (K') point, we obtain the selection rule for k at the K (K') that $|M_{\pm}(\mathbf{k})|^2 = 2 \frac{m_0^2 a^2 t^2}{\hbar^2}$ for σ_- (σ_+) light and $|M_{\pm}(\mathbf{k})|^2 = 0$ for σ_+ (σ_-) light which shows that optical transition is forbidden at one of the two points for given σ_{\pm} light. Then, the degree of valley polarization as a function of \mathbf{k} , $\eta(\mathbf{k})$ around the K (K') point is defined by

$$\eta(\mathbf{k}) = \frac{|M_+(\mathbf{k})|^2 - |M_-(\mathbf{k})|^2}{|M_+(\mathbf{k})|^2 + |M_-(\mathbf{k})|^2} = \frac{2\tau\Delta^2\sqrt{\Delta^2 + 4a^2t^2k^2}}{\Delta^4 + \Delta^2 + 4a^2t^2k^2}. \quad (1.5)$$

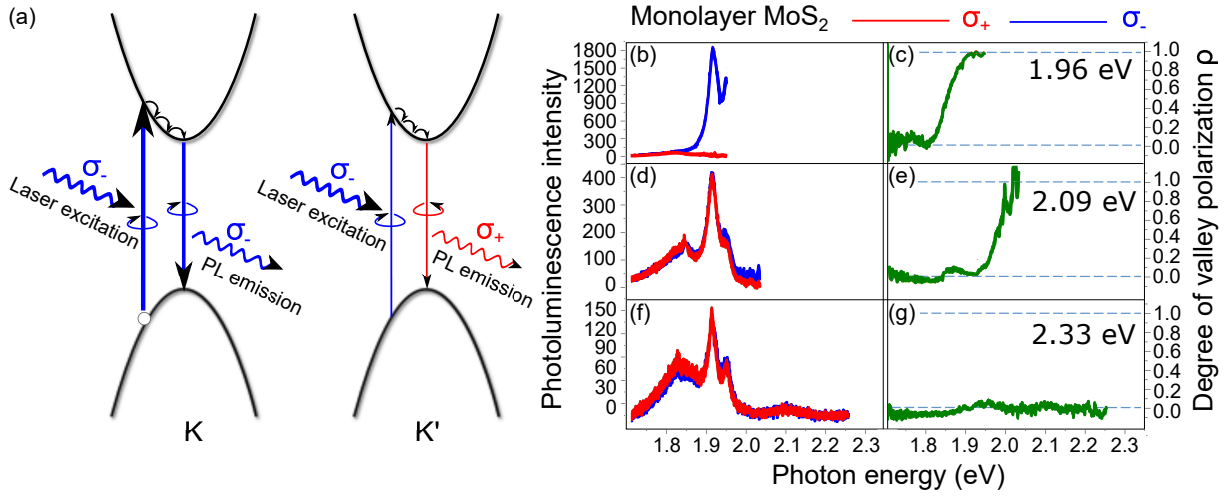


Figure 1-3: (a) Schematic picture of the experiment of the detection of valley polarization by Mak *et al.*¹¹⁾ (b)-(g) Photoluminescence intensity (left figure) and the valley polarization ρ (right figure) of monolayer MoS₂ with the excitation of left-handed circular polarized light (σ_-)¹¹⁾. Excitation laser energy is (b)-(c) 1.96 eV (633 nm), on resonance with the A exciton, (d)-(e) 2.09 eV (594 nm), on resonance with the B exciton, and (g)-(g) 2.33 eV (532 nm), off resonance with both the A and B exciton.

From Eqs. (1.4) and (1.5), the optical valley polarization monotonically decreases ($\eta(\mathbf{k}) \rightarrow 0$) with increasing \mathbf{k} , that is, the distance from the K or K' point.

Experimental observation of valley polarization in TMDs

An important question for the application of valleytronics is how to detect the valley polarization in the experiment. Mak *et al.* and many researchers observed the optical valley polarization by photoluminescence,¹¹⁻²³⁾ optical Stark effect,²⁴⁾ and electroluminescence.²⁵⁾ In Fig. 1-3(a), we show the schematic picture of photoluminescence (PL) considered in the experiment by Mak, *et al.* PL is the process that the photo-excited electron by the excitation laser is relaxed to the bottom of the conduction band and that the photo-excited electron finally recombines with a hole by emitting a photon. In the case of the TMDs, the excited electron by circular polarized light is relaxed to the one of the bottoms at the K or K' valley. Then the valley polarized circular polarized light is observed as the light emission at the K (K') point. In order to discuss the valley polarization by PL, the degree of the valley polarization ρ for PL intensity is defined by

$$\rho = \frac{I(\sigma_-) - I(\sigma_+)}{I(\sigma_-) + I(\sigma_+)}, \quad (1.6)$$

where $I(\sigma_+)$ [$I(\sigma_-)$] is the PL intensity for σ_+ (σ_-) light. $\rho = -1$ ($+1$) when the emitted light is completely polarized to σ_+ (σ_-).

In Figs. 1-3(b)-(g), we show the experimental PL intensity and the degree of the valley polarization ρ of monolayer MoS₂, one of TMDs, reported by Mak *et al.*¹¹⁾ In Figs. 1-3(b)-(g), all the excitation is given by σ_- light and they observe the emitted light by dividing σ_+ and σ_- . The PL intensity and the degree of the valley polarization ρ in Fig. 1-3 is observed for three laser excitation energies E_L : (b)-(c) $E_L = 1.96$ eV, (d)-(e) $E_L = 2.09$ eV, and (f)-(g) $E_L = 2.33$ eV. TMDs have large spin-splitting around the K (K') point (~ 0.15 eV for MoS₂) and two excitons (A and B exciton) are observed with different resonance energy.^{11,12)}

In 2D materials, since the exciton binding energy (~ 0.1 eV) is sufficiently large, the excitons can exist at the room temperature. The $E_L = 1.96$ (2.09) eV corresponds to the resonance energy of the A (B) exciton while the $E_L = 2.33$ eV is off-resonance excitation energy from the A and B excitons. The degree of valley polarization ρ for the resonance energy of the A or B excitons is almost 1.0 [Fig.1-3 (c) and (e)] while the ρ for the off-resonance energy is almost 0 [Fig.1-3 (g)]. This result indicates that the electron at the K valley is excited by σ_- light and the excited electrons are mainly relaxed to the bottom of conduction band of the K valley, and then the electron is combined with a hole by emitting the σ_- light in the case of the resonance excitation energy for the A and B excitons. However, when the excitation energy is off-resonance, the excitation of electron is far from the K point and $\eta(\mathbf{k})$ in Eq. (1.5) approaches zero. In this case, the excited electrons far from the K point are also scattered or relaxed to K' point and we can not observe the valley polarization as shown in Fig. 1-3 (f) and (g).

Another way to detect directly the valley polarization is achieved by breaking the valley degeneracy by applying magnetic field, which is reported by Aivazian *et al.*²⁰⁾ In Fig. 1-4(a), we show the energy states of TMDs at the K and K' point in the magnetic field.²⁰⁾ When we apply the magnetic field, not only the Zeeman shift due to the spin magnetic moment ($\Delta_s = 2s_z\mu_B B$, black arrows), but also the Zeeman shift due to the valley magnetic moment ($\Delta_v = \alpha\tau\mu_B B$, green arrows), and further the energy shift by orbital magnetic moment ($\Delta_\alpha = m\mu_B B$, purple arrows) affect to the energy levels where $\tau = -1(+1)$, μ_B , and α are, respectively, the valley index at K (K') valley, Bohr magneton, and the valley g-factor. We note that Δ_α does not affect in conduction bands since the conduction bands of TMDs at the K valley is by d_{z^2} ($m = 0$) orbital of transition metal. Then the valley degeneracy at the K and K' points are lifted by Δ_s , Δ_v , and Δ_α in the magnetic field. In Fig. 1-4(b), we show the polarization-resolved PL intensity excited by σ_+ and σ_- light under the magnetic field.²⁰⁾ The peak positions of

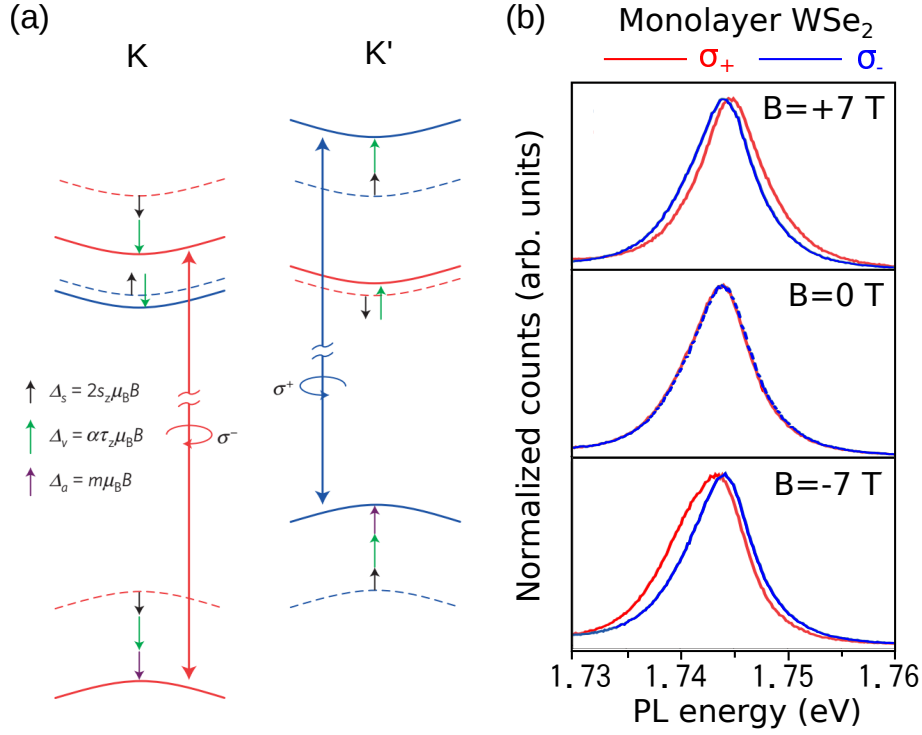


Figure 1-4: The detection of valley polarization for WSe₂ under the magnetic field.²⁰⁾ (a) Energy states of TMDs at the K and K' valley under the magnetic field. Solid (Dashed) lines are the energy states with (without) magnetic field. Black, green, and purple arrows are, respectively, the Zeeman shift due to the spin magnetic moment, the atomic orbital contribution, and the valley magnetic moment. (b) Polarization-resolved PL intensity for the excitation by σ_+ and σ_- under the magnetic field of -7 T (top), 0 T (middle), and +7 T (bottom). Laser excitation energy is 1.88 eV.

PL for σ_+ and σ_- excitation are shifted under the magnetic field due to the lifting of valley degeneracy.

“ Λ valley”: another valley in the Brillouin zone

Finally, let us discuss the valley in the other k point in the Brillouin zone. As discussed above, the optical valley polarization at the K (K') valleys is well investigated up to now. However, the electronic structures of TMDs are not so simple. It is known that there is another so-called Λ valley between the Γ and the K points at slightly higher energy compared that of the K valley in TMDs.⁶²⁾ [see Fig. 1-1 (e)] The optical absorption for the gap energy at the Λ point is strong because of large joint density of states due to the nesting of energy bands.^{62,63)} Selig *et al.* reported the existence of an intervalley exciton where an electron is located at the Λ point and a hole is at

the K point.⁶⁴⁾ The valley polarization of higher energy region including Λ valley is not yet discussed until now. We might find the new possibility of valleytronics by using the Λ valley. In order to study the optical valley polarization at large E_L , we perform the first-principles calculation to obtain the laser energy dependence of the valley polarization with the consideration of all energy bands near the Fermi energy, discussed in Chapter 3.

1.3.3 Polarized and helicity-resolved Raman spectroscopy in atomic layer materials

In this subsection, we introduce Raman spectroscopy with the polarization of light, which is another topic of this thesis.

Basic concept of Raman spectroscopy

Raman spectroscopy is the conventional technique to know the crystal and electronic structures of materials. Raman scattering is inelastic scattering of light in which the difference of the energy between the incident and scattered light is used for the absorption or emission of a phonon. In Fig. 1-5, we show the schematic picture of the process of Raman scattering. The incident photon interacts with the electron (electron-photon interaction M_{opt}^{mi}) in the valence band and excites the electron to the conduction band. Then, the photo-excited electron emits (or absorbs) a phonon by electron-phonon interaction $M_{\text{ep}}^{m'm}$ and returns to the valence band by emitting a photon by electron-photon interaction $M_{\text{opt}}^{im'}$. The scattering process of light with emitting (or absorbing) the phonon is called as Stokes (or Anti-Stokes) Raman scattering.

The signal of the inelastic scattered light is usually very weak compared with elastic scattering. However, the Raman intensity is enhanced when the energy of either the incident or scattered light matches with the energy separation between the initial and final electronic states which corresponds to the situation that m (or m') is a real electronic state (resonant Raman spectroscopy). We show the schematic picture of the resonant Raman scattering for not only the first-order (one phonon) but also second-order (two phonons) processes in Fig. 1-6. As shown in Fig. 1-6(a), resonance condition is satisfied when the incident (scattered) laser energy matches the energy difference between i and m (m') states, which is called incident (scattered) resonance. One of the two intermediate states (m and m') is not necessary to be the real (eigen) state, which is called “virtual state” described by dashed open circle in Fig. 1-6. Assuming that the initial and final states of electron in Raman scattering is the same, only the $\mathbf{q} = 0$ (Γ point) phonon is emitted or absorbed in the incident and scattered resonance

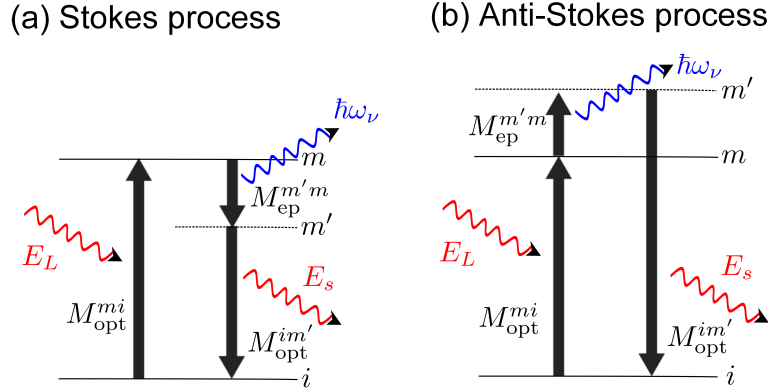


Figure 1-5: Schematic picture of Raman scattering process for (a) Stokes and (b) Anti-Stokes Raman scattering. E_L , E_s , and $\hbar\omega_\nu$ are the energy of the incident laser, scattered light, emitted (absorbed) phonon, respectively. The M_{opt}^{fi} (M_{ep}^{fi}) indicates the electron-photon (electron-phonon) matrix element from the i to f state.

of first-order Raman scattering [see Fig. 1-6(a)].

The Raman intensity of second-order Raman scattering process which emits or absorbs two phonons is comparable with the first-order process when two resonant conditions are satisfied simultaneously (two states in the three intermediate m , m' , and m'' states are eigen states). As shown in Fig. 1-6(b), m and m' (m' and m'') states of incident (scattered) resonance are real states. In the case of second-order Raman scattering, $\mathbf{q} \neq 0$ phonon can be emitted or absorbed to satisfy the momentum conservation and the intermediate states are possible not only in the same valley [intravalley scattering with small \mathbf{q} , Fig. 1-6(b1)], but also in the different valley [intervalley scattering with large \mathbf{q} , Fig. 1-6(b2)].

The difference of the energy between the incident and scattered light which we call Raman shift corresponds to the energy of the emitted (absorbed) phonon and we usually plot the Raman spectra as a function of Raman shift defined by a energy difference in units of cm^{-1} . between incident and scattered light. In Fig. 1-7, we show (a) the Raman spectra⁶⁵⁾ and (b) the phonon dispersion of graphene.⁶⁶⁾ It is known that graphene has strong Raman peak called the G band around the 1600 cm^{-1} . This peak corresponds to the emission of phonons in the doubly-degenerate in-plane phonon modes which is called LO and iTO mode. The LO and iTO modes have the wave number of 1600 cm^{-1} at the Γ point [see the phonon dispersion of graphene in Fig. 1-7(b)]. The oTO phonon mode as another optical phonon mode with the frequency of 840 cm^{-1} at the Γ point which vibrates out-of-plane direction in Fig. 1-7(b), is not a Raman active mode, but an infrared active mode and thus does not appear in the Raman spectra. The D

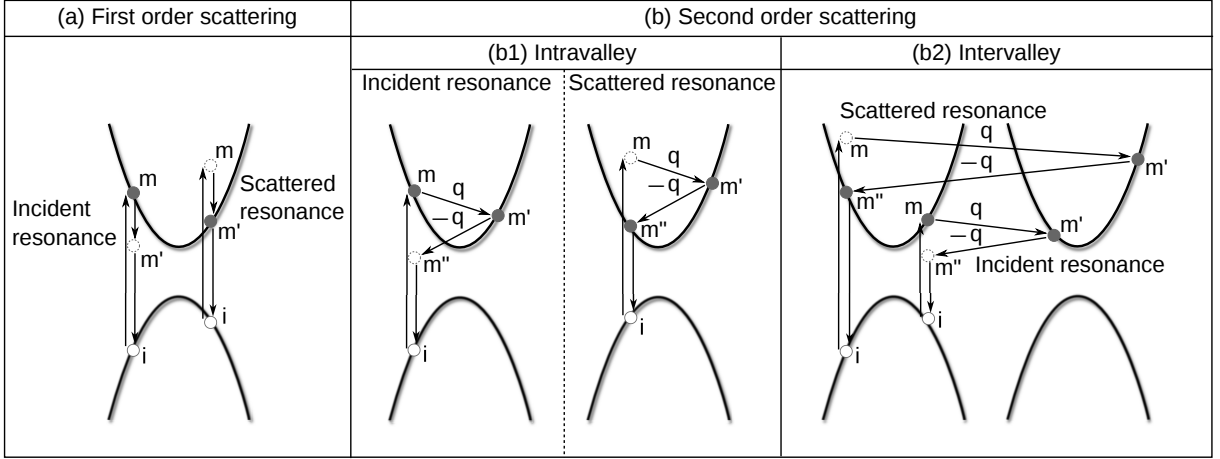


Figure 1-6: The illustration of resonant Raman scattering process for (a) first-order (one phonon) and (b) second-order (two phonon) scattering.⁶⁷⁾ In the second-order scattering, we show the (b1) intravalley and (b2) intervalley scattering. The label i (initial and final states, open circle) m , m' , and m'' (intermediate states) are either real or virtual electronic states. q and $-q$ are the wave number of phonon. We show the initial and final states as white solid circle, and intermediate real (virtual) state as black solid (white dashed) circle.

and D' bands which appear around 1350 and 1650 cm^{-1} , respectively, arise from the scattering by the point defect or edge of the sample and we can evaluate the quality of the sample. the D and D' bands vanish in the single crystal graphene which does not have defects. the G' band at around 2700 cm^{-1} is originated from the second-order Raman process which emits two phonons with $q \neq 0$ at around the K (K') point. We can obtain rich information of the sample from Raman spectroscopy.

Polarized Raman spectroscopy

The Raman intensity can depend on the polarization of light. For example, materials with low symmetrical structures show the anisotropic Raman intensity by changing the direction of polarization of the incident and scattered light, which is called polarized Raman spectroscopy. In Fig. 1-8, we show the geometry of the experimental set up for polarized Raman spectroscopy.⁷⁰⁾ In polarized Raman spectroscopy, we measure the intensity of the scattered light by changing the polarization of the direction for the incident and scattered light. There are two typical geometries of the polarization, that is, parallel (HH) and perpendicular (HV) configurations. The parallel configuration is the geometry which the polarization direction of the incident and scattered light are parallel each other while the polarization direction of incident and scattered light in

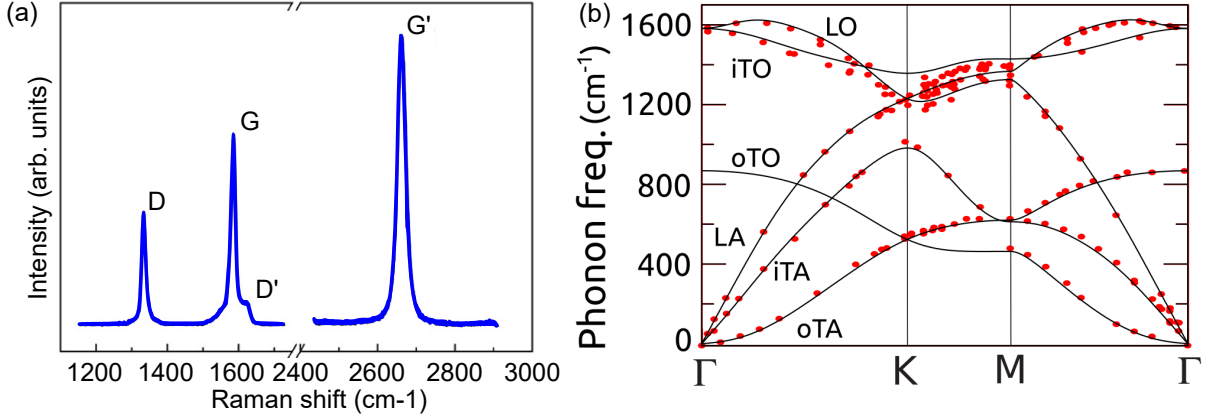


Figure 1-7: (a) Raman spectra of graphene edge.⁶⁵⁾ (b) Phonon dispersion of graphene calculated by Hasdeo, *et al.*,⁶⁶⁾ (solid line) and the experimental data, reported by Maultzsch *et al.*⁶⁸⁾ and Mohr *et al.*⁶⁹⁾ (dots).

perpendicular configuration is perpendicular to each other. By rotating θ of polarizers with fixing θ_1 and θ_2 as parallel configuration ($\theta = \theta_1 = \theta_2$), we can obtain the HH-polarized Raman spectra as a function of ψ , as is shown in Fig. 1-8.

In Fig. 1-9, we show the angle-resolved Raman spectra of BP⁷¹⁾ and GaTe.⁵⁴⁾ In BP, we observe three typical Raman peaks, A_{1g} , B_{2g} , and A_{2g} modes at around 361, 438, and 466 cm⁻¹, respectively. As shown in Fig. 1-9(b), Raman intensity of A_{1g} and A_{2g} (B_{2g}) modes are enhanced when $\theta = 0$ or 90 (45) degree. In the case of GaTe, A_g (B_g) Raman intensity for the peak at around 115 (161) cm⁻¹ is enhanced when $\theta = 0$ (45) degree [Fig. 1-9 (d)]. The Raman peak at 126 cm⁻¹ corresponding to double resonant scattering does not have any polarization direction for the polarized Raman intensity.⁵⁴⁾ The simple explanation of the polarized Raman intensity is given by the Raman tensor⁷²⁾ which is the classical theory with considering only the symmetry of phonon vibration (the details of Raman tensor is given in Sec. 2-3). According to the discussion of the Raman tensor, the Raman intensity for ν phonon mode $I_{\text{Raman}}(\nu)$ is given by

$$I_{\text{Raman}}(\nu) = \left| \mathbf{P}_s^* \overleftrightarrow{\mathbf{R}}(\nu) \mathbf{p}_i \right|^2, \quad (1.7)$$

where \mathbf{P}_i (\mathbf{P}_s) and $\overleftrightarrow{\mathbf{R}}(\nu)$ are the polarization vector of incident (scattered) light and the Raman tensor for the ν phonon mode. Raman tensor gives the Raman intensity as a function of polarization angles $\theta_1 = \theta_2$ of incident and scattered light, respectively. Raman tensors for A_g and B_g phonon modes which are observed in GaTe and BP are,

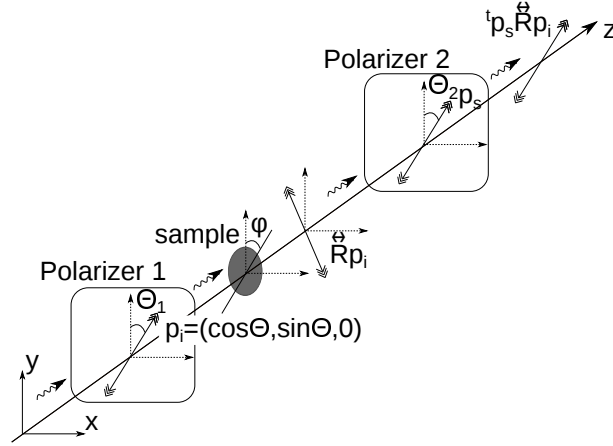


Figure 1-8: Geometry of the polarized Raman spectroscopy.⁷⁰⁾ The \mathbf{P}_i (\mathbf{P}_s) is the polarization vector of incident (scattered) light which indicates the direction of the polarization of light divided by the polarizer. The θ_1 and θ_2 are the polarization angles.

respectively, written as (see Table 2.1)

$$\overleftrightarrow{R}(A_g) = \begin{pmatrix} a & 0 & 0 \\ 0 & b & 0 \\ 0 & 0 & c \end{pmatrix}, \quad (1.8)$$

$$\overleftrightarrow{R}(B_g) = \begin{pmatrix} 0 & d & 0 \\ d & 0 & 0 \\ 0 & 0 & 0 \end{pmatrix}. \quad (1.9)$$

Here we consider the case that the linear polarized light propagates in the direction of z (perpendicular to atomic layer plane) direction and that the polarization vectors for incident and scattered light are parallel to each other (parallel configuration). Then, the polarization vectors for the parallel configuration are written as,

$$\mathbf{P}_i = \mathbf{P}_s = \begin{pmatrix} \cos \theta \\ \sin \theta \\ 0 \end{pmatrix}, \quad (1.10)$$

where θ is the HH polarization angle of the light in xy plane which we set $\theta = 0$ for the x axis. By using Eqs. (1.7)-(1.10), the Raman intensities for A_g and B_g modes under the parallel configuration are given by,

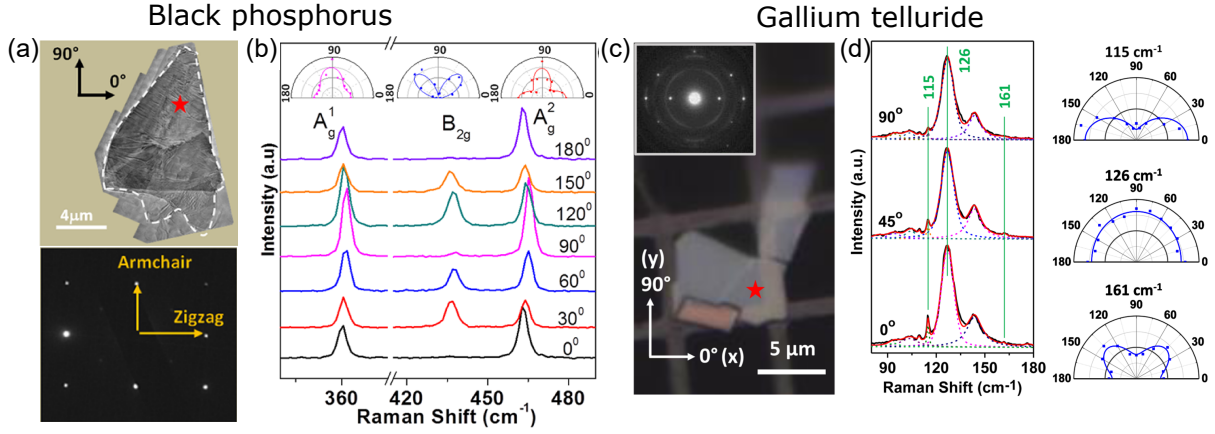


Figure 1-9: (a) Sample configuration of black phosphorus for angle-resolved Raman spectroscopy.⁷¹⁾ (b) Polarized Raman spectra of black phosphorus for the A_{1g} , B_{2g} , and A_{2g} peaks.⁷¹⁾ (c) Sample configuration of GaTe for angle-resolved Raman spectroscopy.⁵⁴⁾ (d) Angle-resolved Raman spectra of GaTe for the peak at 115 (A_g), 126 (double resonant mode), and 161 (B_g) cm^{-1} .⁵⁴⁾

$$\begin{aligned}
 I_{\text{Raman}}(A_g) &= \left| \begin{pmatrix} \cos \theta & \sin \theta & 0 \\ a & 0 & 0 \\ 0 & b & 0 \\ 0 & 0 & c \end{pmatrix} \begin{pmatrix} \cos \theta \\ \sin \theta \\ 0 \end{pmatrix} \right|^2 \\
 &= |a \cos^2 \theta + b \sin^2 \theta|^2, \tag{1.11}
 \end{aligned}$$

$$\begin{aligned}
 I_{\text{Raman}}(B_g) &= \left| \begin{pmatrix} \cos \theta & \sin \theta & 0 \\ 0 & d & 0 \\ d & 0 & 0 \\ 0 & 0 & 0 \end{pmatrix} \begin{pmatrix} \cos \theta \\ \sin \theta \\ 0 \end{pmatrix} \right|^2 \\
 &= |2d \sin \theta \cos \theta|^2. \tag{1.12}
 \end{aligned}$$

In Fig. 1-10, we plot the Raman intensity for A_g and B_g Raman mode as a function of polarization angle θ calculated by Eqs. (1.11) and (1.12). The Raman intensity for A_g (B_g) mode has maximum intensity for $\theta = 90^\circ$ and 270° ($\theta = 45^\circ, 135^\circ, 225^\circ,$ and 315°). The main axis of polar plot for Raman intensity in Fig. 1-10 is x - (90° and 270°) direction for the case of $a > b$ while the main axis is flipped to y - (0° and 180°) direction in the case of $b > a$. In such a way, Raman tensor tells us the general shape of polar plot of Raman intensity. However, the parameter a , b , c , and d of Raman tensors in Eq. (5.2) and (5.3) depend on the excitation laser energy on the electronic wave function and the thickness (see Fig.4-6 in chapter 4). In order to understand the

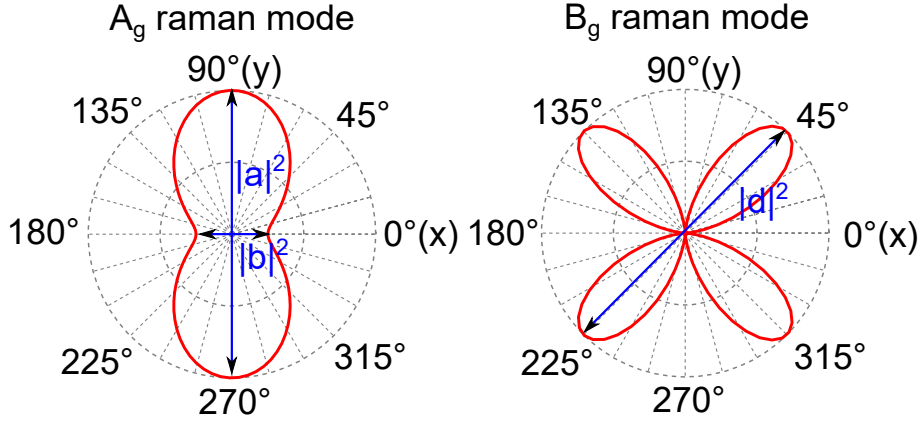


Figure 1-10: Plot of Raman intensity for (a) A_g and (b) B_g modes calculated by Raman tensor in Eqs. (1.11) and (1.12). We use $a = 1, b = 0.5, d = 1$ in the plot.

laser energy and thickness dependence of the polar plot of Raman intensity, we need to consider the theoretical treatment of quantum mechanics. We clarify the detail of polarized Raman spectra in BP and GaTe by considering the symmetry of the wave function and the interference effect in Chapter 4.

Helicity-resolved Raman spectroscopy

Finally, we introduce the helicity-resolved Raman spectroscopy which is somewhat new in the Raman spectroscopy. Chen *et al.* reported that IMC phonon mode in the Raman spectra of MoS_2 change the helicity of light^{73,74} (σ_+ or σ_-) after Raman scattering.²⁶⁾ There are two typical Raman peaks called IMC and OC modes at around 390 and 410 cm^{-1} in MoS_2 . IMC (OC) mode is the phonon mode in which the transition metal and chalcogen (only the chalcogen) atoms vibrate to in-plane (out-of-plane) direction as shown in Fig. 1-11(a) top. As shown in Figs. 1-11(b) and (c), the IMC peak appears only when the helicity of the incident and scattered light is different [$\bar{z}(\sigma_+ \sigma_-)z$, blue line] while the OC peak appears when the helicity of light is same [$\bar{z}(\sigma_+ \sigma_+)z$, orange line]. The symbol of $\bar{z}(\sigma_s \sigma_i)z$ denotes the σ_i circular polarized light propagates in the direction of z and scattered backwards (\bar{z}) with σ_s circular polarized light. The helicity exchange in IMC Raman mode is observed also in the multilayer TMDs even for the bilayer TMDs which does not have the inversion symmetry [see Fig. 1-11(b)]. In the multilayer TMDs, There are also Raman active inter-layer vibrating modes which is called shear and breathing modes [Fig. 1-11(a) bottom]. As shown in Fig. 1-11(d), Chen *et al.* also reported that such a helicity exchange of photon is observed in interlayer phonon mode in multilayer MoS_2 , too.⁷⁵⁾ As shown in Fig. 1-11 (d), The shearing

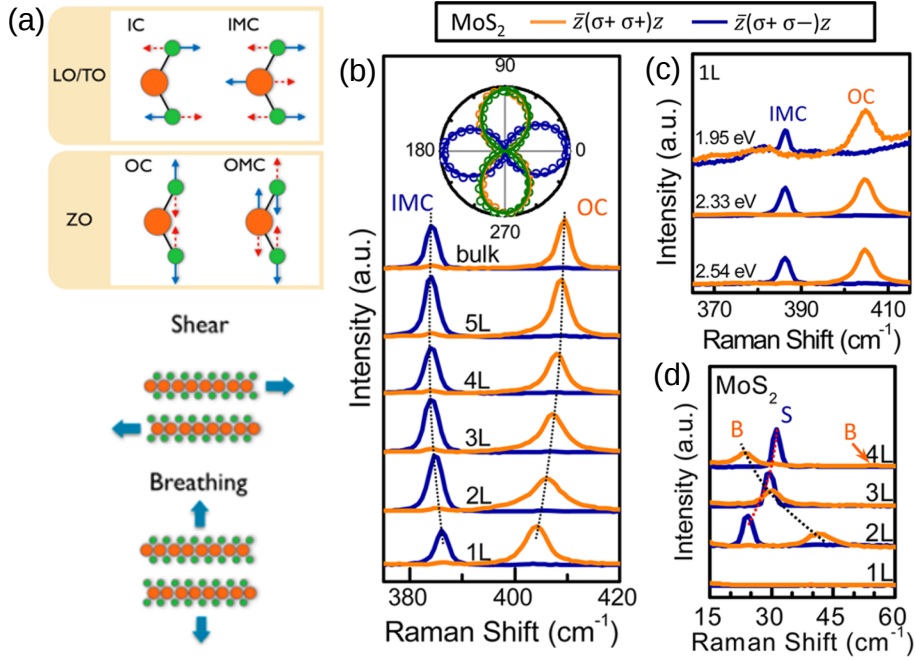


Figure 1-11: (a) Vibration modes of TMDs. The orange (green) color indicates transition metal (chalcogen). We show the in-plane (IC and IMC), out-of-plane (OC and OMC), shearing, and vibrating modes. (b)-(d) Helicity-resolved Raman spectra of MoS₂] (b) layer number dependence, (c) laser energy dependence of monolayer MoS₂, and (d) Shear and breathing mode. Orange (blue) line is the Raman spectra that optical helicity do not change (change). Helicity-resolved Raman spectra.

(breathing) mode which vibrates in-plane (out-of-plane) direction changes (does not change) the helicity in Raman scattering process.

The selection rule of circular polarized light for IMC and OC modes can be discussed, too, by Raman tensor in Eq. (1.7). The polarization vector for σ_+ (σ_-) light is written by $\mathbf{P}_{\sigma_+} = \frac{1}{\sqrt{2}}(1, i, 0)$ ($\mathbf{P}_{\sigma_-} = \frac{1}{\sqrt{2}}(1, -i, 0)$). The Raman tensor for OC (A_g) and doubly-degenerate IMC (E') mode in D_{3h} symmetry is written by (see Table 2.1)

$$\overleftrightarrow{R}(\text{IMC}) = \begin{pmatrix} 0 & d & 0 \\ d & 0 & 0 \\ 0 & 0 & 0 \end{pmatrix}, \begin{pmatrix} d & 0 & 0 \\ 0 & -d & 0 \\ 0 & 0 & 0 \end{pmatrix}. \quad (1.13)$$

$$\overleftrightarrow{R}(\text{OC}) = \begin{pmatrix} a & 0 & 0 \\ 0 & a & 0 \\ 0 & 0 & c \end{pmatrix}, \quad (1.14)$$

Then the Raman intensity is calculated by using Eqs. (2.82), (1.14), and (1.13) as,

$$\begin{aligned}
I_{\text{Raman}}(\text{IMC}) &= \left| \mathbf{P}_{\sigma-}^* \overleftrightarrow{R}(\text{IMC}) \mathbf{P}_{\sigma+} \right|^2 = |d|^2, \\
I_{\text{Raman}}(\text{IMC}) &= \left| \mathbf{P}_{\sigma+}^* \overleftrightarrow{R}(\text{IMC}) \mathbf{P}_{\sigma+} \right|^2 = 0, \\
I_{\text{Raman}}(\text{OC}) &= \left| \mathbf{P}_{\sigma-}^* \overleftrightarrow{R}(\text{OC}) \mathbf{P}_{\sigma+} \right|^2 = 0, \\
I_{\text{Raman}}(\text{OC}) &= \left| \mathbf{P}_{\sigma+}^* \overleftrightarrow{R}(\text{OC}) \mathbf{P}_{\sigma+} \right|^2 = |a|^2.
\end{aligned} \tag{1.15}$$

From Eq. (1.15), we can know that the Raman scattering for IMC (OC) mode changes (does not change) the helicity of light. The helicity exchange of IMC Raman mode implies that IMC phonon modes can change the helicity of light in the scattering process with exchanging the angular momentum from phonon to the photon.

The angular momentum of a photon is defined by^{73,74)}

$$\mathbf{S}_{\text{photon}} = \sigma \frac{\mathbf{k}_{\text{opt}}}{|\mathbf{k}_{\text{opt}}|}, \tag{1.16}$$

where \mathbf{k}_{opt} is the momentum vector whose direction is the propagation direction of light. The σ is called helicity and has the value of either +1 or -1 for left or right-handed circular polarized light, respectively. We can confirm the fact that the circular polarized light has the angular momentum as follows. The circular polarized electromagnetic plane wave propagating z direction is written by

$$\mathbf{E}(z, t) = \frac{1}{\sqrt{2}} e^{i(k_{\text{opt}}z + \omega t)} \begin{pmatrix} 1 \\ i\sigma \\ 0 \end{pmatrix}. \tag{1.17}$$

The electric field defined by Eq. (1.17) represents the eigen modes of z -component of the spin-1 matrix operator $\hat{\mathbf{S}}$ defined by⁷⁶⁾

$$\hat{\mathbf{S}} = -i \left\{ \begin{pmatrix} 0 & 0 & 0 \\ 0 & 0 & -1 \\ 0 & -1 & 0 \end{pmatrix}, \begin{pmatrix} 0 & 0 & -1 \\ 0 & 0 & 0 \\ 1 & 0 & 0 \end{pmatrix}, \begin{pmatrix} 0 & 1 & 0 \\ -1 & 0 & 0 \\ 0 & 0 & 0 \end{pmatrix} \right\}. \tag{1.18}$$

By Eqs. (1.17) and (1.18), we obtain

$$\hat{S}_z \mathbf{E}(z, t) = \sigma \mathbf{E}(z, t). \tag{1.19}$$

In 2D material, degenerate in-plane phonon modes can have angular momentum. The concept of angular momentum of phonon is discussed by Zhang and Niu^{75,77)} We

call the phonon with the angular momentum “chiral phonon”. Here we discuss the angular momentum of phonon around the z axis and consider the phonon vibration in xy plane: phonon eigen vector $\boldsymbol{\epsilon} = (x_1, y_1, x_2, y_2, \dots, x_n, y_n)$ where n is the number of atoms in the unit cell. In order to represent the angular momentum of phonon more explicitly, we use the basis of phonon eigen vectors for circular polarization as $|R_1\rangle \equiv \frac{1}{\sqrt{2}}(1, i, 0, 0, \dots)$, $|L_1\rangle \equiv \frac{1}{\sqrt{2}}(1, -i, 0, 0, \dots)$, $|R_2\rangle \equiv \frac{1}{\sqrt{2}}(0, 0, 1, i, \dots)$, $|L_2\rangle \equiv \frac{1}{\sqrt{2}}(0, 0, 1, -i, \dots)$, Then the phonon eigen vector $\boldsymbol{\epsilon}$ is written by

$$\boldsymbol{\epsilon} = \sum_{\alpha=1}^n \epsilon_{R\alpha} |R_\alpha\rangle + \epsilon_{L\alpha} |L_\alpha\rangle, \quad (1.20)$$

where $\epsilon_{R\alpha}$ ($\epsilon_{L\alpha}$), α , n are the coefficient for right- (left-) handed circular polarized chiral phonon, the label of atom in the unit cell, the number of atom in the unit cell, respectively. The coefficients $\epsilon_{R\alpha}$ and $\epsilon_{L\alpha}$ are, respectively, given by

$$\epsilon_{R\alpha} = \langle R_\alpha | \boldsymbol{\epsilon} \rangle, \quad (1.21)$$

$$\epsilon_{L\alpha} = \langle L_\alpha | \boldsymbol{\epsilon} \rangle. \quad (1.22)$$

By using $\epsilon_{R\alpha}$ and $\epsilon_{L\alpha}$ in Eq. (1.21) and (1.22), the circular polarization of phonon along the z direction s_{ph}^z is defined by⁷⁵⁾

$$s_{\text{ph}}^z = \sum_{\alpha=1}^n (|\epsilon_{R\alpha}|^2 - |\epsilon_{L\alpha}|^2). \quad (1.23)$$

When the phonon exchange the angular momentum in the Raman scattering process, s_{ph}^z in Eq. (1.23) has the finite value. In Fig. 1-12, we plot the s_{ph}^z in Eq. (1.23) for graphene and monolayer MoS₂. In the case of graphene, s_{ph}^z is always zero due to the existence of inversion symmetry. This means that the phonons in graphene do not have the angular momentum and usually can not exchange the helicity of light in Raman scattering process. In the case of MoS₂, s_{ph}^z of the most phonon modes around the K point have finite value. This result is consistent with the fact that the valley-selective optical transition by σ_- (σ_+) light can occur in the K (K') point. When the electron at the K point is excited by the σ_- light and scattered to the K' point by the K point phonon which exchanges the angular momentum, optical transition of scattered electron at the K' point has the helicity of σ_+ (helicity switching).

It should be noted that the G band in graphene and IMC mode in monolayer MoS₂ correspond to the first-order Raman process, in which only the Γ point phonon contributes to the Raman scattering. From the calculated results in Fig. 1-12, the Γ

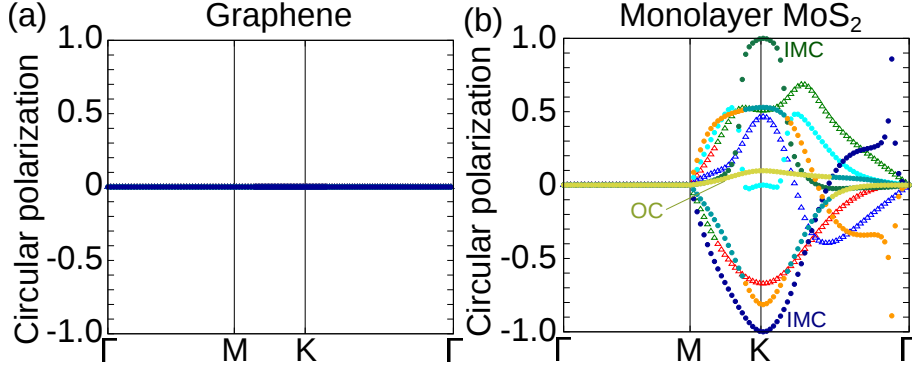


Figure 1-12: (a)-(b) Circular polarization of phonon in (a) graphene and (b) monolayer MoS₂. The circle (triangle) indicates the optical (acoustic) phonon mode.

point phonons do not have the circular polarization ($s_{\text{ph}}^z = 0$). It means that $|L\rangle$ and $|R\rangle$ have equal contributions to the eigen vectors of the phonon. The degenerate eigen vectors are written in orthogonal form by

$$\epsilon_1 = \frac{1}{\sqrt{2}}(|R\rangle + |L\rangle), \quad (1.24)$$

$$\epsilon_2 = \frac{1}{\sqrt{2}}(|R\rangle - |L\rangle). \quad (1.25)$$

The degenerate eigen vectors can be reconstructed by the unitary transformation as

$$\epsilon'_1 = \frac{1}{\sqrt{2}}(\epsilon_1 + \epsilon_2) = |R\rangle, \quad (1.26)$$

$$\epsilon'_2 = \frac{1}{\sqrt{2}}(\epsilon_1 - \epsilon_2) = |L\rangle, \quad (1.27)$$

which means that the s_{ph}^z can be determined arbitrarily only for the degenerate state and can have the circular polarization which is nothing but the angular momentum. The doubly-degenerate phonon mode at the Γ point can have the angular momentum and the conservation of angular momentum is satisfied in the Raman process for the G band of graphene or IMC mode of MoS₂.

Based on the discussion of chiral phonon with the angular momentum, Zhang and Niu predicted that helicity exchange can be observed in the doubly-degenerate G band in gapped graphene by considering the conservation of angular momentum.⁷⁵⁾ However, the helicity exchange would occur in not only gapped graphene, but also in gapless graphene since the shape of Raman tensor for the G band in graphene is same with IMC mode in TMDs as shown in Eq. (1.13). Further, we will show the phenomena of

helicity exchange can occur even in nondegenerate phonon, by quantitative calculation to understand the detail and the mechanism of helicity-resolved Raman scattering.

In Chapter 5, we will explain that we develop the programs to calculate the first-order resonant Raman spectra by first-principles calculation and perform the calculation for TMDs and graphene. Using the calculated results, we discuss the mechanism of helicity-resolved Raman spectra of TMDs and graphene in Chapter 5.

Chapter 2

Methods to calculate optical absorption and Raman spectra

Electrons in a material can interact with photons, phonons (lattice vibrations), other electrons (Coulomb interaction), etc. Therefore, electron-photon and electron-phonon interactions are essential to discuss the optical properties. In this chapter, we present the basic formulation to calculate the electron-photon and electron-phonon matrix elements.

2.1 Time-dependent perturbation theory

Light is an electro-magnetic wave vibrating as a function of time. We can discuss the interaction associated with the light by using time-dependent perturbation theory. In this section, we derive the transition probability from i to f state up to third-order perturbation which is related to the first-order Raman scattering.

2.1.1 Time-dependent perturbation theory

We start from the Hamiltonian with the time-dependent perturbation term $H'(t)$ as,

$$H(t) = H_0 + H'(t), \quad (2.1)$$

where H_0 is the time-independent unperturbed Hamiltonian. The time-dependent eigenstate $|\Psi(t)\rangle$ can be described by the time-dependent Schrödinger equation as follows,

$$i\hbar \frac{\partial}{\partial t} |\Psi(t)\rangle = H(t) |\Psi(t)\rangle. \quad (2.2)$$

We define the eigen state $|m\rangle$ with the eigen energy E_m for unperturbed Hamiltonian H_0 ;

$$H_0|m\rangle = E_m|m\rangle. \quad (2.3)$$

We note that the H_0 is the Hermitian operator and then the eigen function of H_0 is expressed by complete orthonormal set as follows,

$$\langle n|m\rangle = \delta_{nm}, \quad (2.4)$$

$$\sum_m |m\rangle\langle m| = 1. \quad (2.5)$$

We expand the time-dependent eigen state $|\Psi(t)\rangle$ by the orthonormal complete set as follows,

$$|\Psi(t)\rangle = \sum_m a_m(t)e^{\frac{E_m}{i\hbar}t}|m\rangle, \quad (2.6)$$

where $a_m(t)$ is the time-dependent expansion coefficient. Substituting Eq. (2.6) into (2.2), the right- and left-hand sides of Eq. (2.2) are, respectively, written by

$$i\hbar\frac{\partial}{\partial t}|\Psi(t)\rangle = \sum_m \left\{ i\hbar\frac{\partial a_m(t)}{\partial t} + E_m a_m(t) \right\} e^{\frac{E_m}{i\hbar}t}|m\rangle, \quad (2.7)$$

$$\begin{aligned} H(t)|\Psi(t)\rangle &= (H_0 + H'(t))|\Psi(t)\rangle \\ &= \sum_m (E_m + H'(t))a_m(t)e^{\frac{E_m}{i\hbar}t}|m\rangle. \end{aligned} \quad (2.8)$$

Then, by using Eqs. (2.4), (2.5), (2.7), and (2.8), the time-dependent Schrödinger equation in Eq. (2.2) is further calculated as follows,

$$\begin{aligned} i\hbar \sum_m \frac{\partial a_m(t)}{\partial t} e^{\frac{E_m}{i\hbar}t}|m\rangle &= \sum_m H'(t)a_m(t)e^{\frac{E_m}{i\hbar}t}|m\rangle \\ \sum \left\{ i\hbar\frac{\partial a_n(t)}{\partial t} e^{\frac{E_n}{i\hbar}t} - \sum_m a_m(t)e^{\frac{E_m}{i\hbar}t}\langle n|H'(t)|m\rangle \right\} |n\rangle &= 0. \end{aligned} \quad (2.9)$$

Multiplying $\langle n|$ from the left side of Eq. (2.9), we obtain

$$\frac{\partial a_n(t)}{\partial t} = \frac{1}{i\hbar} \sum_m a_m(t)e^{\frac{E_m - E_n}{i\hbar}t}\langle n|H'(t)|m\rangle. \quad (2.10)$$

The time-dependent coefficient $a_n(t)$ can be obtained by integrating Eq. (2.10) from t_0 to t and we obtain

$$a_n(t) = a_n(t_0) + \frac{1}{i\hbar} \sum_m \int_{t_0}^t dt' a_m(t') e^{\frac{E_m^{(0)} - E_n^{(0)}}{i\hbar} t'} \langle n | H'(t') | m \rangle. \quad (2.11)$$

In Eq. (2.11), substituting the left hand side to right hand side iteratively, we obtain the expression of $a_n(t)$ as follows;

$$\begin{aligned} a_n(t) &= a_n(t_0) + \frac{1}{i\hbar} \sum_m \int_{t_0}^t dt' a_m(t_0) e^{\frac{E_m - E_n}{i\hbar} t'} \langle n | H'(t') | m \rangle \\ &+ \frac{1}{(i\hbar)^2} \sum_m \sum_{m'} \int_{t_0}^t dt' \int_{t_0}^{t'} dt'' a_{m'}(t_0) e^{\frac{E_{m'} - E_m}{i\hbar} t} e^{\frac{E_m - E_n}{i\hbar} t'} \langle n | H'(t') | m \rangle \langle m | H'(t'') | m' \rangle \\ &+ \frac{1}{(i\hbar)^3} \sum_m \sum_{m'} \sum_{m''} \int_{t_0}^t dt' \int_{t_0}^{t'} dt'' \int_{t_0}^{t''} dt''' a_{m''}(t_0) e^{\frac{E_{m''} - E_{m'}}{i\hbar} t} e^{\frac{E_{m'} - E_m}{i\hbar} t'} e^{\frac{E_m - E_n}{i\hbar} t''} \\ &\times \langle n | H'(t') | m \rangle \langle m | H'(t'') | m' \rangle \langle m' | H'(t''') | m'' \rangle \\ &+ \dots \end{aligned} \quad (2.12)$$

The first, second, third, and fourth terms in Eq. (2.12) are the zeroth-, first-, second-, and third-order perturbation coefficients ($a_n^{(0)}(t)$, $a_n^{(1)}(t)$, $a_n^{(2)}(t)$, and $a_n^{(3)}(t)$), respectively. The $a_n(t_0)$ is determined by the initial condition. The initial state at the time t_0 is the eigen state of H_0 , that is,

$$|\Psi(t_0)\rangle = \sum_n a_n(t_0) e^{\frac{E_n}{i\hbar} t_0} |n\rangle = |i\rangle. \quad (2.13)$$

Under this initial condition, we can obtain $a_n(t_0)$ as follows,

$$a_n(t_0) = \delta_{ni}. \quad (2.14)$$

Thus, the first-, second-, and third-order perturbation coefficients in Eq. (2.12), $a_n^{(1)}(t)$, $a_n^{(2)}(t)$, and $a_n^{(3)}(t)$ are, respectively, written by

$$a_n^{(1)}(t) = \frac{1}{i\hbar} \int_{t_0}^t dt' e^{\frac{E_i - E_n}{i\hbar} t'} \langle n | H'(t') | i \rangle, \quad (2.15)$$

$$a_n^{(2)}(t) = \frac{1}{(i\hbar)^2} \sum_m \int_{t_0}^t dt' \int_{t_0}^{t'} dt'' e^{\frac{E_i - E_m}{i\hbar} t''} e^{\frac{E_m - E_n}{i\hbar} t'} \langle n | H'(t') | m' \rangle \langle m' | H'(t'') | i \rangle \quad (2.16)$$

$$a_m^{(3)}(t) = \frac{1}{(i\hbar)^3} \sum_m \sum_{m'} \int_{t_0}^t dt' \int_{t_0}^{t'} dt'' \int_{t_0}^{t''} dt''' e^{\frac{E_i - E_{m'}}{i\hbar} t'''} e^{\frac{E_{m'} - E_m}{i\hbar} t''} e^{\frac{E_m - E_n}{i\hbar} t'} \times \langle n | H'(t') | m \rangle \langle m | H'(t'') | m' \rangle \langle m' | H'(t''') | i \rangle. \quad (2.17)$$

2.1.2 Time-dependent periodic perturbation

We assume the time-dependent periodic perturbation with frequency ω , which is written by

$$H'(t) = V e^{-i\omega t} + V^\dagger e^{i\omega t}. \quad (2.18)$$

This perturbation Hamiltonian can be applied to a vibrating electro-magnetic wave or phonon vibration which is discussed in Section 2.2 and 2.4. Using the perturbation Hamiltonian in Eq. (2.18), the first-order perturbation coefficient $a_n^{(1)}(t)$ in Eq. (2.15) is written by

$$a_n^{(1)}(t) = \frac{1}{i\hbar} \langle n | V | i \rangle \int_{t_0}^t dt' e^{\frac{i}{\hbar}(E_n - E_i - \hbar\omega)t'} + \frac{1}{i\hbar} \langle n | V^\dagger | i \rangle \int_{t_0}^t dt' e^{\frac{i}{\hbar}(E_n - E_i + \hbar\omega)t'}. \quad (2.19)$$

The integration in Eq. (2.19) is calculated as follows,

$$\begin{aligned} \int_{t_0}^t dt' e^{\frac{i}{\hbar}(E_n - E_i \pm \hbar\omega)t'} &= \frac{i}{\hbar} (E_n - E_i \pm \hbar\omega) \left(e^{\frac{i}{\hbar}(E_n - E_i \pm \hbar\omega)t'} - e^{\frac{i}{\hbar}(E_n - E_i \pm \hbar\omega)t_0} \right) \\ &= \frac{2\hbar}{E_n - E_i \pm \hbar\omega} \sin \left\{ \frac{E_n - E_i \pm \hbar\omega}{2\hbar} (t - t_0) \right\} e^{\frac{E_n - E_i \pm \hbar\omega}{2\hbar} (t + t_0)}. \end{aligned} \quad (2.20)$$

The expression in Eq. (2.20) is for finite time while we consider the limit of $t \rightarrow \infty$ and $t_0 \rightarrow -\infty$ in the following discussion. Under the limit of $t \rightarrow \infty$ and $t_0 \rightarrow -\infty$, the integration in Eq. (2.19) is expressed by the delta function as follows,

$$\int_{-\infty}^{\infty} dt' e^{\frac{i}{\hbar}(E_n - E_i \pm \hbar\omega)t'} = 2\pi\hbar\delta(E_n - E_i \pm \hbar\omega). \quad (2.21)$$

Then, the transition probability from the initial state $|i\rangle$ to another state $|n\rangle$ by the first-order time-dependent perturbation with perturbation Hamiltonian in Eq. (2.18)

is calculated under the limit of $t \rightarrow \infty$ and $t_0 \rightarrow -\infty$:

$$\begin{aligned}
|a_n^{(1)}|^2 &= \left| \frac{1}{i\hbar} \langle n|V|i\rangle \int_{-\infty}^{\infty} dt' e^{\frac{i}{\hbar}(E_n - E_i - \hbar\omega)t'} + \frac{1}{i\hbar} \langle n|V^\dagger|i\rangle \int_{-\infty}^{\infty} dt' e^{\frac{i}{\hbar}(E_n - E_i + \hbar\omega)t'} \right|^2 \\
&= (2\pi)^2 \left| \langle n|V|i\rangle \delta(E_n - E_i - \hbar\omega) + \langle n|V^\dagger|i\rangle \delta(E_n - E_i + \hbar\omega) \right|^2 \\
&= (2\pi)^2 \delta(0) \left(|\langle n|V|i\rangle|^2 \delta(E_n - E_i - \hbar\omega) + |\langle n|V^\dagger|i\rangle|^2 \delta(E_n - E_i + \hbar\omega) \right).
\end{aligned} \tag{2.22}$$

In the derivation from the second to the third line in Eq. (2.22), we use

$$|\delta(E_n - E_i \pm \hbar\omega)|^2 = \delta(0)\delta(E_n - E_i \pm \hbar\omega), \tag{2.23}$$

$$\delta(E_n - E_i + \hbar\omega)\delta(E_n - E_i - \hbar\omega) = 0. \tag{2.24}$$

The factor $2\pi\hbar\delta(0) = \int_{-\infty}^{\infty} dt$ is the time from $-\infty$ to ∞ and thus we can obtain the transition probability from the initial (i) to the final (f) state per unit time W^{fi} by dividing Eq. (2.22) by $2\pi\hbar\delta(0)$:

$$\begin{aligned}
W^{fi(1)} &= \frac{|a_f^{(1)}|^2}{2\pi\hbar\delta(0)} \\
&= \frac{2\pi}{\hbar} \left(|\langle f|V|i\rangle|^2 \delta(E_f - E_i - \hbar\omega) + |\langle f|V^\dagger|i\rangle|^2 \delta(E_f - E_i + \hbar\omega) \right).
\end{aligned} \tag{2.25}$$

This result is the so-called Fermi's golden rule that gives the transition probability from the i to f state within the first-order time-dependent perturbation theory. Optical absorption is a process where an electron excites from the valence to conduction band by interacting with light. We can directly calculate the optical absorption probability by Fermi's golden rule.

2.1.3 Second- and third-order time-dependent perturbation theory

The transition probability from the i to f state by mediating the intermediate state m is calculated by higher-order time-dependent perturbation theory. The first-order Raman scattering process discussed in Sec. 2.5 is calculated by the third-order perturbation theory. Here we consider the perturbation Hamiltonian as harmonic perturbation that gradually switches on, more generally defined by:

$$H'(t) = e^{\eta_1 t} V_1 e^{-i\omega_1 t} + e^{\eta_2 t} V_2 e^{-i\omega_2 t} + \dots, \tag{2.26}$$

where η_1, η_2, \dots are the factors to switch on the potential gradually and approach 0 in the limit. Using the perturbation Hamiltonian in Eq. (2.26), the second-order perturbation coefficient $a_n^{(2)}(t)$ in Eq. (2.16) is written by

$$\begin{aligned} a_n^{(2)}(t) &= \frac{1}{(i\hbar)^2} \sum_m \int_{t_0}^t dt' \int_{t_0}^{t'} dt'' e^{\frac{i}{\hbar}(E_m - E_i - \hbar\omega_1 - i\hbar\eta_1)t''} e^{\frac{i}{\hbar}(E_n - E_m - \hbar\omega_1 - i\hbar\eta_1)t'} \langle n|V_1|m\rangle \langle m|V_1|i\rangle \\ &\quad + \frac{1}{(i\hbar)^2} \sum_m \int_{t_0}^t dt' \int_{t_0}^{t'} dt'' e^{\frac{i}{\hbar}(E_m - E_i - \hbar\omega_1 - i\hbar\eta_1)t''} e^{\frac{i}{\hbar}(E_n - E_m - i\hbar\omega_2 - \hbar\eta_2)t'} \langle n|V_2|m\rangle \langle m|V_1|i\rangle \\ &\quad + \dots \end{aligned} \quad (2.27)$$

The second-order perturbation associated with V_1 and V_2 , $a_{n,V_1,V_2}^{(2)}(t)$ (second term in Eq. (2.27)) is further calculated as follows,

$$\begin{aligned} &a_{n,V_1,V_2}^{(2)}(t) \\ &= \frac{1}{(i\hbar)^2} \sum_m \int_{t_0}^t dt' \int_{t_0}^{t'} dt'' e^{\frac{i}{\hbar}(E_m - E_i - \hbar\omega_1 - i\hbar\eta_1)t''} e^{\frac{i}{\hbar}(E_n - E_m - \hbar\omega_2 - \hbar\eta_2)t'} \langle n|V_2|m\rangle \langle m|V_1|i\rangle \\ &= \frac{1}{(i\hbar)^2} \sum_m (-i\hbar) \frac{\langle n|V_2|m\rangle \langle m|V_1|i\rangle}{E_m - E_i - \hbar\omega_1 - i\hbar\eta_1} \\ &\quad \times \int_{t_0}^t dt' \left\{ e^{\frac{i}{\hbar}(E_m - E_i - \hbar\omega_1 - i\hbar\eta_1)t'} - e^{\frac{i}{\hbar}(E_m - E_i - \hbar\omega_1 - i\hbar\eta_1)t_0} \right\} e^{\frac{i}{\hbar}(E_n - E_m - \hbar\omega_2 - \hbar\eta_2)t'} \\ &= \frac{1}{(i\hbar)^2} \sum_m (-i\hbar) \frac{\langle n|V_2|m\rangle \langle m|V_1|i\rangle}{E_m - E_i - \hbar\omega_1 - i\hbar\eta_1} \\ &\quad \times \left\{ \int_{t_0}^t e^{\frac{i}{\hbar}(E_n - E_i - \hbar\omega_1 - \hbar\omega_2 - i\hbar(\eta_1 + \eta_2))t'} dt' + e^{\eta_1 t_0} e^{\frac{i}{\hbar}(E_m - E_i - \hbar\omega_1)t_0} \int_{t_0}^t e^{\frac{i}{\hbar}(E_n - E_m - \hbar\omega_2 - \hbar\eta_2)t'} dt' \right\}. \end{aligned} \quad (2.28)$$

Then, we take the limit of $t_0 \rightarrow -\infty, t \rightarrow \infty$ and after that, take the limit of $\eta_1 \rightarrow 0, \eta_2 \rightarrow 0$ in the integral. The second term in Eq. (2.28) becomes zero in this limit and we obtain,

$$\begin{aligned} a_{n,V_1,V_2}^{(2)} &= \frac{i}{\hbar} \sum_m \frac{\langle n|V_2|m\rangle \langle m|V_1|i\rangle}{E_m - E_i - \hbar\omega_1 - i\hbar\eta_1} \int_{-\infty}^{\infty} e^{\frac{i}{\hbar}(E_n - E_i - \hbar\omega_1 - \hbar\omega_2)t'} dt' \\ &= 2\pi i \sum_m \frac{\langle n|V_2|m\rangle \langle m|V_1|i\rangle}{E_m - E_i - \hbar\omega_1 - i\hbar\eta_1} \delta(E_n - E_i - \hbar\omega_1 - \hbar\omega_2). \end{aligned} \quad (2.29)$$

All other terms in Eq. (2.27) are calculated similarly. The transition probability $|a_{n,V_1,V_2}^{(2)}|^2$ is given by using Eq. (2.23) and (2.29) as follows,

$$|a_{n,V_1,V_2}^{(2)}|^2 = (2\pi)^2 \delta(0) \left| \sum_m \frac{\langle n|V_2|m\rangle \langle m|V_1|i\rangle}{E_m - E_i - \hbar\omega_1 - i\hbar\eta_1} \right|^2 \delta(E_n - E_i - \hbar\omega_1 - \hbar\omega_2). \quad (2.30)$$

The second-order transition probability from i to f state associated with V_1 and V_2 per unit time, $W_{V_1,V_2}^{fi(2)}$ is given by dividing Eq. (2.30) by $2\pi\hbar\delta(0)$ as follows,

$$\begin{aligned} W_{V_1,V_2}^{fi(2)} &= \frac{2\pi\hbar\delta(0)}{|a_{f,V_1,V_2}^{(2)}|^2} \\ &= \frac{2\pi}{\hbar} \left| \sum_m \frac{\langle f|V_2|m\rangle \langle m|V_1|i\rangle}{E_m - E_i - \hbar\omega_1 - i\gamma_1} \right|^2 \delta(E_f - E_i - \hbar\omega_1 - \hbar\omega_2). \end{aligned} \quad (2.31)$$

where we use the notation $\gamma_1 = \hbar\eta_1$ with the dimension of the energy, which gives the finite resonance window in the resonance condition of Eq. (2.31).

The third order time-dependent perturbation is calculated by the same with second order perturbation. Then the third order transition probability from i to f state associated with V_1 , V_2 , and V_3 per unit time, $W_{V_1,V_2,V_3}^{fi(3)}$ is given by

$$\begin{aligned} W_{V_1,V_2,V_3}^{fi(3)} &= \frac{2\pi}{\hbar} \left| \sum_{m,m'} \frac{\langle f|V_3|m'\rangle \langle m'|V_2|m\rangle \langle m|V_1|i\rangle}{(E_m - E_i - \hbar\omega_1 - i\gamma_1)(E_{m'} - E_m - \hbar\omega_2 - i\gamma_2)} \right|^2 \\ &\quad \times \delta(E_f - E_i - \hbar\omega_1 - \hbar\omega_2 - \hbar\omega_3). \end{aligned} \quad (2.32)$$

The transition probability of the first order Raman scattering discussed in Sec. 2.5 is calculated by using Eq. (2.32) with assumptions that: (1) the initial and final state is same ($i = f$), and (2) V_1 (V_3) and V_2 are electron-photon and electron-phonon interaction, respectively.

2.2 Electron-photon interaction

In this section, we discuss the electron-photon interaction which is directly related to the optical absorption.

2.2.1 Derivation of electron-photon matrix element

In order to get the perturbation Hamiltonian for the electron-photon interaction, we start from the Hamiltonian of an electron in the electro-magnetic field as follows,

$$\begin{aligned} H &= \frac{1}{2m}(-i\hbar\nabla - e\mathbf{A})^2 + V(\mathbf{r}) + e\phi \\ &= \frac{1}{2m}(-\hbar^2\nabla^2 - ie\hbar\nabla \cdot \mathbf{A} - 2ie\hbar\mathbf{A} \cdot \nabla + e^2(\mathbf{A})^2) + V(\mathbf{r}) + e\phi. \end{aligned} \quad (2.33)$$

We set the scalar potential ϕ as zero and employ the Coulomb gage ($\nabla \cdot \mathbf{A} = 0$). Neglecting the second order term of \mathbf{A} , finally the Hamiltonian in Eq. (2.33) is written by

$$\begin{aligned} H &= -\frac{\hbar^2}{2m}\nabla^2 + V(\mathbf{r}) - \frac{ie\hbar}{m}\mathbf{A} \cdot \nabla \\ &= H_0 + H_{\text{opt}}, \end{aligned} \quad (2.34)$$

where unperturbed Hamiltonian H_0 and perturbation Hamiltonian for electron-photon interaction H_{opt} are, respectively, written by

$$H_0 = -\frac{\hbar^2}{2m}\nabla^2 + V(\mathbf{r}), \quad (2.35)$$

$$H_{\text{opt}} = -\frac{ie\hbar}{m}\mathbf{A} \cdot \nabla. \quad (2.36)$$

Using the definition of vector potential $\mathbf{B} = \nabla \times \mathbf{A}$ and the Maxwell equation in vacuum $\nabla \times \mathbf{B} = \mu_0\mathbf{j} + \mu_0\varepsilon_0\frac{\partial\mathbf{E}}{\partial t}$ with the current density $\mathbf{j} = 0$, we obtain

$$\nabla \times \nabla \times \mathbf{A} = \nabla(\nabla \cdot \mathbf{A}) - \Delta\mathbf{A} = \mu_0\varepsilon_0\frac{\partial\mathbf{E}}{\partial t}. \quad (2.37)$$

We assume a harmonic electric field described by $\mathbf{E} = E_0 \exp\{i(\mathbf{k}_{\text{opt}} \cdot \mathbf{r} \pm \omega t)\}\mathbf{P}$ with the polarization vector \mathbf{P} which is the unit vector to describe the direction of optical electric field, and the vector potential \mathbf{A} also has same wave number and frequency with the electric field. Using the relation $\omega = ck_{\text{opt}}$, $c = 1/\sqrt{\varepsilon_0\mu_0}$, the laser intensity $I_0 = E_0^2/\mu_0c$, and the assumption of Coulomb gage $\nabla \cdot \mathbf{A} = 0$, we can obtain the form of the vector potential \mathbf{A} as follows,

$$\mathbf{A} = \frac{i}{\omega}\sqrt{\frac{I_0}{c\varepsilon_0}} \exp\{i(\mathbf{k}_{\text{opt}} \cdot \mathbf{r} \pm \omega t)\}\mathbf{P}. \quad (2.38)$$

Thus the electron-photon matrix element M_{opt}^{fi} for a pair of initial (i) and final (f) state is written by using Eqs. (2.36) and (2.38) as follows,

$$\begin{aligned}
M_{\text{opt}}^{fi} &= \langle f | H_{\text{opt}} | i \rangle \\
&= -\frac{ie\hbar}{m} \langle f | \mathbf{A} \cdot \nabla | i \rangle \\
&= \frac{e\hbar}{m\omega} \sqrt{\frac{I}{c\varepsilon_0}} \exp\{i(\omega_f - \omega_i \pm \omega)t\} \langle f | \nabla | i \rangle \cdot \mathbf{P} \\
&= \frac{e\hbar}{m\omega} \sqrt{\frac{I}{c\varepsilon_0}} \exp\{i(\omega_f - \omega_i \pm \omega)t\} \mathbf{D}^{fi} \cdot \mathbf{P}.
\end{aligned} \tag{2.39}$$

In Eq. (2.39), we define the dipole vector \mathbf{D}^{fi} as follows⁷⁸⁾;

$$\mathbf{D}^{fi} = \langle f | \nabla | i \rangle. \tag{2.40}$$

From the third line to fourth line in Eq. (2.39), we assume that the wave number in the crystal is sufficiently larger than the wave number of the light ($|\mathbf{k}| \gg |\mathbf{k}_{\text{opt}}|$) and thus we can take the vector potential \mathbf{A} out of the integral. The positive (negative) sign in Eq. (2.39) corresponds to the emission (absorption) of photon.

We can calculate the electron-photon matrix element M_{opt}^{fi} if we obtain the dipole vector \mathbf{D}^{fi} as shown in Eq. (2.40). The dipole vector becomes a function of the wave number \mathbf{k} of the wave function in the crystal ($\mathbf{D}^{fi} = \mathbf{D}^{fi}(\mathbf{k})$) since the wave function of the crystal is written as a function of \mathbf{k} . When the wave function is expanded by the basis set of plane wave, the dipole vector is easily calculated. We write the wave function expanded by plane wave as follows,

$$\Psi^n(\mathbf{r}, \mathbf{k}) = \sum_{\mathbf{G}} C_{\mathbf{G}}^n(\mathbf{k}) \exp\{i(\mathbf{k} + \mathbf{G})\mathbf{r}\}, \tag{2.41}$$

where \mathbf{G} and $C_{\mathbf{G}}^n(\mathbf{k})$ are, respectively, the reciprocal lattice vector and the coefficient for plane wave basis with the wave number $\mathbf{k} + \mathbf{G}$. Substituting the wave function in Eq. (2.41) into Eq. (2.40), the $\mathbf{D}^{fi}(\mathbf{k})$ is expanded as follows,

$$\begin{aligned}
\mathbf{D}^{fi}(\mathbf{k}) &= \sum_{\mathbf{G}} \sum_{\mathbf{G}'} C_{\mathbf{G}'}^f(\mathbf{k})^* C_{\mathbf{G}}^i(\mathbf{k})(\mathbf{k} + \mathbf{G}) \int \exp\{i(\mathbf{G} - \mathbf{G}')\mathbf{r}\} d\mathbf{r} \\
&= \sum_{\mathbf{G}} \sum_{\mathbf{G}'} C_{\mathbf{G}'}^f(\mathbf{k})^* C_{\mathbf{G}}^i(\mathbf{k})(\mathbf{k} + \mathbf{G}) \delta_{\mathbf{G}, \mathbf{G}'} \\
&= \sum_{\mathbf{G}} C_{\mathbf{G}}^f(\mathbf{k})^* C_{\mathbf{G}}^i(\mathbf{k})(\mathbf{k} + \mathbf{G}).
\end{aligned} \tag{2.42}$$

2.2.2 Polarization vector (the Jones vector)

The polarization vector (or the Jones vector) \mathbf{P} in Eq. (2.38) describes the direction of the electric field of light. General expression of \mathbf{P} for electro-magnetic wave propagating in the z direction is written as,

$$\mathbf{P} = \frac{1}{\sqrt{P_x^2 + P_y^2}} \begin{pmatrix} P_x \\ P_y e^{i\phi} \\ 0 \end{pmatrix}, \quad (2.43)$$

where P_x (P_y) and ϕ are, respectively, the amplitude of x (y) component defined by real number and the phase difference between the x and y components of \mathbf{P} . The linear polarized light can be expressed by $\phi = 0$ or π . In the case of $\phi = 0$, polarization \mathbf{P} vector is written as

$$\mathbf{P} = \frac{1}{\sqrt{P_x^2 + P_y^2}} \begin{pmatrix} P_x \\ P_y \\ 0 \end{pmatrix}, \quad (2.44)$$

and x -polarized (y -polarized) light corresponds to $P_y = 0$ ($P_x = 0$). The general case of $\phi \neq 0$ is called as elliptical polarization. In particular \mathbf{P} for $\phi = \frac{\pi}{2}$ ($\phi = -\frac{\pi}{2}$) with $P_x = P_y$ corresponds to left- (right-) handed circular polarized light that is defined by σ_+ (σ_-). In this case, polarization vectors for σ_+ and σ_- light are written, respectively, by

$$\mathbf{P}_{\sigma_+} = \frac{1}{\sqrt{2}} \begin{pmatrix} 1 \\ i \\ 0 \end{pmatrix} \quad (\sigma_+ : \phi = \frac{\pi}{2}), \quad (2.45)$$

$$\mathbf{P}_{\sigma_-} = \frac{1}{\sqrt{2}} \begin{pmatrix} 1 \\ -i \\ 0 \end{pmatrix} \quad (\sigma_- : \phi = -\frac{\pi}{2}). \quad (2.46)$$

2.3 Optical absorption

2.3.1 Absorption coefficient and Fermi's Golden rule

Using electron-photon matrix element, the optical absorption probability per a unit time is calculated by Fermi's golden rule shown in Eq. (2.25). The transition probability by the electron-photon interaction per unit time between the states i and f is written

by

$$W^{fi} = \frac{2\pi}{\hbar} \left| M_{\text{opt}}^{fi} \right|^2 \delta(E_f - E_i \pm \hbar\omega). \quad (2.47)$$

The absorption coefficients α and β for the material sample with depth L are defined by the Lambert-Beer law as follows,

$$I = I_0 e^{-\alpha L} = I_0 10^{-\beta L}, \quad (2.48)$$

or

$$\alpha = -\frac{1}{L} \ln \left(\frac{I}{I_0} \right), \beta = -\frac{1}{L} \log_{10} \left(\frac{I}{I_0} \right), \quad (2.49)$$

where I_0 and I are, respectively, the optical intensities of the incident light and the light after transmitting the sample by the length L . The coefficients α and β are material-specific constants in units of nm^{-1} or m^{-1} to describe how much length the light propagates in the material. Then the relation between the absorbance defined by $A = -\log_{10}(I/I_0)$ and the absorption coefficients α and β is given as follows,

$$A = \log_{10} e \cdot \alpha L = \beta L. \quad (2.50)$$

The units of absorbance is dimensionless. Absorbance depends on the thickness of the sample while absorption coefficient is material-specific. In this thesis, we adopt the definition of α in Eq. (2.48) and (2.49) as absorption coefficient. Absorption coefficient α is related to the transition probability of Fermi's Golden rule in Eq. (2.25). We derive the relation between the absorption coefficient α and the transition probability W^{fi} as below. The energy loss per unit volume P_{loss}/V [W] in a material is written by the α and the intensity of light I [W/m^2] as follows,

$$\frac{P_{\text{loss}}}{V} = I\alpha, \quad (2.51)$$

where V is the volume of the sample. The energy loss P_{loss} is also given by using absorption rate R [1/s] as follows,

$$P_{\text{loss}} = R\hbar\omega, \quad (2.52)$$

where the absorption rate R is described by transition probability W^{fi} as follows,

$$R = \sum_{i,f} W^{fi} = \frac{2\pi}{\hbar} \sum_{i,f} \left| M_{\text{opt}}^{fi} \right|^2 \delta(E_f - E_i - \hbar\omega). \quad (2.53)$$

The summation in Eq. (2.53) is taken over all occupied i and unoccupied f states, including the information of the number of electron. Using Eqs. (2.51), (2.52), and (2.53), we obtain

$$\begin{aligned} \alpha &= \frac{P_{\text{loss}}}{IV} = \frac{\hbar\omega}{IV} R \\ &= \frac{2\pi\omega}{IV} \sum_{i,f} \left| M_{\text{opt}}^{fi} \right|^2 \delta(E_f - E_i - \hbar\omega). \end{aligned} \quad (2.54)$$

Especially when the electron-photon matrix element is given by the dipole vector as a function of wave number \mathbf{k} , we integrate Eq. (2.54) in the first Brillouin zone. Then using Eq. (2.39) and (2.54), α is given by,

$$\alpha = \frac{e^2 \hbar^2}{4\pi^2 m^2 \omega c \epsilon_0} \sum_{i,f} \int_{\text{BZ}} d^3k \left| \mathbf{P} \cdot \mathbf{D}^{fi}(\mathbf{k}) \right|^2 \delta(E_f - E_i - \hbar\omega). \quad (2.55)$$

2.3.2 Relationship between optical absorption, refractive index, and dielectric constant

The absorption coefficient α is related to the refraction index or dielectric constant, too. We show the derivation of these relationships as below. We start from the expression of the electric field of light propagating to z direction with wave number k_{opt} and frequency ω in continuous medium as follows,

$$E = E_0 e^{-i\omega t - ik_{\text{opt}} z}, \quad (2.56)$$

By introducing complex refractive index $\tilde{n} = n + i\kappa$ where n and κ are, respectively, the real and imaginary part that are functions of ω , the velocity of light in the medium v is written by

$$v = \frac{c}{\tilde{n}} = \frac{\omega}{n + i\kappa}, \quad (2.57)$$

and the wave number k_{opt} in the medium can be written by

$$k_{\text{opt}} = \frac{\omega}{v} = \frac{\omega}{c} (n + i\kappa). \quad (2.58)$$

Then the electric field of light in Eq. (2.56) is written by

$$E = E_0 e^{-\kappa\omega z/c} e^{-i\omega t + i n \omega z/c}. \quad (2.59)$$

The intensity of light is given by the square of the absolute value of electric field as follows,

$$I \sim \varepsilon_0 |E|^2 = \varepsilon_0 E_0^2 e^{-2\kappa\omega z/c} = I_0 e^{-2\kappa\omega z/c}. \quad (2.60)$$

Comparing with the definition of absorption coefficient in Eq. (2.48), we obtain

$$\alpha = \frac{2\kappa\omega}{c} = \frac{4\pi\kappa}{\lambda}, \quad (2.61)$$

where λ is the wavelength of light. The imaginary part of complex refractive index κ is related with the optical absorption and we call κ as an extinction function. The dielectric constant is also related with absorption. We consider the complex relative dielectric constant with real (imaginary) part ε'_r (ε''_r),

$$\varepsilon_r = \varepsilon'_r + i\varepsilon''_r. \quad (2.62)$$

Using the Maxwell equation $\nabla \times \mathbf{B} = \varepsilon_r \varepsilon_0 \mu_0 \frac{\partial \mathbf{E}}{\partial t}$, $\nabla \times \mathbf{E} = -\frac{\partial \mathbf{B}}{\partial t}$, $\nabla \cdot \mathbf{E} = \mathbf{0}$, and the expression of the electric field of light in Eq. (2.59), we obtain

$$\nabla \times \nabla \times \mathbf{E} = -\nabla \times \frac{\partial \mathbf{B}}{\partial t} = -\varepsilon_r \varepsilon_0 \mu_0 \frac{\partial^2 \mathbf{E}}{\partial t^2}, \quad (2.63)$$

$$\nabla \times \nabla \times \mathbf{E} = \nabla(\nabla \cdot \mathbf{E}) - \Delta \mathbf{E} = \frac{N^2 \omega^2}{c^2} \mathbf{E}. \quad (2.64)$$

Comparing Eqs. (2.63) and (2.64), we obtain

$$\tilde{n}^2 = \varepsilon_r \quad (2.65)$$

Using Eqs. (2.62) and (2.65), the real and imaginary part of the complex dielectric constant is written by

$$\varepsilon' = n^2 - \kappa^2, \quad (2.66)$$

$$\varepsilon'' = 2n\kappa. \quad (2.67)$$

When we write the explicit form of the n and κ , we can write

$$n = \sqrt{\frac{\sqrt{\varepsilon_r'^2 + \varepsilon_r''^2} + \varepsilon_r'}{2}}, \quad (2.68)$$

$$\kappa = \sqrt{\frac{\sqrt{\varepsilon_r'^2 + \varepsilon_r''^2} - \varepsilon_r'}{2}}. \quad (2.69)$$

Using Eqs.(2.61) and (2.69), absorption coefficient is written up to the first order of ε_r'' as follows,

$$\alpha \sim \frac{\omega}{c} \frac{\varepsilon_r''}{\sqrt{\varepsilon_r'}}. \quad (2.70)$$

The absorption coefficient is proportional to ε_r'' when ε_r'' is sufficiently small compared with ε_r' .

2.4 Electron-phonon interaction

In this section, we briefly discuss about the electron-phonon interaction. The atomic potential is changed by the vibration of neighbor atoms. Thus the interaction between the electron and the ion is modified, too. We call such an interaction as electron-phonon interaction. We assume that the ion at the cite s is located at a position \mathbf{R}_s with a displacement \mathbf{u}_s from its equilibrium position \mathbf{R}_{s0} , that is, $\mathbf{R}_s = \mathbf{R}_{s0} + \mathbf{u}_s$. The atomic potential $V(\mathbf{r} - \mathbf{R}_s)$ is expanded by \mathbf{u}_s for the small amplitude vibration as follows,

$$\begin{aligned} V(\mathbf{r} - \mathbf{R}_s) &= V(\mathbf{r} - \mathbf{R}_{s0} - \mathbf{u}_s) \\ &= V(\mathbf{r} - \mathbf{R}_{s0}) + \mathbf{u}_s \cdot \nabla_{\mathbf{u}_s} V(\mathbf{r} - \mathbf{R}_{s0} - \mathbf{u}_s)|_{\mathbf{u}_s=0} \\ &= V(\mathbf{r} - \mathbf{R}_{s0}) + \mathbf{u}_s \cdot \nabla_{\mathbf{R}_s} V(\mathbf{r} - \mathbf{R}_s)|_{\mathbf{R}_s=\mathbf{R}_{s0}}. \end{aligned} \quad (2.71)$$

The first term in Eq. (2.71) is unperturbed atomic potential and can be treated as the potential for calculating energy band. The second term in Eq. (2.71) is given by an inner product of the atomic vibration and the gradient of the potential $\nabla_{\mathbf{R}_s} V(\mathbf{r} - \mathbf{R}_s)|_{\mathbf{R}_s=\mathbf{R}_{s0}}$. The electron-phonon interaction with $\mathbf{q} = 0$ phonon is calculated by the electron-phonon matrix element,

$$M_{ep}^{fi}(\mathbf{k}', \mathbf{k}) = \sum_s \sqrt{\frac{\hbar}{2M_s\omega_\nu}} \langle \psi^f(\mathbf{k}', \mathbf{r}) | \mathbf{u}_s \cdot \nabla_{\mathbf{R}_s} V(\mathbf{r} - \mathbf{R}_s)|_{\mathbf{R}_s=\mathbf{R}_{s0}} | \psi^i(\mathbf{k}, \mathbf{r}) \rangle \quad (2.72)$$

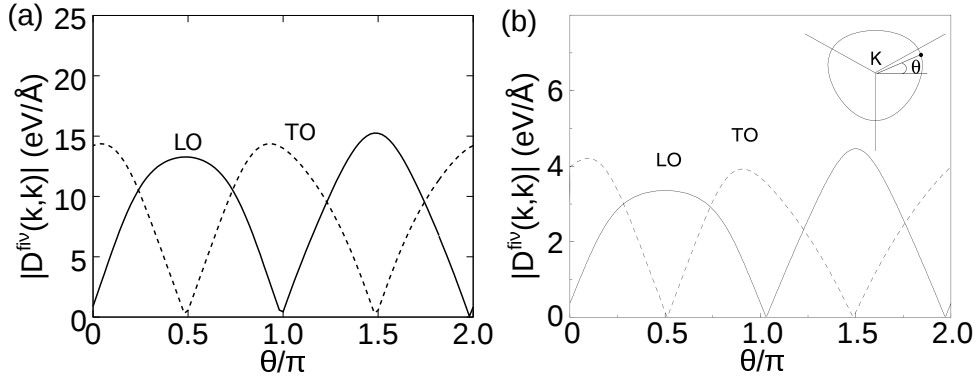


Figure 2-1: Deformation potential $D^{fiv}(\mathbf{k}, \mathbf{k})$ of iTO (dashed line) and LO (solid line) modes for π (valence) and π^* (conduction) bands in graphene (a) extracted from EPW package and (b) calculated by tight-binding method reported by Jiang, *et al.*⁸¹⁾ The plot is on the equi-countour line of the difference of energy between the conduction and valence band $E_c - E_v = 1$ eV [inset of (b)].

where M_s is the mass of the ion labeled by s . The phonon frequency and eigenfunction are calculated by first-principles density functional perturbation theory (DFPT)⁷⁹⁾. We can calculate the electron-phonon matrix element by EPW package⁸⁰⁾ which uses the Wannier function as basis functions. By comparing the previous calculation for graphene by tight-binding method reported by Jiang,⁸¹⁾ we checked that EPW gives reasonable values of electron-phonon matrix element as a function of \mathbf{k} . In Fig. 2-1, we show the deformation potential defined by $D^{fiv}(\mathbf{k}, \mathbf{k}) = \sum_s \langle \psi^f(\mathbf{k}', \mathbf{r}) | \mathbf{u}_s \cdot \nabla_{\mathbf{R}_s} V(\mathbf{r} - \mathbf{R}_s) |_{\mathbf{R}_s = \mathbf{R}_{s0}} \psi^i(\mathbf{k}, \mathbf{r}) \rangle$ for π and π^* bands along $E_f - E_i = 1$ eV contour line calculated by EPW and tight-binding method.⁸¹⁾ Since the tight-binding calculation uses the fitting parameter, the value of $D^{fiv}(\mathbf{k}, \mathbf{k})$ does not match with EPW result. However the behavior of $D^{fiv}(\mathbf{k}, \mathbf{k})$ is consistent each other. Furthermore, final results of Raman spectra is given by arbitrary units. Thus in this thesis, we adopt the electron-phonon matrix element calculated from the EPW package.

2.5 Raman spectroscopy

When light is shed into a material, the light can be transmitted, absorbed, or scattered by the material. We can classify the scattering as elastic scattering (Rayleigh scattering) and inelastic scattering (Raman scattering). We focus on the Raman scattering in the following section.

2.5.1 Classical description of Raman scattering and Raman tensor

In this section, we explain the classical theory of Raman tensor which is powerful method to discuss the selection rule of Raman intensity as a function of the polarization direction of light. In the inelastic scattering, energy of the scattered light is different from the incident light. This difference of energy is explained by the modulation of the dielectric susceptibility by the lattice vibration in the classical theory.

The polarization $\mathbf{P}(\mathbf{r}, t)$ of a material for a given optical electric field \mathbf{E} is written by

$$\mathbf{P}(\mathbf{r}, t) = \epsilon_0 \chi \mathbf{E}(\mathbf{r}, t), \quad (2.73)$$

where χ is the dielectric susceptibility. Assuming the oscillated electric field with the wave number \mathbf{k}_i and the frequency ω_i , polarization is oscillated as following form;

$$\mathbf{P}(\mathbf{r}, t) = \epsilon_0 \chi \mathbf{E}(\mathbf{k}_i, \omega_i) \cos(\mathbf{k}_i \cdot \mathbf{r} - \omega_i t). \quad (2.74)$$

Furthermore, the dielectric susceptibility χ is modulated by the lattice vibration with the wave number \mathbf{q} and the frequency ω_q written as

$$\mathbf{u}(\mathbf{r}, t) = \mathbf{u}(\mathbf{q}, \omega_q) \cos(\mathbf{q} \cdot \mathbf{r} - \omega_q t). \quad (2.75)$$

By expanding χ by $\mathbf{u}(\mathbf{r}, t)$, we obtain

$$\chi(\mathbf{k}_i, \omega_i, \mathbf{u}) = \chi^{(0)}(\mathbf{k}_i, \omega_i) + \left(\frac{\partial \chi}{\partial \mathbf{u}} \right)_{\mathbf{u}=0} \mathbf{u} + \dots \quad (2.76)$$

Using Eqs. (2.74) and (2.76), the polarization modulated by the lattice vibration is

written as follows,

$$\mathbf{P}(\mathbf{r}, t, \mathbf{u}) = \mathbf{P}^{(0)}(\mathbf{r}, t) + \mathbf{P}^{(\text{ind})}(\mathbf{r}, t, \mathbf{u}), \quad (2.77)$$

$$\mathbf{P}^{(0)}(\mathbf{r}, t) = \chi^{(0)}(\mathbf{k}_i, \omega_i) \epsilon_0 \mathbf{E}(\mathbf{k}_i, \omega_i) \cos(\mathbf{k}_i \cdot \mathbf{r} - \omega_i t), \quad (2.78)$$

$$\mathbf{P}^{(\text{ind})}(\mathbf{r}, t, \mathbf{u}) = \left(\frac{\partial \chi}{\partial \mathbf{u}} \right)_{\mathbf{u}=0} \mathbf{u}(\mathbf{r}, t) \epsilon_0 \mathbf{E}(\mathbf{k}_i, \omega_i) \cos(\mathbf{k}_i \cdot \mathbf{r} - \omega_i t). \quad (2.79)$$

The first (second) term in Eq. (2.77) is the polarization without (with) the lattice vibration, which is given in Eq. (2.78) [(2.79)]. Raman scattering occurs by the second term in Eq. (2.77). Using Eqs. (2.75) and (2.79), we obtain

$$\begin{aligned} \mathbf{P}^{(\text{ind})}(\mathbf{r}, t, \mathbf{u}) &= \frac{1}{2} \epsilon_0 \left(\frac{\partial \chi}{\partial \mathbf{u}} \right)_{\mathbf{u}=0} \mathbf{u}(\mathbf{q}, \omega_q) \mathbf{E}(\mathbf{k}_i, \omega_i) \\ &\quad \times [\cos\{(\mathbf{k}_i + \mathbf{q}) \cdot \mathbf{r} - (\omega_i + \omega_q)t\} + \cos\{(\mathbf{k}_i - \mathbf{q}) \cdot \mathbf{r} - (\omega_i - \omega_q)t\}]. \end{aligned} \quad (2.80)$$

In the Eq. (2.80), the induced polarization by the lattice vibration consists of the scattering wave with the wave number $\mathbf{k}_s = \mathbf{k}_i + \mathbf{q}$ and the frequency $\omega_s = \omega_i + \omega_q$ (Stokes shifted light) and the one with $\mathbf{k}_s = \mathbf{k}_i - \mathbf{q}$ and $\omega_s = \omega_i - \omega_q$ (anti-Stokes shifted light).

When we use the polarized light for the Raman scattering, the electric field of the incident light is written by $\mathbf{E}(\mathbf{k}_i, \omega_i) = E(\mathbf{k}_i, \omega_i) \mathbf{P}_i$ with the polarization vector \mathbf{P}_i in Eq. (2.43) which describes the direction of the electric field and the scattered light is given by

$$\begin{aligned} \mathbf{P}^{(\text{ind})} &\propto \left(\frac{\partial \chi}{\partial \mathbf{P}} \right)_{\mathbf{u}=0} \mathbf{u}(\mathbf{q}, \omega_q) \cdot \mathbf{P}_i \\ &= \overleftrightarrow{R} \mathbf{P}_i, \end{aligned} \quad (2.81)$$

where $\overleftrightarrow{R} = \left(\frac{\partial \chi}{\partial \mathbf{u}} \right)_{\mathbf{u}=0} \mathbf{u}(\mathbf{q}, \omega_q)$ is the Raman tensor. Then the intensity of the scattered light which polarizes to the direction of \mathbf{P}_s is given by

$$I_s \propto |\mathbf{P}_s \cdot \mathbf{P}^{(\text{ind})}|^2 = \left| \mathbf{P}_s^* \overleftrightarrow{R} \mathbf{P}_i \right|^2. \quad (2.82)$$

The symmetry of the Raman tensor is determined only by the symmetry of the lattice vibration (phonon mode). We obtain the expression of Raman tensor from the character table. Here we derive the Raman tensor for D_{3h} symmetry which TMDs belong to. The character table of D_{3h} point group is given in Table C.2 in Appendix C. The phonon mode is Raman active when the normal mode belongs to the irreducible representation which has quadratic basis functions which change the polarization by the

vibration. Thus the A'_1 (first order representation, basis: $x^2 + y^2$ or z^2), E' (second order representation, basis: $x^2 - y^2$ and xy), and E'' (second order representation, basis: xz and yz) modes are Raman active in D_{3h} point group. Thus the Raman tensor for D_{3h} point group $\overleftrightarrow{R}(A'_1)$, $\overleftrightarrow{R}(E')$, and $\overleftrightarrow{R}(E'')$ are, respectively, written by using non-zero components e_{ii} as follows,

$$(x^2 + y^2, z^2) \overleftrightarrow{R}(A'_1) = \begin{pmatrix} e_{xx} + e_{yy} & 0 & 0 \\ 0 & e_{xx} + e_{yy} & 0 \\ 0 & 0 & e_{zz} \end{pmatrix}, \quad (2.83)$$

$$(\{x^2 - y^2, xy\}) \overleftrightarrow{R}(E') = \begin{pmatrix} e_{xx} - e_{yy} & 0 & 0 \\ 0 & -(e_{xx} - e_{yy}) & 0 \\ 0 & 0 & 0 \end{pmatrix}, \begin{pmatrix} 0 & e_{xy} & 0 \\ e_{yx} & 0 & 0 \\ 0 & 0 & 0 \end{pmatrix}, \quad (2.84)$$

$$(\{yz, zx\}) \overleftrightarrow{R}(E'') = \begin{pmatrix} 0 & 0 & e_{xz} \\ 0 & 0 & 0 \\ e_{zx} & 0 & 0 \end{pmatrix}, \begin{pmatrix} 0 & 0 & 0 \\ 0 & 0 & e_{yz} \\ 0 & e_{zy} & 0 \end{pmatrix}. \quad (2.85)$$

Using the definition, $a = e_{xx} - e_{yy}$, $c = e_{zz}$, $d = e_{xx} - e_{yy} = e_{xy} = e_{yz} = e_{zx}$ and assuming the symmetric shape of Raman tensor ($e_{xy} = e_{yx}$, $e_{yz} = e_{zy}$, and $e_{zx} = e_{xz}$), we can write the Raman tensor in Eqs. (2.83)-(2.85) as follows,

$$\overleftrightarrow{R}(A'_1) = \begin{pmatrix} a & 0 & 0 \\ 0 & a & 0 \\ 0 & 0 & c \end{pmatrix}, \quad (2.86)$$

$$\overleftrightarrow{R}(E') = \begin{pmatrix} d & 0 & 0 \\ 0 & -d & 0 \\ 0 & 0 & 0 \end{pmatrix}, \begin{pmatrix} 0 & d & 0 \\ d & 0 & 0 \\ 0 & 0 & 0 \end{pmatrix}, \quad (2.87)$$

$$\overleftrightarrow{R}(E'') = \begin{pmatrix} 0 & 0 & d \\ 0 & 0 & 0 \\ d & 0 & 0 \end{pmatrix}, \begin{pmatrix} 0 & 0 & 0 \\ 0 & 0 & d \\ 0 & d & 0 \end{pmatrix}. \quad (2.88)$$

In Table 2.1, we show the shape of Raman tensor⁷²⁾ for the corresponding phonon modes. We can know the selection rule of the polarization for the incident and the scattered light from the Raman tensor in Table 2.1 to calculate the Raman intensity by using Eq. (2.82).

Table 2.1: Raman-active vibrational symmetries and Raman tensors for the crystal symmetry classes⁷²⁾

Class	Raman tensors
Monoclinic	
2	$\begin{pmatrix} a & d \\ d & c \end{pmatrix} \begin{pmatrix} e & f \\ e & f \end{pmatrix}$
C ₂	A(y) B(x,z)
m	A'(x,z) A''(y)
2/m	A _g B _g
Orthorhombic	
	$\begin{pmatrix} a & & \\ & b & c \\ & c & \end{pmatrix} \begin{pmatrix} d \\ d \\ \end{pmatrix} \begin{pmatrix} e \\ e \\ \end{pmatrix} \begin{pmatrix} f \\ f \\ \end{pmatrix}$
222	A B ₁ (z) B ₂ (y) B ₃ (x)
mm2	A ₁ (z) A ₂ B ₁ (x) B ₂ (y)
mmm	A _g (z) B _{1g} B _{2g} B _{3g}
Trigonal	
	$\begin{pmatrix} a & & \\ & a & b \\ & b & \end{pmatrix} \begin{pmatrix} c & d & e \\ d & -c & f \\ e & f & \end{pmatrix} \begin{pmatrix} d & -c & -f \\ -c & -d & e \\ -f & e & \end{pmatrix}$
3	A(z) E(x) E(y)
$\bar{3}$	A _g E _g E _g
	$\begin{pmatrix} a & & \\ & b & b \\ & b & \end{pmatrix} \begin{pmatrix} c & d \\ -c & d \\ d & \end{pmatrix} \begin{pmatrix} -c & -d \\ -c & -d \\ -d & \end{pmatrix}$
32	A ₁ E(x) E(y)
3m	A ₁ (z) E(y) E(-x)
$\bar{3}m$	A _{1g} E _g E _g
Tetragonal	
	$\begin{pmatrix} a & & \\ & a & b \\ & b & \end{pmatrix} \begin{pmatrix} c & d \\ d & -c \\ -c & \end{pmatrix} \begin{pmatrix} e \\ e \\ f \end{pmatrix} \begin{pmatrix} -f \\ -f \\ e \end{pmatrix}$
4	A(z) B E(x) E(y)
$\bar{4}$	A B(z) E(x) E(-y)
4/m	A _g B _g E _g

	$\begin{pmatrix} a \\ a \\ b \end{pmatrix}$	$\begin{pmatrix} c \\ -c \end{pmatrix}$	$\begin{pmatrix} d \\ d \end{pmatrix}$	$\begin{pmatrix} e \\ e \end{pmatrix}$	$\begin{pmatrix} e \\ e \end{pmatrix}$
4mm	$A_1(z)$	B_1	B_2	$E(x)$	$E(y)$
422	A_1	B_1	B_2	$E(-y)$	$E(x)$
$\bar{4}2m$	A_1	B_1	$B_2(z)$	$E(y)$	$E(x)$
4/mmm	A_{1g}	B_{1g}	B_{2g}	E_g	E_g
Hexagonal					
6	$A(z)$	$\begin{pmatrix} c \\ c \\ d \\ d \end{pmatrix}$	$\begin{pmatrix} -d \\ -d \\ c \\ c \end{pmatrix}$	$\begin{pmatrix} e \\ e \\ f \\ f \end{pmatrix}$	$\begin{pmatrix} f \\ -e \\ -e \\ -f \end{pmatrix}$
$\bar{6}$	A'	$E_1(x)$	$E_1(y)$	E_2	E_2
$6/m$	A_g	E''	E''	$E'(x)$	$E'(y)$
		E_{1g}	E_{1g}	E_{2g}	E_{2g}
	$\begin{pmatrix} a \\ a \\ b \\ b \end{pmatrix}$	$\begin{pmatrix} c \\ c \\ c \\ c \end{pmatrix}$	$\begin{pmatrix} -c \\ -c \\ -c \\ -c \end{pmatrix}$	$\begin{pmatrix} d \\ d \\ d \\ d \end{pmatrix}$	$\begin{pmatrix} d \\ -d \\ -d \\ d \end{pmatrix}$
622	A_1	$E_1(x)$	$E_1(y)$	E_2	E_2
6mm	$A_1(z)$	$E_1(x)$	$E_1(-x)$	E_2	E_2
$\bar{6}m2$	A'_1	E''	E''	$E'(x)$	$E'(y)$
6/mmm	A_{1g}	E_{1g}	E_{1g}	E_{2g}	E_{2g}
Cubic					
	$\begin{pmatrix} a \\ a \\ a \end{pmatrix}$	$\begin{pmatrix} b \\ b \\ b \end{pmatrix}$	$\begin{pmatrix} b \\ b \\ b \end{pmatrix}$	$\begin{pmatrix} d \\ d \\ d \end{pmatrix}$	$\begin{pmatrix} d \\ d \\ d \end{pmatrix}$
23	A	E	E	$F(x)$	$F(z)$
m3	A_g	E_g	E_g	F_g	F_g
432	A_1	E	E	F_2	F_2
$\bar{4}3m$	A_1	E	E	$F_2(x)$	$F_2(z)$
m3m	A_{1g}	E_g	E_g	F_{2g}	F_{2g}

2.5.2 Quantum mechanical description of Raman scattering

In quantum mechanics, Raman scattering is the process that: (1) the electron in the ground state gets the energy of the incident photon and excited, (2) the excited electron interacts with the phonon and emit (absorb) a phonon, and (3) the electron recombines with the hole and emits the scattered photon. This process is described by the third-order perturbation theory given in Eq. (2.32) and the Raman intensity in Quantum mechanical formula is given by⁸²⁾

$$I_{\text{Raman}} = \sum_{\nu} \left| \sum_{\mathbf{k}} \sum_{i=f,m,m'} \frac{M_{\text{opt}}^{fm'}(\mathbf{k}) M_{\text{ep},\nu}^{m'm}(\mathbf{k}) M_{\text{opt}}^{mi}(\mathbf{k})}{(E_L - E^{mi}(\mathbf{k}) - i\gamma)(E_L - E^{m'i}(\mathbf{k}) - \hbar\omega_{\nu} - i\gamma)} \right|^2 \times \delta(E_{\text{RS}} - \hbar\omega_{\nu}), \quad (2.89)$$

where E_L , E_{RS} , $E^{m(m')i} = E_{m(m')} - E_i$, and $\hbar\omega_{\nu}$ are, respectively, the laser energy, Raman shift, the energy difference between i and $m(m')$ states, and the energy of emitted ν mode phonon. Since the electron-photon matrix element is written as $M_{\text{opt}}^{fi}(\mathbf{k}) \propto \mathbf{D}^{fi} \cdot \mathbf{P}$, the Raman intensity formula in Eq. (2.89) can be written as

$$I_{\text{Raman}} \propto \sum_{\nu} \left| \mathbf{P}_s^* \cdot \sum_{\mathbf{k}} \sum_{i=f,m,m'} \frac{\mathbf{D}^{fm'}(\mathbf{k}) \cdot M_{\text{ep},\nu}^{m'm}(\mathbf{k}) \cdot \mathbf{D}^{mi}(\mathbf{k})^*}{(E_L - E^{mi}(\mathbf{k}) - i\gamma)(E_L - E^{m'i}(\mathbf{k}) - \hbar\omega_{\nu} - i\gamma)} \cdot \mathbf{P}_i \right|^2 \times \delta(E_{\text{RS}} - \hbar\omega_{\nu}). \quad (2.90)$$

Then, the relation of Raman tensor with the quantum mechanical formula of Raman intensity is given by

$$\overleftrightarrow{R}(\nu) = \sum_{\mathbf{k}} \sum_{i=f,m,m'} \frac{\mathbf{D}^{fm'}(\mathbf{k}) \cdot M_{\text{ep},\nu}^{m'm}(\mathbf{k}) \cdot \mathbf{D}^{mi}(\mathbf{k})^*}{(E_L - E^{mi}(\mathbf{k}) - i\gamma)(E_L - E^{m'i}(\mathbf{k}) - \hbar\omega_{\nu} - i\gamma)}. \quad (2.91)$$

Chapter 3

Valley polarization in transition metal dichalcogenides

In this chapter, we present the laser energy dependence of optical valley polarization for TMDs. Valley-selective optical transition occurs by using the circularly polarized light. Right-handed circularly polarized (RCP, σ_-) [or left-handed circularly polarized (LCP, σ_+)] light selectively excites the electrons in the K (or K') valley. Such a valley polarized optical transition can be observed only in odd number of the TMD layers since even number of TMD layers or bulk TMDs have an inversion symmetry in their structure, which gives the condition for the optical matrix element $M_{\text{opt}}^{\text{cv}}(\mathbf{k}) = M_{\text{opt}}^{\text{cv}}(-\mathbf{k})$ that requests the same optical transition in the K and K' valleys for given RCP or LCP light.^{55,83)} The valley-selective optical transition is discussed analytically by calculating dipole vector $\mathbf{D}^{fi}(\mathbf{k})$. In Sec. 3.1, we present the analytical form of dipole vector in the K and K' valley for TMDs within the tight-binding calculation and compare with the graphene presented by Grüneis, *et al.*⁷⁸⁾ In Sec. 3.2, we show the laser energy dependence of the valley polarization for six monolayer TMD materials: MoS₂, MoSe₂, MoTe₂, WS₂, WSe₂, and WTe₂, calculated by using first-principles calculations. We discuss the optimum condition of the valley polarization to excite many valley-polarized electrons.

3.1 Dipole vector of hexagonal lattice

In this section, we derive the dipole vector around the K and K' points in hexagonal lattice within simple tight-binding method. We assume that two atoms in the unit cell are different from each other and consider the dipole transition between the p and d orbitals. In tight-binding method, wave function is given by a linear combination of

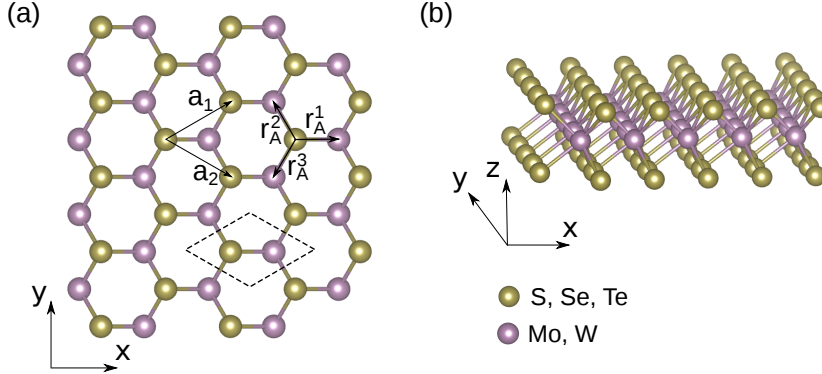


Figure 3-1: (a) Top and (b) side views of the crystal structure of TMDs. In Fig. (a), we show the unitcell of TMDs (dashed line), lattice vectors (\mathbf{a}_1 , \mathbf{a}_2), and the vectors pointing to the three nearest B (transition metal) atoms from an A (chalcogen) atom (\mathbf{r}_A^1 , \mathbf{r}_A^2 , \mathbf{r}_A^3) in two dimensional atomic layer plane

Bloch orbitals as follows,

$$\Psi^i(\mathbf{k}, \mathbf{r}) = \frac{1}{\sqrt{N_u}} \sum_{m=A,B} C_m^i(\mathbf{k}) \sum_{j=1}^{N_u} e^{i\mathbf{k} \cdot \mathbf{R}_j} \varphi_m^i(\mathbf{r} - \mathbf{R}_j) \quad (i = v, c) \quad (3.1)$$

where \mathbf{R}_j , $\varphi_m^i(\mathbf{r})$, $C_m^i(\mathbf{k})$ and N_u are, respectively, the j -th lattice vector, the m -th atomic orbital, the coefficient of the Bloch function, and the number of unit cells in the crystal. Label i denotes either valence (v) or conduction (c) band. We consider one orbital for each atom that has a different on-site energy $\varepsilon_m = \langle \varphi_m^i | H | \varphi_m^i \rangle$ for A and B atoms (A: S, Se, Te and B: Mo, W, $\varepsilon_A > \varepsilon_B$).

According to the first principles calculations,^{56,84,85)} φ_A^c is represented by the wave function of the $\frac{1}{\sqrt{2}}(\tilde{p}_x \pm i\tilde{p}_y)$ orbital of chalcogen atom and φ_B^v is represented by the $\frac{1}{\sqrt{2}}(d_{xy} \pm id_{x^2-y^2})$ orbital of transition metal atom, i.e. $\langle \varphi_A^c(\mathbf{r} - \mathbf{r}_B^\ell) | \nabla | \varphi_B^v(\mathbf{r}) \rangle = \frac{1}{2} \langle \tilde{p}_x \pm i\tilde{p}_y(\mathbf{r} - \mathbf{r}_B^\ell) | \nabla | d_{xy} \pm id_{x^2-y^2}(\mathbf{r}) \rangle$. Plus (minus) sign corresponds to the K (K') point. It is noted that for S, Se, and Te of TMDs, we have two atoms in the unit cell. The coefficients C_A^i for p_x and p_y orbitals of the chalcogen atoms have the same value with the same sign for both the highest valence and lowest conduction band near the K or K' point.^{84,85)} Thus we simply consider a linear combination of two orbitals of S, Se, Te atoms as a single hybridized orbital and we can virtually put the orbitals without

losing the symmetry of p orbitals on the x - y plane of Mo or W atoms as follows,

$$|\tilde{p}_x\rangle = \frac{1}{\sqrt{2}}(|p_x^1\rangle + |p_x^2\rangle), \quad (3.2)$$

$$|\tilde{p}_y\rangle = \frac{1}{\sqrt{2}}(|p_y^1\rangle + |p_y^2\rangle), \quad (3.3)$$

where $|p_x^1\rangle$, $|p_x^2\rangle$, $|p_y^1\rangle$, and $|p_y^2\rangle$ are the p_x and p_y orbitals for the two chalcogen atoms in the unit cell. Thus, the matrix can be selected in a 2×2 matrix in which a d orbital of B atom and a \tilde{p}_x orbital are selected to A atom as a basis set. We take into account only the nearest neighbor transfer integral and dipole transition for the simplicity and the Hamiltonian matrix \mathcal{H} and the overlap matrix \mathcal{S} are written by

$$\mathcal{H} = \begin{pmatrix} \varepsilon_A & tf(\mathbf{k}) \\ tf(\mathbf{k})^* & \varepsilon_B \end{pmatrix}, \quad (3.4)$$

$$\mathcal{S} = \begin{pmatrix} 1 & sf(\mathbf{k}) \\ sf(\mathbf{k})^* & 1 \end{pmatrix}, \quad (3.5)$$

where $t = \langle \varphi_B^i(\mathbf{r} - \mathbf{r}_A^\ell) | H | \varphi_A^i(\mathbf{r}) \rangle$ and $s = \langle \varphi_B^i(\mathbf{r} - \mathbf{r}_A^\ell) | \varphi_A^i(\mathbf{r}) \rangle$ are the transfer integral and the overlap integral from A to B atom, respectively. The phase factor $f(\mathbf{k})$ is given by

$$f(\mathbf{k}) = e^{ik_x a/\sqrt{3}} + 2e^{-ik_x a/2\sqrt{3}} \cos\left(\frac{k_y a}{2}\right), \quad (3.6)$$

where a is a lattice constant. Solving the secular equation $\det|\mathcal{H} - E\mathcal{S}| = 0$, we can obtain the eigen energy and eigen function by assuming the overlap matrix is the unit matrix as follows,

$$E^i(\mathbf{k}) = \pm \frac{1}{2} \sqrt{\varepsilon_g^2 - 4t^2|f(\mathbf{k})|^2}, \quad (3.7)$$

$$\begin{pmatrix} C_A^i(\mathbf{k}) \\ C_B^i(\mathbf{k}) \end{pmatrix} = \frac{e^{i\delta_i}}{\sqrt{w^i(\mathbf{k})}} \begin{pmatrix} tf(\mathbf{k}) \\ -\frac{1}{2}\varepsilon_g + E^i(\mathbf{k}) \end{pmatrix}, \quad (3.8)$$

where normalization factor $w^i(\mathbf{k})$ is given by

$$w^i(\mathbf{k}) = t^2|f(\mathbf{k})|^2 + \left(-\frac{1}{2}\varepsilon_g + E^i(\mathbf{k})\right)^2, \quad (3.9)$$

and, $\varepsilon_g = \varepsilon_A - \varepsilon_B$ and δ_i are, respectively, the energy gap and the arbitrary phase factor of the eigen function, respectively. Here we adopt the difference of the phase

factor of the wave function between valence and conduction band $\delta_v - \delta_c = \pi$ in the following calculation. We set the origin of energy at the averaged value of ε_A and ε_B , i.e. $\varepsilon_A + \varepsilon_B = 0$. Using Eqs. (2.40) and (3.1), dipole vector $\mathbf{D}^{\text{cv}}(\mathbf{k})$ is written by

$$\begin{aligned} \mathbf{D}^{\text{cv}}(\mathbf{k}) &= \langle \Psi^{\text{c}}(\mathbf{k}, \mathbf{r}) | \nabla | \Psi^{\text{v}}(\mathbf{k}, \mathbf{r}) \rangle \\ &= \sum_{\ell=1}^3 C_B^{\text{c}*}(\mathbf{k}) C_A^{\text{v}}(\mathbf{k}) \exp(-i\mathbf{k} \cdot \mathbf{r}_A^\ell) \langle \varphi_B^{\text{c}}(\mathbf{r} - \mathbf{r}_A^\ell) | \nabla | \varphi_A^{\text{v}}(\mathbf{r}) \rangle \\ &\quad + \sum_{\ell=1}^3 C_A^{\text{c}*}(\mathbf{k}) C_B^{\text{v}}(\mathbf{k}) \exp(-i\mathbf{k} \cdot \mathbf{r}_B^\ell) \langle \varphi_A^{\text{c}}(\mathbf{r} - \mathbf{r}_B^\ell) | \nabla | \varphi_B^{\text{v}}(\mathbf{r}) \rangle, \end{aligned} \quad (3.10)$$

where $\mathbf{r}_A^1 = (a/\sqrt{3}, 0, 0)$, $\mathbf{r}_A^2 = (-a/2\sqrt{3}, a/2, 0)$, $\mathbf{r}_A^3 = (-a/2\sqrt{3}, -a/2, 0)$ are the vectors pointing to the three nearest B atoms from an A atom in two dimensional atomic layer plane [see Fig. 3-1 (a)]. The vector \mathbf{r}_B^ℓ has a relation with \mathbf{r}_A^ℓ as $\mathbf{r}_B^\ell = -\mathbf{r}_A^\ell$. The dipole transition within the same orbital of the same atom is forbidden [$\langle \varphi_m^i(\mathbf{r}) | \nabla | \varphi_m^i(\mathbf{r}) \rangle = 0$] because of being odd function of the products. $f(\mathbf{k})$ and $E^i(\mathbf{k})$ in Eqs. (3.6) and (3.8) are expanded by \mathbf{k} around the K [$\mathbf{K} = (0, -4\pi/3a, 0)$] and K' [$\mathbf{K}' = (0, 4\pi/3a, 0)$] points as follows,

$$f(\mathbf{K} + \mathbf{k}) \sim \frac{\sqrt{3}a}{2}(ik_x + k_y), \quad (3.11)$$

$$f(\mathbf{K}' + \mathbf{k}') \sim \frac{\sqrt{3}a}{2}(ik'_x - k'_y), \quad (3.12)$$

$$E^i(\mathbf{K} + \mathbf{k}) \simeq E^i(\mathbf{K}' + \mathbf{k}') \sim \pm \frac{1}{2}\varepsilon_g. \quad (3.13)$$

where k_x (k'_x) and k_y (k'_y) are the wave number measured from the K (K') point, and plus (minus) sign corresponds to the conduction (valence) band. Using Eqs. (3.11)-(3.13), the products of the coefficients in Eq. (3.10) are expanded, too, up to the first order of k , which are given by

$$\begin{aligned} C_B^{\text{c}*}(\mathbf{K} + \mathbf{k}) C_A^{\text{v}}(\mathbf{K} + \mathbf{k}) &\simeq C_B^{\text{c}*}(\mathbf{K}' + \mathbf{k}') C_A^{\text{v}}(\mathbf{K}' + \mathbf{k}') \\ &\sim 0, \end{aligned} \quad (3.14)$$

$$C_A^{\text{c}*}(\mathbf{K} + \mathbf{k}) C_B^{\text{v}}(\mathbf{K} + \mathbf{k}) \sim \frac{-ik_x + k_y}{k}, \quad (3.15)$$

$$C_A^{\text{c}*}(\mathbf{K}' + \mathbf{k}') C_B^{\text{v}}(\mathbf{K}' + \mathbf{k}') \sim \frac{-ik'_x - k'_y}{k'}, \quad (3.16)$$

where $k = \sqrt{k_x^2 + k_y^2}$ ($k' = \sqrt{k'^2_x + k'^2_y}$) is the distance from the K (K') point. The matrix element $\langle \varphi_A^{\text{c}}(\mathbf{r} - \mathbf{r}_B^\ell) | \nabla | \varphi_B^{\text{v}}(\mathbf{r}) \rangle$ is obtained by the Slater-Koster method⁸⁶⁾ of p

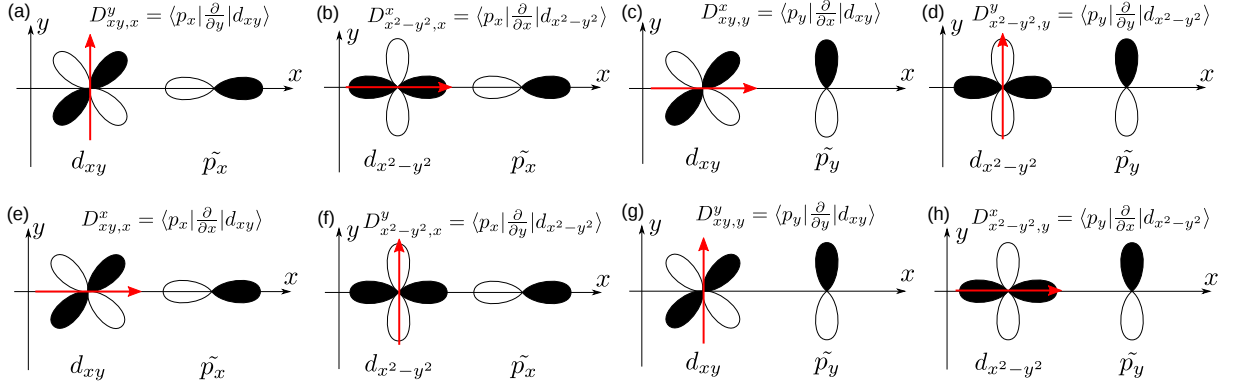


Figure 3-2: (a)-(d) Non-vanishing and (e)-(h) vanishing dipole parameters between \tilde{p}_x or \tilde{p}_y and d_{xy} or $d_{x^2-y^2}$ orbitals. Red arrow indicates the direction of differential operator.

and d orbitals in the tight-binding calculation which decomposes the atomic orbitals to π and σ direction (see Fig. 3-2) as is discussed below. When we rotate the coordinate axis around the z axis by an angle θ , p_x , p_y , d_{xy} , and $d_{x^2-y^2}$ orbitals are written by using the orbitals $p_{x'}$, $p_{y'}$, $d_{x'y'}$, and $d_{x'^2-y'^2}$ which is the expression of orbitals in the rotated axis as follows,

$$p_x = p_{x'} \cos \theta - p_{y'} \sin \theta, \quad (3.17)$$

$$p_y = p_{x'} \sin \theta + p_{y'} \cos \theta, \quad (3.18)$$

$$d_{x^2-y^2} = d_{x'^2-y'^2} \cos 2\theta - d_{x'y'} \sin 2\theta, \quad (3.19)$$

$$d_{xy} = d_{x'^2-y'^2} \sin 2\theta + d_{x'y'} \cos 2\theta. \quad (3.20)$$

In the same way, the components of ∇ are also written by

$$\frac{\partial}{\partial x} = \cos \theta \frac{\partial}{\partial x'} - \sin \theta \frac{\partial}{\partial y'}, \quad (3.21)$$

$$\frac{\partial}{\partial y} = \sin \theta \frac{\partial}{\partial x'} + \cos \theta \frac{\partial}{\partial y'}, \quad (3.22)$$

$$\frac{\partial}{\partial z} = \frac{\partial}{\partial z'}. \quad (3.23)$$

Using Eq. (3.14)-(3.23), we can decompose the dipole vector described by non-vanishing four parameters as is shown in Figs. 3-2 (a)-(d). We note that dipole parameters for z direction and four parameters shown in Figs. 3-2 (e)-(h) vanish because of the symmetry of the orbitals. Using the four dipole parameters ($D^x_{xy,y}$, $D^y_{xy,x}$, $D^y_{x^2-y^2,y}$, $D^x_{x^2-y^2,x}$), we obtain the matrix elements between d_{xy} and the three nearest \tilde{p}_x orbitals

Fig. 3-2: fig/ch3-dipole-parameter.eps

(atomic dipole vectors) as follows,

$$\langle \tilde{p}_x(\mathbf{r} - \mathbf{r}_B^1) | \nabla | d_{xy}(\mathbf{r}) \rangle = \begin{pmatrix} 0 \\ D_{xy,x}^y \\ 0 \end{pmatrix}, \quad (3.24)$$

$$\langle \tilde{p}_x(\mathbf{r} - \mathbf{r}_B^2) | \nabla | d_{xy}(\mathbf{r}) \rangle = \begin{pmatrix} \frac{\sqrt{3}}{8}(D_{xy,y}^x + D_{xy,x}^y + 3D_{x^2-y^2,y}^y + D_{x^2-y^2,x}^x) \\ \frac{1}{8}(3D_{xy,y}^x - D_{xy,x}^y - 3D_{x^2-y^2,y}^y + 3D_{x^2-y^2,x}^x) \\ 0 \end{pmatrix} \quad (3.25)$$

$$\langle \tilde{p}_x(\mathbf{r} - \mathbf{r}_B^3) | \nabla | d_{xy}(\mathbf{r}) \rangle = \begin{pmatrix} \frac{\sqrt{3}}{8}(-D_{xy,y}^x - D_{xy,x}^y - 3D_{x^2-y^2,y}^y - D_{x^2-y^2,x}^x) \\ \frac{1}{8}(3D_{xy,y}^x - D_{xy,x}^y - 3D_{x^2-y^2,y}^y + 3D_{x^2-y^2,x}^x) \\ 0 \end{pmatrix} \quad (3.26)$$

Similarly, other atomic dipole vectors are given by

$$\langle \tilde{p}_y(\mathbf{r} - \mathbf{r}_B^1) | \nabla | d_{xy}(\mathbf{r}) \rangle = \begin{pmatrix} D_{xy,y}^x \\ 0 \\ 0 \end{pmatrix}, \quad (3.27)$$

$$\langle \tilde{p}_y(\mathbf{r} - \mathbf{r}_B^2) | \nabla | d_{xy}(\mathbf{r}) \rangle = \begin{pmatrix} \frac{1}{8}(-D_{xy,y}^x + 3D_{xy,x}^y - 3D_{x^2-y^2,y}^y + 3D_{x^2-y^2,x}^x) \\ \frac{\sqrt{3}}{8}(-D_{xy,y}^x - D_{xy,x}^y + D_{x^2-y^2,y}^y + 3D_{x^2-y^2,x}^x) \\ 0 \end{pmatrix} \quad (3.28)$$

$$\langle \tilde{p}_y(\mathbf{r} - \mathbf{r}_B^3) | \nabla | d_{xy}(\mathbf{r}) \rangle = \begin{pmatrix} \frac{1}{8}(-D_{xy,y}^x + 3D_{xy,x}^y - 3D_{x^2-y^2,y}^y + 3D_{x^2-y^2,x}^x) \\ \frac{\sqrt{3}}{8}(D_{xy,y}^x + D_{xy,x}^y - D_{x^2-y^2,y}^y - 3D_{x^2-y^2,x}^x) \\ 0 \end{pmatrix} \quad (3.29)$$

$$\langle \tilde{p}_x(\mathbf{r} - \mathbf{r}_B^1) | \nabla | d_{x^2-y^2}(\mathbf{r}) \rangle = \begin{pmatrix} D_{x^2-y^2,x}^x \\ 0 \\ 0 \end{pmatrix}, \quad (3.30)$$

$$\langle \tilde{p}_x(\mathbf{r} - \mathbf{r}_B^2) | \nabla | d_{x^2-y^2}(\mathbf{r}) \rangle = \begin{pmatrix} \frac{1}{8}(3D_{xy,y}^x + 3D_{xy,x}^y - 3D_{x^2-y^2,y}^y - D_{x^2-y^2,x}^x) \\ \frac{\sqrt{3}}{8}(3D_{xy,y}^x - D_{xy,x}^y + D_{x^2-y^2,y}^y - D_{x^2-y^2,x}^x) \\ 0 \end{pmatrix} \quad (3.31)$$

$$\langle \tilde{p}_x(\mathbf{r} - \mathbf{r}_B^3) | \nabla | d_{x^2-y^2}(\mathbf{r}) \rangle = \begin{pmatrix} \frac{1}{8}(3D_{xy,y}^x + 3D_{xy,x}^y - 3D_{x^2-y^2,y}^y - D_{x^2-y^2,x}^x) \\ \frac{\sqrt{3}}{8}(-3D_{xy,y}^x + D_{xy,x}^y - D_{x^2-y^2,y}^y + D_{x^2-y^2,x}^x) \\ 0 \end{pmatrix} \quad (3.32)$$

$$\langle \tilde{p}_y(\mathbf{r} - \mathbf{r}_B^1) | \nabla | d_{x^2-y^2}(\mathbf{r}) \rangle = \begin{pmatrix} 0 \\ D_{x^2-y^2,y}^y \\ 0 \end{pmatrix}, \quad (3.33)$$

$$\langle \tilde{p}_y(\mathbf{r} - \mathbf{r}_B^2) | \nabla | d_{x^2-y^2}(\mathbf{r}) \rangle = \begin{pmatrix} \frac{\sqrt{3}}{8}(-D_{xy,y}^x + 3D_{xy,x}^y + D_{x^2-y^2,y}^y - D_{x^2-y^2,x}^x) \\ \frac{1}{8}(-3D_{xy,y}^x - 3D_{xy,x}^y - D_{x^2-y^2,y}^y - 3D_{x^2-y^2,x}^x) \\ 0 \end{pmatrix} \quad (3.34)$$

$$\langle \tilde{p}_y(\mathbf{r} - \mathbf{r}_B^3) | \nabla | d_{x^2-y^2}(\mathbf{r}) \rangle = \begin{pmatrix} \frac{\sqrt{3}}{8}(D_{xy,y}^x - 3D_{xy,x}^y - D_{x^2-y^2,y}^y - D_{x^2-y^2,x}^x) \\ \frac{1}{8}(-3D_{xy,y}^x - 3D_{xy,x}^y - D_{x^2-y^2,y}^y - 3D_{x^2-y^2,x}^x) \\ 0 \end{pmatrix} \quad (3.35)$$

Using Eqs. (3.33)-(3.35), the summation of the three components of atomic dipole vectors with the phase factors between d_{xy} orbital of transition metal atom and the nearest p_x orbital of chalcogen atom is given in the lowest order as follows,

$$\begin{aligned} & \sum_{\ell=1}^3 \exp(-i\mathbf{k} \cdot \mathbf{r}_B^\ell) \langle \tilde{p}_x(\mathbf{r} - \mathbf{r}_B^\ell) | \nabla | d_{xy}(\mathbf{r}) \rangle \\ &= \frac{3}{8} \begin{pmatrix} \pm i(D_{xy,y}^x + D_{xy,x}^y + 3D_{x^2-y^2,y}^y + D_{x^2-y^2,x}^x) \\ -D_{xy,y}^x + 3D_{xy,x}^y + D_{x^2-y^2,y}^y - D_{x^2-y^2,x}^x \\ 0 \end{pmatrix}. \end{aligned} \quad (3.36)$$

In a similar way, we obtain the other terms in Eq. (3.10) as follows,

$$\begin{aligned} & \sum_{\ell=1}^3 \exp(-i\mathbf{k} \cdot \mathbf{r}_B^\ell) \langle \tilde{p}_y(\mathbf{r} - \mathbf{r}_B^\ell) | \nabla | d_{xy}(\mathbf{r}) \rangle \\ &= \frac{3}{8} \begin{pmatrix} 3D_{xy,y}^x - D_{xy,x}^y + D_{x^2-y^2,y}^y - D_{x^2-y^2,x}^x \\ \pm i(-D_{xy,y}^x - D_{xy,x}^y + D_{x^2-y^2,y}^y + 3D_{x^2-y^2,x}^x) \\ 0 \end{pmatrix}, \end{aligned} \quad (3.37)$$

$$\begin{aligned}
& \sum_{\ell=1}^3 \exp(-i\mathbf{k} \cdot \mathbf{r}_B^\ell) \langle \tilde{p}_x(\mathbf{r} - \mathbf{r}_B^\ell) | \nabla | d_{x^2-y^2}(\mathbf{r}) \rangle \\
&= \frac{3}{8} \begin{pmatrix} -D_{xy,y}^x - D_{xy,x}^y + D_{x^2-y^2,y}^y + 3D_{x^2-y^2,x}^x \\ \pm i(3D_{xy,y}^x - D_{xy,x}^y + D_{x^2-y^2,y}^y - D_{x^2-y^2,x}^x) \\ 0 \end{pmatrix}, \tag{3.38}
\end{aligned}$$

$$\begin{aligned}
& \sum_{\ell=1}^3 \exp(-i\mathbf{k} \cdot \mathbf{r}_B^\ell) \langle \tilde{p}_y(\mathbf{r} - \mathbf{r}_B^\ell) | \nabla | d_{x^2-y^2}(\mathbf{r}) \rangle \\
&= \frac{3}{8} \begin{pmatrix} \pm i(-D_{xy,y}^x + 3D_{xy,x}^y + D_{x^2-y^2,y}^y - D_{x^2-y^2,x}^x) \\ D_{xy,y}^x + D_{xy,x}^y + 3D_{x^2-y^2,y}^y + D_{x^2-y^2,x}^x \\ 0 \end{pmatrix}. \tag{3.39}
\end{aligned}$$

Plus (minus) sign in Eqs. (3.36)-(3.39) corresponds to around the K (K') point. Using Eqs. (3.10), (3.14)-(3.16), and (3.36)-(3.39), dipole vector of TMDS around the K (K') point is finally given by

$$\begin{aligned}
\mathbf{D}^{\text{cv}}(\mathbf{K} + \mathbf{k}) &= (D_{xy,y}^x - D_{xy,x}^y - D_{x^2-y^2,y}^y - D_{x^2-y^2,x}^x) \\
&\quad \times \frac{3}{4} \cdot \frac{k_x + ik_y}{k} \begin{pmatrix} 1 \\ -i \\ 0 \end{pmatrix}, \tag{3.40}
\end{aligned}$$

$$\begin{aligned}
\mathbf{D}^{\text{cv}}(\mathbf{K}' + \mathbf{k}') &= (D_{xy,y}^x - D_{xy,x}^y - D_{x^2-y^2,y}^y - D_{x^2-y^2,x}^x) \\
&\quad \times \frac{3}{4} \cdot \frac{k'_x - ik'_y}{k'} \begin{pmatrix} 1 \\ i \\ 0 \end{pmatrix}. \tag{3.41}
\end{aligned}$$

The form of $\mathbf{D}^{\text{cv}}(\mathbf{K} + \mathbf{k}) \propto (1, -i, 0)$ [$\mathbf{D}^{\text{cv}}(\mathbf{K}' + \mathbf{k}') \propto (1, i, 0)$] couples only with RCP (σ_-) [LCP (σ_+)] light and valley polarization occurs near the K (K') point. We note that the expression of the dipole vector $\mathbf{D}^{\text{cv}}(\mathbf{k})$ depends on the complex value of the phase of the Bloch wave function $C_m^i(\mathbf{k})$ in Eq. (3.8). However, the relative angle of real and imaginary part for $\mathbf{D}^{\text{cv}}(\mathbf{k})$ does not depend on the phase of the Bloch functions and always give $-\frac{\pi}{2}$ or $\frac{\pi}{2}$ for the K and K' point, respectively.

In Figs 3-3 (a) and (b), we show the real and imaginary part of the dipole vectors of TMDS near the K and K' points expressed in Eqs. (3.40) and (3.41). The angle between the real and imaginary part of $\mathbf{D}^{\text{cv}}(\mathbf{k})$ is always $\frac{\pi}{2}$ ($-\frac{\pi}{2}$) around the K (K') point that is written by $\mathbf{D}^{\text{cv}}(\mathbf{k}) \propto (1, -i, 0)$ [$\mathbf{D}^{\text{cv}}(\mathbf{k}) \propto (1, i, 0)$]. When we take an inner product $\mathbf{D}^{\text{cv}}(\mathbf{k}) \cdot \mathbf{p}_{\sigma\pm}$, the value is zero or finite value depending on (1) the K or

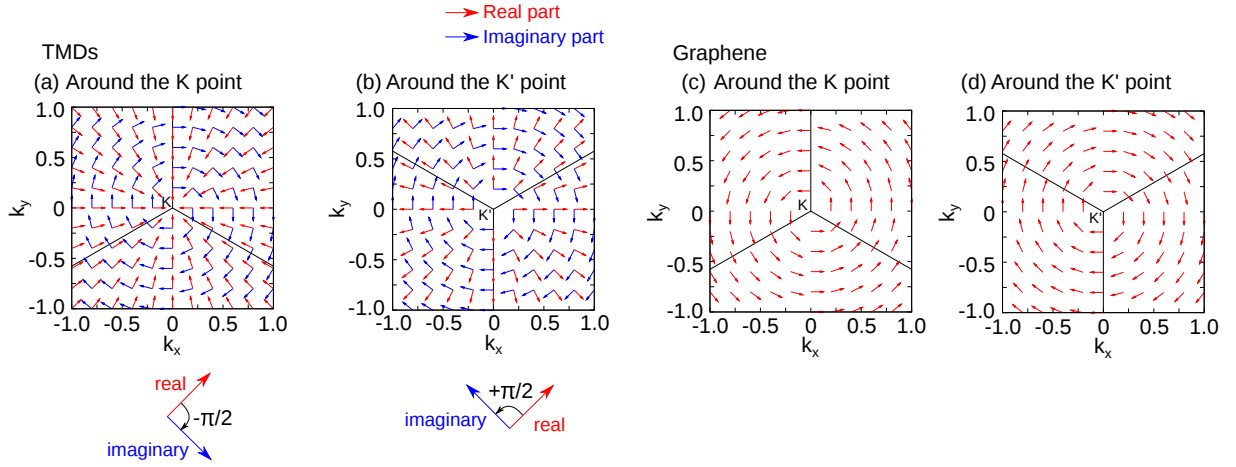


Figure 3-3: The dipole vectors of (a)-(b) TMDs and (c)-(d) graphene⁷⁾ around the K and K' points calculated by analytical tight-binding method.

K' valley, or (2) LCP (σ_+) or RCP (σ_-) light, respectively, which is the origin of the valley polarization. By using the description of the dipole vector in Eqs. (3.40) and (3.41), the matrix element of the electron-photon interaction is given by

$$M_{\text{opt}}^{\text{cv}}(\mathbf{k}) \propto \mathbf{D}^{\text{cv}}(\mathbf{k}) \cdot \mathbf{P}_{\sigma_+} \propto \begin{cases} 0 & (\text{K}) \\ \frac{-k'_x + ik'_y}{k'} & (\text{K}') \end{cases}, \quad (3.42)$$

for LCP light, and

$$M_{\text{opt}}^{\text{cv}}(\mathbf{k}) \propto \mathbf{D}^{\text{cv}}(\mathbf{k}) \cdot \mathbf{P}_{\sigma_-} \propto \begin{cases} \frac{k_x + ik_y}{k} & (\text{K}) \\ 0 & (\text{K}') \end{cases}, \quad (3.43)$$

for RCP light.

Thus the right-hand sides of Eqs. (3.42) and (3.43) become a finite value at $k_x = k_y = 0$ ($k'_x = k'_y = 0$). The relation between the real and imaginary part of $\mathbf{D}^{\text{cv}}(\mathbf{k})$ which gives valley polarization is unique for the hexagonal lattice system with different A and B atoms in the unit cell. In the case of graphene, on the other hand, $\mathbf{D}^{\text{cv}}(\mathbf{k})$ can be expressed only by a real part as shown in Figs. 3-3 (c) and (d) since A and B atoms are the same carbon atom in the tight-binding calculation.⁸⁷⁾ We also show the dipole vector of graphene at the K and K' valley that was given by Grüneis *et al.*⁷⁸⁾ In the case of graphene, dipole vector can be expressed only by the real part. Then the electron-photon matrix element $M_{\text{opt}} \propto \mathbf{D}^{\text{cv}} \cdot \mathbf{P}_{\sigma_{\pm}}$ is same at the K and K' valley, which is the consequence of the existence of the inversion symmetry in graphene. Thus, we can

say that the materials of hexagonal lattice structure with different atoms (monolayer TMDs, or hexagonal boron nitride) have non-equivalent optical transition near the K and K' point for RCP and LCP light, though graphene, silicene, and germanene which are composed by one type of atom do not have such a valley-selective optical transition. This result is in good agreement with that the valley-selective optical transition occurs only for the materials which do not have inversion symmetry.^{9,55,83)}

3.2 Laser energy dependence of valley polarization in TMDs

In this section, we discuss about the laser energy E_L dependence of valley polarization calculated by first-principles method.

3.2.1 Electronic structure of TMDs

In Fig. 3-4 (a)-(f), we show the electronic energy bands of the six TMD materials calculated by the DFT calculation with spin-orbit interaction. The direct energy gaps at the K (K') point of the six TMDs are 0.71 eV (WTe₂) to 1.65 eV (MoS₂) in this calculation. The conduction bands at the K (K') point are almost degenerate for spin-up and down states. On the other hand, the valence band splits by spin-orbit interaction at the K (K') point about from 0.15 eV (MoS₂) to 0.50 eV (WTe₂) as shown in red (spin-up) or blue (spin-down) lines in Figs. 3-4 (a)-(f). Spin-up and down states are almost degenerate near the Γ point because the spin-orbit interaction $\boldsymbol{\ell} \cdot \boldsymbol{s}$ becomes zero ($\ell = 0$ at the Γ point). On the other hand, the energy bands at the K (K') point are well separated for spin-up and down states, and the spin-up (down) state for the valence band is higher than the spin-down (up) state at the K (K') point. This relation satisfies the condition of the time reversal symmetry [$E(\mathbf{k}, \uparrow) = E(-\mathbf{k}, \downarrow)$] of the spin-orbit interaction.

It is noted that the spin-split two energy bands show the same dipole selection rule of the optical transition within the same valley since the selection rule is determined by the azimuthal (ℓ) and magnetic (m) quantum numbers. Spin quantum number is conserved in the electric-dipole transition for the spin-split energy bands (from spin-up to up and from down to down state). Thus the valley-selective excitation near the K (K') point is also the spin-selective excitation because of the large spin-splitting of the electronic energy bands when we match the laser energy to the energy gap. This fact makes it possible to detect the valley polarized electron by the direction of spin.

3.2. LASER ENERGY DEPENDENCE OF VALLEY POLARIZATION IN TMDS55

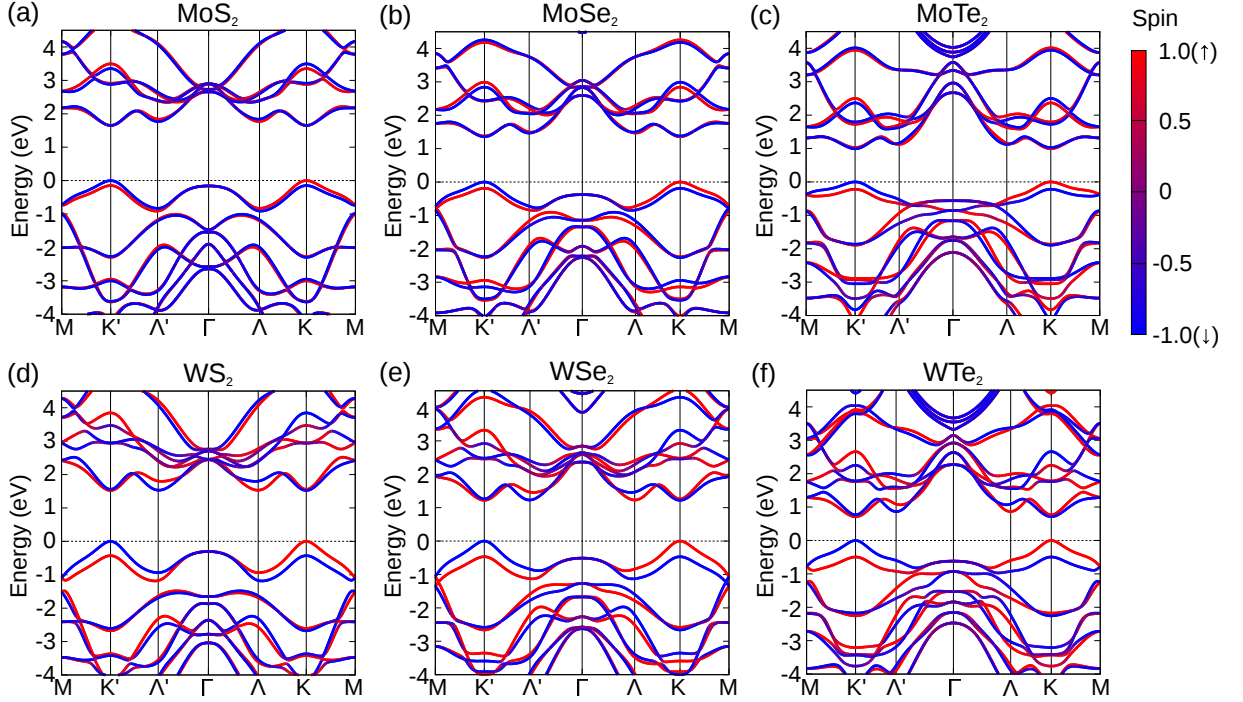


Figure 3-4: (a)-(f) Electronic energy bands of six TMD materials [(a) MoS₂ (b) MoSe₂ (c) MoTe₂ (d) WS₂ (e) WSe₂ (f) WTe₂] along to MK'ΓKM line calculated by DFT method with spin-orbit interaction. Red (blue) color indicates spin up (down) state. The top of valence band is set as zero energy.

3.2.2 Absorption spectra of TMDs

In Figs. 3-5 (b)-(g), we plot the absorption spectra $\alpha(E_L)$ for the six TMD materials. We note that the absorption spectra shown in Figs. 3-5 (b)-(g) are calculated based on the density functional theory (DFT) for the ground state and generally DFT calculation underestimates the energy gap of semiconductors. Beyond DFT calculation, GW method is an effective way to consider the many body effect for TMD materials, too.⁸⁸⁻⁹⁰⁾ However, the shapes of the electronic energy bands calculated by GW method are almost the same as the case of DFT calculation⁸⁸⁻⁹⁰⁾ and thus the shapes of absorption spectra should not change except for the value of the energy gap. The optical absorption coefficient α around the K (denoted by A and B), Λ (A' and B'), and M (M) points are large where the corresponding transition in the \mathbf{k} -space are shown in Fig. 3-5 (a). It is clear that intensity of the optical absorption is large if the laser energy matches with the energy separation at the Λ valley or the M point compared with that at the K (K') point. Strong absorption at the Λ valley is due to the nesting of the two energy bands along to the Λ - Γ line.^{62,63)} As for the M point, two dimensional

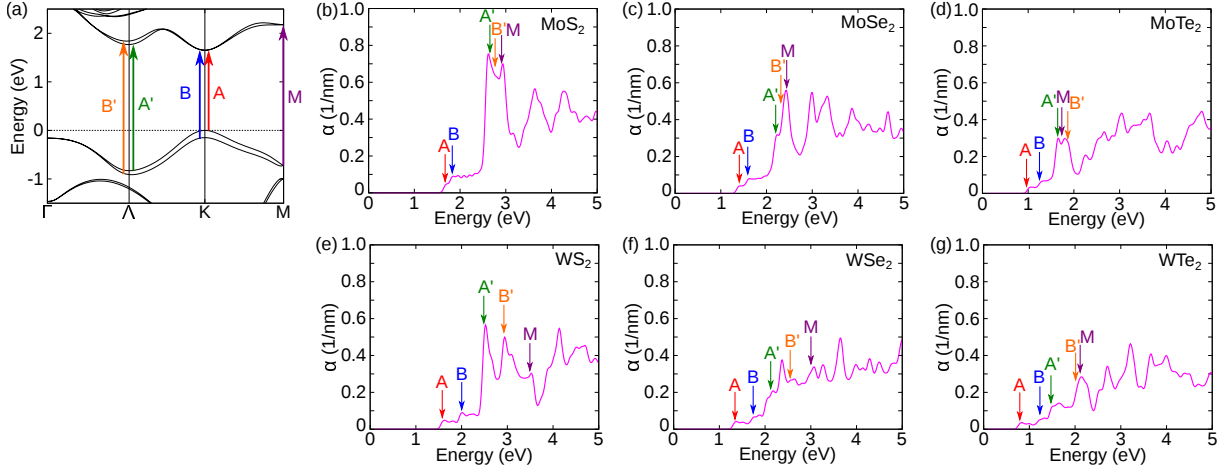


Figure 3-5: (a) Significant optical transition paths in TMDs in the low energy region. (b)-(g) Optical absorption coefficient of six TMD materials. Excitation energy of A, B, A', B', and M path in Fig. (a) are also shown by arrows.

van Hove singularity for joint density of states contributes to the strong absorption. When we compare Figs. 3-5 (b)-(d) with that of Figs. 3-5 (e)-(g), we can point out that the spin-orbit interaction (between A and B) and energy separation between Λ and M (A', B', and M) are large for W compared with Mo. The spin splitting has small modification by changing S, Se, and Te since the wave functions around the K (K') and Λ (Λ') points mainly consist of Mo or W atoms.

In Figs. 3-6 (a)-(d), we illustrate the color plot of the intensity of the matrix elements $|M_{\text{opt}}^{\text{cv}}(\mathbf{k})|$ in the hexagonal Brillouin zone for LCP or RCP light in monolayer MoS₂. In the case of $E_L = 1.65$ eV [Fig 3-6 (a)], only the electrons near the K (K') point can be excited by RCP (LCP) light and 100% valley polarization is achieved. When E_L increases to $E_L = 1.82$ eV [Fig 3-6 (b)], the region of the strong optical transition near the K (K') point becomes larger and the degree of the valley polarization becomes small. In the case of $E_L = 2.60$ eV [Fig. 3-6 (c)] which corresponds to the excitation energy of the Λ nesting region, the optical transition by circularly polarized light occurs selectively for either the Λ or Λ' valley. The intensity of the optical transition at the Λ (Λ') valley [Fig. 3-6 (c)] is dominant compared with that at the K (K') valley [Fig. 3-5 (b)] since the corresponding matrix elements become relatively large, and thus we can say that the Λ valley is important for obtaining many valley-polarized electrons.

3.2. LASER ENERGY DEPENDENCE OF VALLEY POLARIZATION IN TMDS57

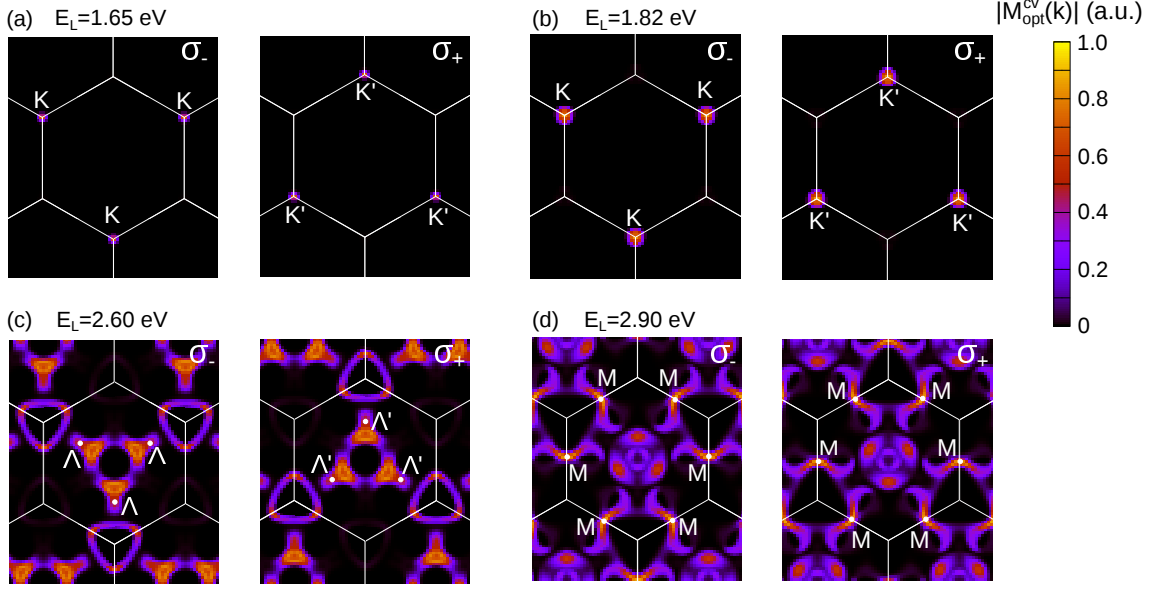


Figure 3-6: (a)-(d) Color plot of the absolute value of the matrix elements $|M_{\text{opt}}^{\text{cv}}(\mathbf{k})|$ in the two dimensional Brillouin zone of monolayer MoS_2 for RCP (σ_-) and LCP (σ_+) light, inducing the excitation energy E_L of (a) 1.65, (b) 1.82, (c) 2.60, and (d) 2.90 eV.

3.2.3 Degree of valley polarization

In order to evaluate how absorbed light is valley-polarized, we define the degree of the valley polarization $\rho^\xi(E_L)$ ($\xi = \text{K}$ or K') as follows,

$$\rho^\xi(E_L) = -\frac{I_{\sigma_+}^\xi(E_L) - I_{\sigma_-}^\xi(E_L)}{I_{\sigma_+}^\xi(E_L) + I_{\sigma_-}^\xi(E_L)}, \quad (3.44)$$

where $I_{\sigma_+}^\xi(E_L)$ [$I_{\sigma_-}^\xi(E_L)$] is the intensity of the optical absorption at the ξ valley for the σ_+ (σ_-) light. $\rho^\xi(E_L) = 1$ (or -1) corresponds to 100% valley polarization when only the RCP (LCP) light is absorbed around the ξ valley. In order to calculate the valley polarization, we divide the hexagonal Brillouin zone into the two regions [orange and green area in Fig. 3-7 (a)] around either the K or K' point and define a \mathbf{k} -point in the each region to belong to the K or K' vally region.

In Figs. 3-7 (b)-(g), we plot the degree of the valley polarization $\rho^\xi(E_L)$ (black line), intensity of the optical transition $I_{\sigma_\pm}^K(E_L)$ (red or blue line), and the difference of the intensity $|I_{\sigma_+}^\xi(E_L) - I_{\sigma_-}^\xi(E_L)|$ (green line) for RCP and LCP light near the K point shown by orange region in Fig. 3-7 (a). The degree of the valley polarization and the intensity of the optical absorption for RCP and LCP around the K and K' point has following relations: $\rho^K(E_L) = -\rho^{K'}(E_L)$, $I_{\sigma_+}^K = I_{\sigma_-}^{K'}$, and $I_{\sigma_-}^K = I_{\sigma_+}^{K'}$ as a

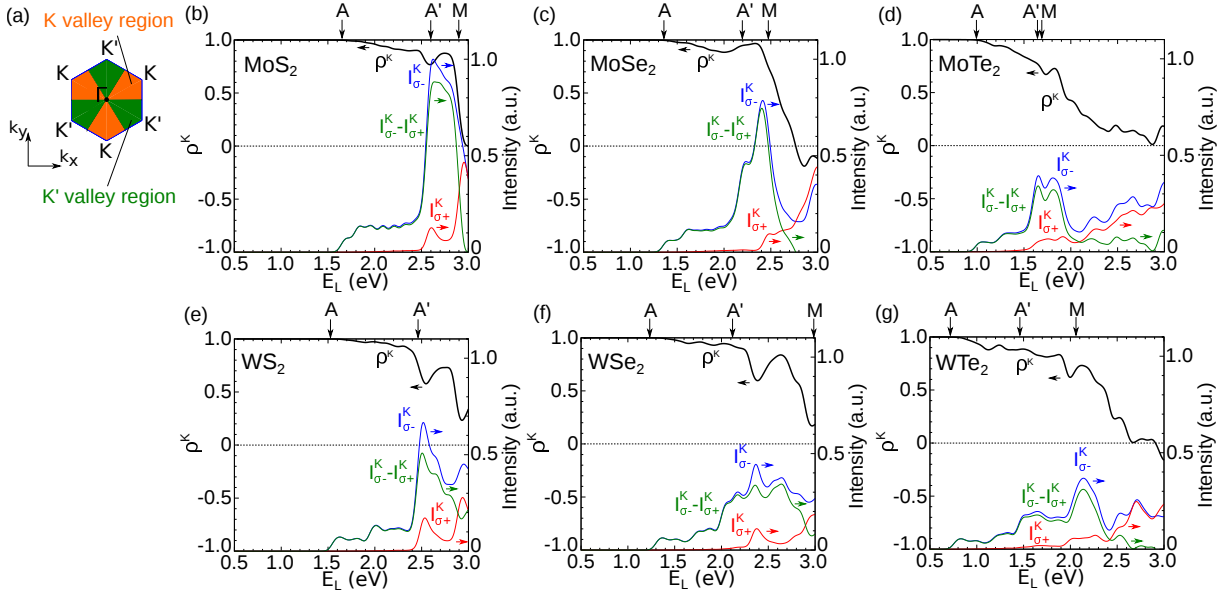


Figure 3-7: (a) Two dimensional Brillouin zone which is divided to the region near the K and K' valleys. (b)-(g) Laser energy dependence of the degree of the valley polarization of the optical transition [$\rho^K(E_L)$], intensity of the optical absorption in the K valley region excited by circularly polarized light [$I_{\sigma_{\pm}}^K(E_L)$], and difference of the intensity for RCP and LCP incident light in the K valley region [$I_{\sigma_-}^K(E_L) - I_{\sigma_+}^K(E_L)$]. The excitation energy at the K (K'), Λ , and M shown in Fig. 3-5 (a) are also shown by A, A', and M. The energy position M of WS₂ is about 3.5 eV and out of the range shown in Fig. (e).

consequence of time reversal symmetry between the K and K' valleys. The degree of the valley polarization $\rho^K(E_L)$ is almost the unity near the gap energy shown at the label A in Figs. 3-7 (b)-(g) and decreases with increasing E_L . It is important to point out that $I_{\sigma_-}^K(E_L) - I_{\sigma_+}^K(E_L)$ is the largest at $E_L = 2.60$ eV for MoS₂ for the transition shown by A' in Fig. 3-7 (a). The maximum difference of the intensity corresponds to the transition around the Λ (Λ') valley. The optical transition around the Λ (Λ') valley is much stronger than the K (K') point. However, the degree of the valley polarization at the Λ (Λ') valley can not be the unity but 0.8. Though excitation at the Λ (Λ') valley holds information of the valley polarization for MoS₂, the degree of the valley polarization rapidly decreases when the excitation at the M point contributes to $I_{\sigma_{\pm}}^K$. It can be understood from Fig. 3-6 (d) that absorption occurs at the M point for both of RCP and LCP light.

In Table 3.1, we show the maximum value of the $I_{\sigma_-}^K - I_{\sigma_+}^K = I_{\sigma_-}^K - I_{\sigma_-}^{K'}$ defined by $\Delta I_{K-K'}^{\max}$, and the laser energy to give $\Delta I_{K-K'}^{\max}$ for six TMD materials. Since DFT calculation underestimates the energy gap as is discussed in the previous section, we

3.2. LASER ENERGY DEPENDENCE OF VALLEY POLARIZATION IN TMDS59

Table 3.1: Calculated parameters to give the maximum difference for the optical transition of RCP and LCP light around the K point in six TMD materials. E_g^K and E_g^Λ are the energy gap at the K and Λ valleys, respectively. E_L^{\max} , $\Delta I_{K-K'}^{\max}$, and $\rho^K(E_L^{\max})$ are, respectively, the laser energy to give the maximum value of $I_{\sigma_-}^K - I_{\sigma_+}^K$, maximum value of $I_{\sigma_-}^K - I_{\sigma_+}^K$, and the degree of the valley polarization for the laser energy of E_L^{\max} . Optical band gap E_g^{exp} measured by the experiments (Photoluminescence^{27,32,33} and ARPES³¹) and the difference of the energy gap between theory and experiment $E_g^{\text{exp}} - E_g^K$ are also shown. The values in the brackets are the energy for the upshifted energy bands to fit the experimental data.

	E_g^{exp} [eV]	E_g^K [eV]	$E_g^{\text{exp}} - E_g^K$ [eV]	E_g^Λ [eV]	E_L^{\max} [eV]	$\Delta I_{K-K'}^{\max}$	$\rho^K(E_L^{\max})$
MoS ₂	1.83 ^{a)}	1.65	0.18	2.60 (2.78)	2.64 (2.82)	0.88	0.80
MoSe ₂	1.58 ^{b)}	1.36	0.22	2.20 (2.42)	2.40 (2.62)	0.75	0.92
MoTe ₂	1.10 ^{c)}	0.99	0.11	1.64 (1.75)	1.65 (1.76)	0.34	0.77
WS ₂	1.96 ^{d)}	1.52	0.44	2.47 (2.91)	2.51 (2.95)	0.51	0.62
WSe ₂	1.65 ^{d)}	1.22	0.43	2.12 (2.55)	2.64 (3.07)	0.34	0.84
WTe ₂	- ^{e)}	0.71	-	1.47	2.14	0.31	0.73

a) Ref. 27 (PL), b) Ref. 31 (ARPES), c) Ref. 32 (PL), d) Ref. 33 (PL), e) no data.

also show the the corresponding energy by upshifted conduction energy bands to fit the experiment. In the six TMD materials, MoS₂ and MoSe₂ show large valley polarization, compared with other four materials. This is because the nesting region of the highest valence and lowest conduction bands for MoS₂ and MoSe₂ is much larger than other four materials [see Figs. 3-5 (a) and (b)]. Furthermore, $\Delta I_{K-K'}^{\max}$ for MoS₂ and MoSe₂ is larger than other TMDs. $\Delta I_{K-K'}^{\max}$ decreases with increasing the weight of TMDs. The reason is due to small spin splitting of energy bands and thus larger value of $\Delta I_{K-K'}^{\max}$ is expected since both up- and down-spin energy bands contribute to the optical transition. In other words, spin-up and down electrons excite for same laser energy around the same valley and it is difficult to excite electrons with different spin separately in MoS₂ and MoSe₂. $\Delta I_{K-K'}^{\max}$ is small for TMDs with W atom. However, they have a possibility to achieve spin- and valley-selective optical excitation due to the large spin-orbit interaction.

Generally, observing the valley polarization in the optical absorption is difficult since two valleys are energetically degenerate. Many experiments have observed the valley polarization for photoluminescence, excited by circularly polarized light.^{11-19,21,22} However, we might not be able to observe the photoluminescence at the exciton of the Λ valley since there is no hill at the Λ point in valence bands and hole cannot be relaxed to the Λ point. In order to observe the valley polarization of the Λ and Λ'

valleys, we need to break the time reversal symmetry of the system. It is reported that intense circularly polarized pump light lifts the degeneracy of the K and K' valleys by the optical Stark effect in WS₂, which makes us distinguish the absorption of RCP and LCP light.²⁴⁾ We also can break the time reversal symmetry by applying magnetic field.^{20,23)} We predict that we can observe the valley polarization at the Λ (Λ') valley by measuring the optical absorption for RCP and LCP light by breaking the time reversal symmetry.

Chapter 4

Optical anisotropy of Gallium telluride and Black phosphorus

In this chapter, we discuss the anisotropy of the optical absorption and Raman spectra as a function of the polarization direction of incident laser light. In the low symmetry material such as gallium telluride (GaTe) and black phosphorus (BP), the optical absorption and Raman intensity are anisotropic depending on the in-plane polarization direction of light. The anisotropies for optical absorption and Raman intensity also depend on the excitation laser energy and sample thickness which is difficult to be evaluated by the Raman tensor discussed in Sec. 1.3.3. The laser energy dependence is discussed by considering the selection rule of the optical matrix element for the given electronic energy bands with the group theory analysis. The thickness dependence is discussed by using transfer matrix for optical absorption, and by calculating enhancement factor for Raman intensity. In Sec. 4.1 and 4.2, we discuss the anisotropic optical properties of GaTe and BP, respectively, by using group theory analysis, transfer matrix, and enhancement factor of Raman intensity.

4.1 Gallium telluride

As is discussed in Sec. 1.3.1, Gallium telluride (GaTe) is the atomic layer material which recently attracts an interest by its high photoresponsibility.⁴³⁾ The structure of GaTe is already known more than five decades ago⁹¹⁾, however, GaTe attracts attention again with the recent upsurge of the interests for the atomic layers.

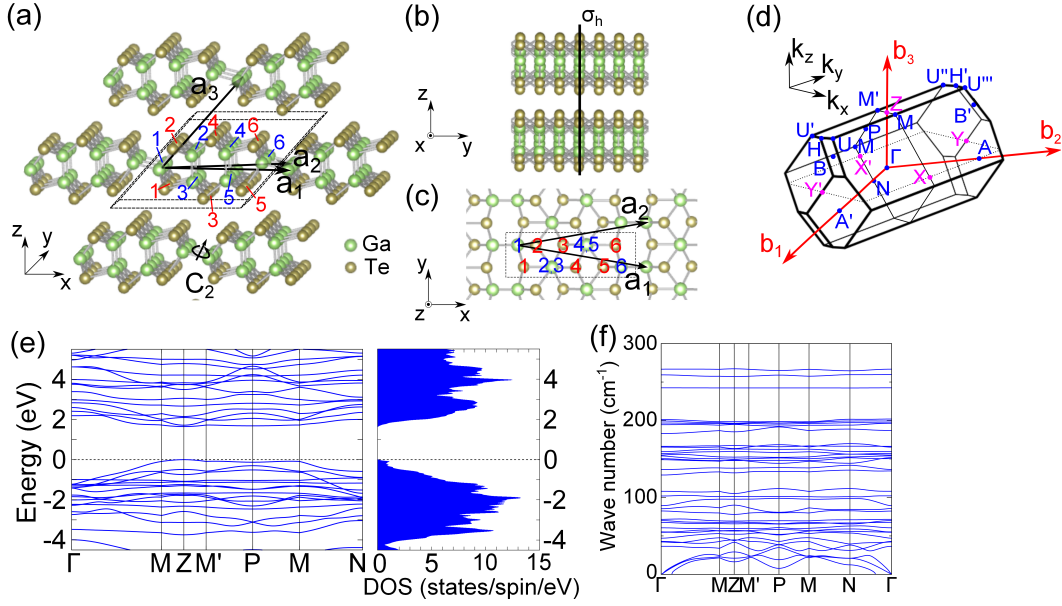


Figure 4-1: (a)-(c) Crystal structure of bulk GaTe of (a) front, (b) side, and (c) top view. (d) First Brillouin zone for the triclinic primitive unit cell of bulk GaTe. (e) Electronic energy bands along the Γ -M-Z-M'-P-M-N and density of states for bulk GaTe. (f) Phonon dispersion relation along Γ -M-Z-M'-P-M-N- Γ of bulk GaTe.

4.1.1 Crystal, electronic and phonon structure of bulk GaTe

In Fig. 4-1 (a)-(c), we show the crystal structure of bulk GaTe. Bulk GaTe consists of 6 Ga and 6 Te atoms in the primitive unit cell. Bulk GaTe belongs to C_{2h}^3 ($C/2m$) symmetry^{43,91,92}, which has two-fold rotational axis along in-plane y axis and a mirror plane ($x-z$ plane) perpendicular to the layer plane [see Fig. 4-1 (a)-(b)]. The layers of GaTe are stacked each other by van der Waals force.

In Fig. 4-1 (e), we show the electronic energy band structure of bulk GaTe along Γ -M-Z-M'-P-M-N- Γ calculated by DFT. The calculated energy bands are flat around both the top of valence band and the bottom of conduction band with the direct energy band gap at the Z point ($E_g = 1.65$ eV) and slightly larger energy band gaps at the P and M point ($E_g = 1.80$ eV), which is in good agreement with previous works^{37,93}.

In Fig. 4-1 (f), we show the phonon dispersion of bulk GaTe calculated by first-principles density functional perturbation theory (DFPT). According to the group theory, bulk GaTe has 18 Raman active phonon modes in which there are 12 A_g and 6 B_g modes. The phonon dispersion is flat Γ -M-Z-M'-P-M-N line. We illustrate the vibration of 36 phonon modes in bulk GaTe shown in Fig. 4-2.

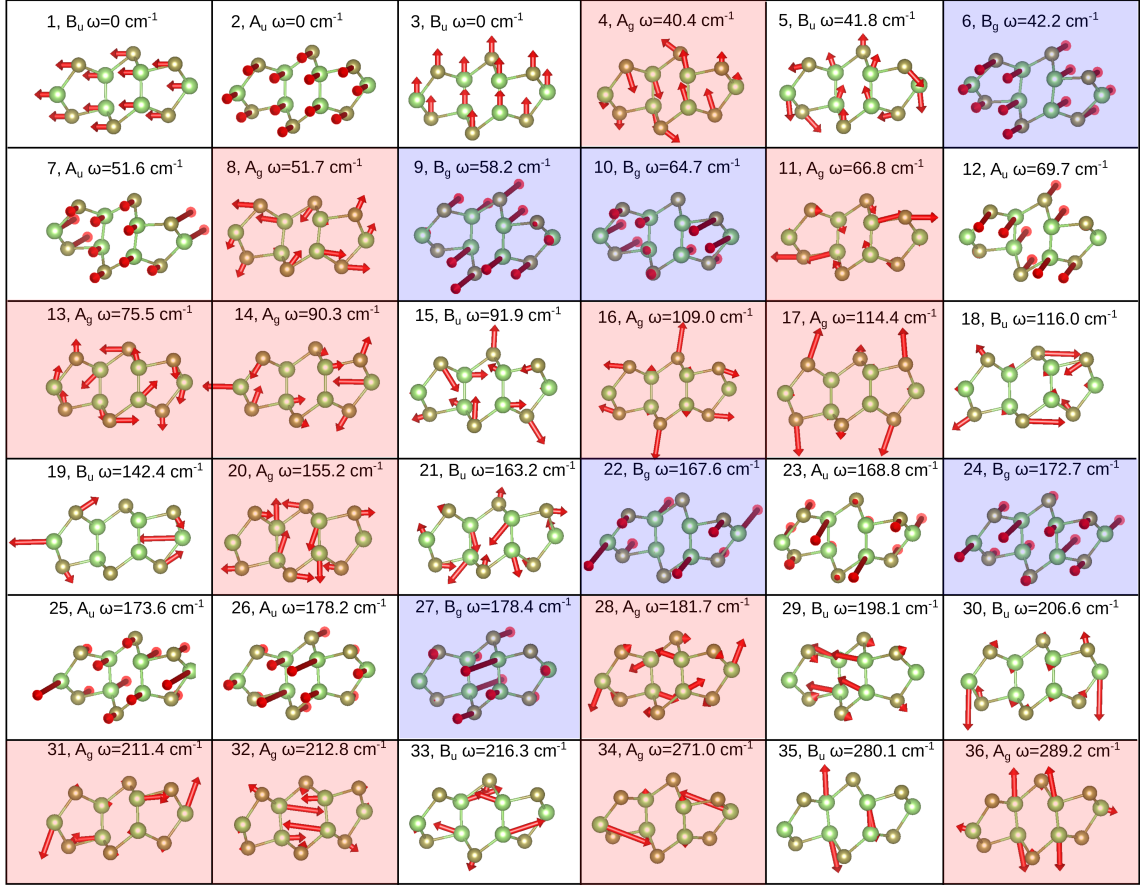


Figure 4-2: Illustration of the atomic vibrational motions of the phonon modes at the Γ point in bulk GaTe. Raman active A_g (B_g) mode is shown by red (blue) box.

4.1.2 Optical absorption

In Fig. 4-3 (d), we show the polarization dependence of the optical extinction in GaTe by the experiment.⁵⁴⁾ The anisotropy of the optical extinction in GaTe is not so large but we can see that the extinction for x - (0°) polarization is slightly stronger than that for y - (90°) polarization. The reason of the anisotropy of the extinction can be understood by the group theory analysis with the electronic structure. In Fig. 4-4 (a), we show the symmetry of the eigen state near the Fermi energy at the symmetrical point (Z and P) in C_{2h}^3 space group. The electronic energy bands of bulk GaTe is flat around the top of valence and the bottom of conduction bands near the Z and P points. Then the main contribution for the optical absorption is that from the electronic energy bands near the Fermi energy at around the Z and P points. As shown in Fig. 4-4 (b), the electron-photon matrix elements near the Fermi energy have

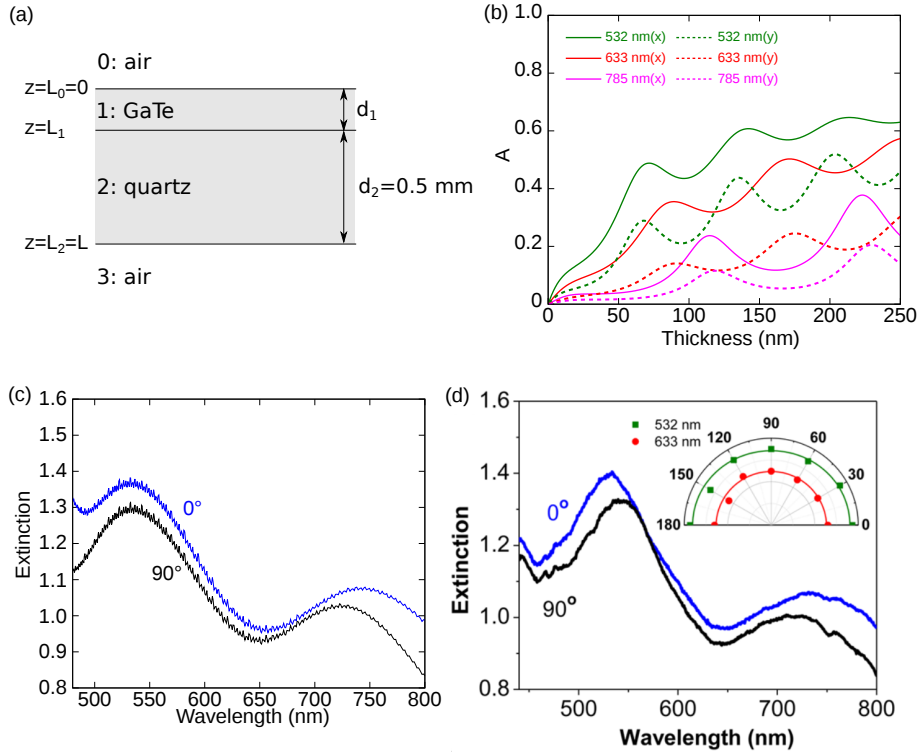


Figure 4-3: (a) Geometrical arrangement for the measurement of bulk GaTe sample. (b) GaTe sample thickness dependence of the calculated optical absorption probability for x - (solid line) and y - (dashed line) polarized light. The calculated results for the three laser energies (532, 633, 785 nm) are shown. (c) Calculated optical extinction, fitted to the experiment of the 112 nm thick sample. (d) Experimental optical extinction spectra of GaTe.⁵⁴⁾

the symmetry of the x -polarization while the electron-photon matrix elements for y -polarization appears for higher excitation energy E_L , and thus the optical absorption of bulk GaTe has x -polarization for the E_L near the energy gap while the anisotropy of the optical absorption becomes weak with increasing the E_L .

The optical extinction spectra has the non-zero value of the extinction even when the E_L is smaller than the energy gap (1.65 eV = 752 nm) of bulk GaTe as shown in Fig. 4-3 (d). This indicates that we have to consider the contribution of not only the absorption but also the reflection by the sample. The optical property (absorption, reflection, and transmission) depends on the thickness of the sample and the substrate. Thus the extinction ratio for x - and y -polarization should have a thickness dependence. We analyze the thickness dependence of the optical extinction for bulk GaTe by transfer matrix method (see Appendix B). As shown in Fig. 4-3 (a), we consider the experimental setup that the GaTe sample with thickness d_1 nm on a $d_2 = 0.5$ nm

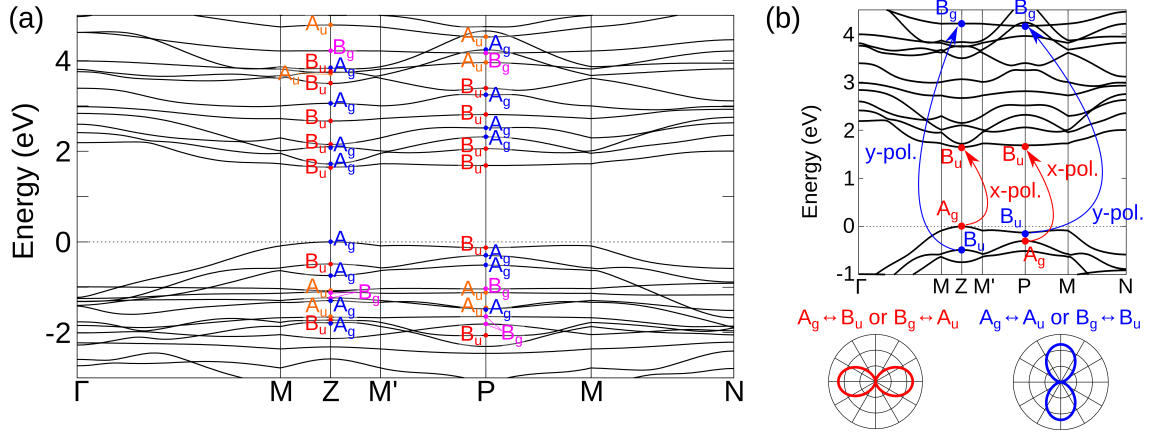


Figure 4-4: (a) Symmetry assignment of the electronic energy bands of bulk GaTe at the Z and P points in the Brillouin zone. Different colors indicate the different symmetries. (b) The polarization direction of the electron-photon matrix elements.

Table 4.1: Selection rules of optical transitions for the C_{2h}^3 space group. These selection rules correspond to the electron-photon matrix element $\langle f | \nabla | i \rangle$, which is coupled by the inner product with polarization vector \mathbf{p} .

x -polarized light $\nabla = B_u$		y -polarized light $\nabla = A_u$	
$ f\rangle$	$ i\rangle$	$ i\rangle$	$ f\rangle$
B_u	A_g	A_u	A_g
A_u	B_g	B_u	B_g
B_g	A_u	A_g	A_u
A_g	B_u	B_g	B_u

quartz substrate. Then we apply the 4 medium (0: air, 1: GaTe, 2: quartz 3:air) system as shown in Fig. 4-3(a) to calculate the transimission, reflection, and absorption by transfer matrix. By using transfir matrix of this system, the reflection and transmission coefficients are given by (see Appendix B for the derivation of transfer matrix)

$$r = \frac{M_{11}\Gamma_0 + M_{12}\Gamma_0\Gamma_3 - M_{21} - M_{22}\Gamma_3}{M_{11}\Gamma_0 + M_{12}\Gamma_0\Gamma_3 + M_{21} + M_{22}\Gamma_3}, \quad (4.1)$$

$$t = \frac{2\Gamma_0}{M_{11}\Gamma_0 + M_{12}\Gamma_0\Gamma_3 - M_{21} - M_{22}\Gamma_3}, \quad (4.2)$$

where M_{ij} is the ij component of transfer matrix and $\Gamma_i = \tilde{n}_i / \sqrt{\frac{\epsilon_0}{\mu_0}}$. By using Eqs. (4.1) and (4.2), reflection, transmission, and absorption probabilities (\mathcal{R} , \mathcal{T} , and \mathcal{A}) are given

by,

$$\mathcal{R} = |r|^2, \quad (4.3)$$

$$\mathcal{T} = |t|^2, \quad (4.4)$$

$$\mathcal{A} = 1 - \mathcal{R} - \mathcal{T}. \quad (4.5)$$

We note that the transfer matrix is the function of the refractive index and the thickness of sample and substrate. Thus, in order to calculate the absorption probability by the transfer matrix method, we need to obtain the complex refractive index of GaTe. We firstly calculate the refractive index by a first-principles calculation. The refractive index of quartz (SiO_2) substrate as a function of the wavelength is adopted from Malitson et al.⁹⁴). In Fig. 4-3 (b), we show the optical absorption probability for x - and y -polarized light with the wave length of 532, 633, and 785 nm, calculated by transfer matrix method. Absorption probability oscillates by the interference effect with the quartz substrate as shown in Fig. 4-3 (b). The calculated optical absorption has a finite value even when the laser energy is 1.58 eV (=785 nm) which is smaller than the the energy gap (1.65 eV) of GaTe.

In order to match the calculation result to the experimental extinction spectra, we did the following analysis. GaTe is a semiconductor and thus the absorption by the exciton is expected.^{37,92} As discussed in Sec. 2.3, the extinction function is related to the optical absorption and then we put the artificial exciton absorption term in the extinction function κ as follows;

$$n = \sqrt{\frac{\sqrt{\varepsilon_r'^2 + \varepsilon_r''^2} + \varepsilon_r'}{2}}, \quad (4.6)$$

$$\kappa = \sqrt{\frac{\sqrt{\varepsilon_r'^2 + \varepsilon_r''^2} - \varepsilon_r'}{2}} + \frac{I}{\sqrt{2\pi}\sigma} \exp\left(\frac{(\hbar\omega - E_0)^2}{2\sigma^2}\right). \quad (4.7)$$

We take into account the term $\frac{I}{\sqrt{2\pi}\sigma} \exp\left(\frac{(\hbar\omega - E_0)^2}{2\sigma^2}\right)$ in Eq. (4.7) in order to describe the absorption by the exciton whose excitation energy is $E_0 = 1.62$ - 1.66 eV. The real and imaginary part of dielectric constants ε' and ε'' are, respectively, given by using Drude-Lorentz model:

$$\varepsilon' = 1 - \frac{\omega_p^2(\omega^2 - \omega_0^2)^2}{(\omega^2 - \omega_0^2)^2 + (\omega/\tau)^2}, \quad (4.8)$$

$$\varepsilon'' = \frac{\omega_p^2(\omega/\tau)}{(\omega^2 - \omega_0^2)^2 + (\omega/\tau)^2}, \quad (4.9)$$

Table 4.2: Laser wavelength dependence of the complex refractive index \tilde{n} of bulk GaTe for the x - and y - directions, SiO₂⁹⁴⁾, and Si.⁹⁵⁾ The refractive index for GaTe is given by first-principles calculation.⁵⁴⁾

Wavelength	GaTe (x)	GaTe (y)	SiO ₂	Si
532 nm	3.70-0.515i	3.87-0.211i	1.46	4.21-0.010i
633 nm	3.74-0.318i	3.65-0.0926i	1.46	4.14-0.0010i
785 nm	3.59-0.0923i	3.49-0.0389i	1.46	4.00-0.0010i

where $\hbar\omega$ corresponds to the laser energy. In order to reproduce the experiments, we fit with the experiments and determine the parameters: $\hbar\omega_0$, $\hbar\omega_p$, τ , I , σ , and E_0 . We thus obtain the parameter as: $\hbar\omega_0 = 3.6$ eV, $\hbar\omega_p = 10.2$ eV, $\tau/\hbar = 2.7$ eV⁻¹, $I = 0.17$ eV, $\sigma = 0.20$ eV, and $E_0 = 1.62$ eV for x - (0°) polarized light, and $\hbar\omega_0 = 3.8$ eV, $\hbar\omega_p = 11.0$ eV, $\tau/\hbar = 2.7$ eV⁻¹, $I = 0.14$ eV, $\sigma = 0.18$ eV, and $E_0 = 1.66$ eV for y - (90°) polarized light. In Fig. 4-3 (c), we show the optical extinction spectra obtained by the Drude-Lorentz model with the above fitting parameters. In order to compare with experiment directly, we evaluate the optical extinction $\ln(T_{\text{substrate}}/T)$, where T and $T_{\text{substrate}}$ are the transmission probability of the sample with the substrate, and only the substrate, respectively. From the fitted calculation result, we think that the peak at 530 nm (2.34 eV) is given by an interference effect and the peak at 730 nm (1.70 eV) is given by the absorption in GaTe since 1.70 eV is almost same with the energy gap of GaTe.

4.1.3 Raman spectra

The polarization dependence can be found in Raman intensity of bulk GaTe, too. We discuss about the polarization dependence of Raman intensity in this subsection. We also consider the polarization dependence with the sample thickness by the interference effect.

We firstly calculate the non-resonant Raman spectra by first-principles calculation with Placzek approximation⁹⁶⁾ and clarify the observed Raman peak in the experiment (see Fig. 4-5). We observe 9 Raman peaks at 107, 115, 126, 142, 161, 176, 208, 268, and 280 cm⁻¹ in the experiment. The peaks at 126 and 141 cm⁻¹ can not be assigned from the theoretical calculation for non-resonant Raman spectra and we conclude that these two peaks are double resonant Raman peaks which emit two phonon (see Section 1.3.3). The peak width is larger compared with other peaks since a lot of combinations of $\mathbf{q} \neq 0$ phonons contribute to the double resonant Raman process. There are 6 Raman

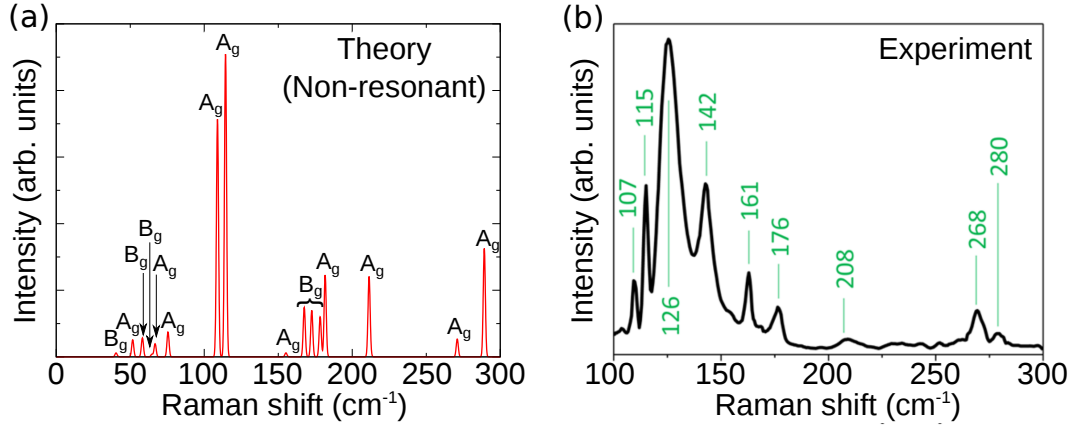


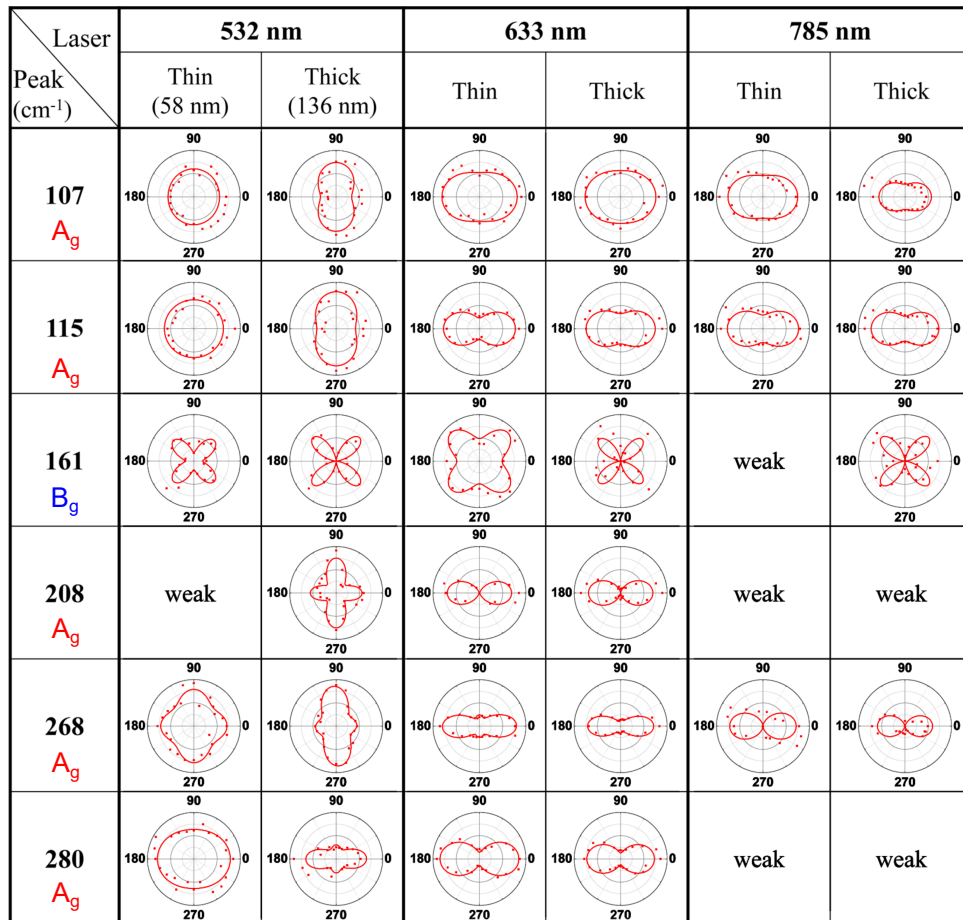
Figure 4-5: (a) Non-resonant Raman spectra of bulk GaTe by first-principles calculation with Placzek approximation. (b) Experimental Raman spectra of a 125 nm thick GaTe flake at room temperature under vacuum (10^{-5} mbar). The measurement was performed with 532 nm laser excitation.

active (A_g and B_g) Γ point phonons from 50 to 80 cm^{-1} and the phonon dispersion relations of these phonons are flat as shown in Fig. 4-1 (f). We guess that the strong double resonant Raman peaks at 126 and 142 cm^{-1} is originated from the combination of these A_g and B_g phonon modes (60-70 cm^{-1}). The anisotropy of the double resonant peak becomes weak since many kinds of phonons with different symmetry and different \mathbf{q} values contribute to the Raman process [see Fig. 4-6 (b)]. Among the remaining seven peaks, five peaks at 107, 115, 208, 268, and 280 cm^{-1} are A_g modes and two peaks at 161 and 176 cm^{-1} are B_g modes. The peak at 176 cm^{-1} probably includes three B_g Raman peaks around 176 cm^{-1} in the theoretical calculation in Fig. 4-5. In Fig. 4-6 (a), we show the polar plot of the Raman intensity for the first order Raman peaks as a function of the polarization of light. We can see the strong polarization for 0° or 90° (45°) in A_g (B_g) Raman peak. This anisotropic polarization of Raman intensity can be understood by the simple calculation by Raman tensor, but Raman tensor tells us only the selection rule of Raman intensity depending on the symmetry of phonon mode. We discuss the detail of the angle-dependent anisotropic Raman intensity by considering the quantum mechanical formula of Raman intensity given by Eq. (2.89). The numerator of the Raman intensity formula is given by the production of two electron-photon matrix elements M_{opt} for incident and scattered light accompanied with an electron-phonon matrix element M_{ep} . Then the characteristic shapes of the Raman intensity polar plots for the A_g and B_g modes are explained by analyzing the symmetry of the matrix elements. The polarization vector which gives the anisotropic

Fig. 4-5: fig/ch4-raman-gate.eps

Fig. 4-6: fig/ch4-aniso-raman-gate.eps

(a) First order Raman peak



(b) Second order Raman peak

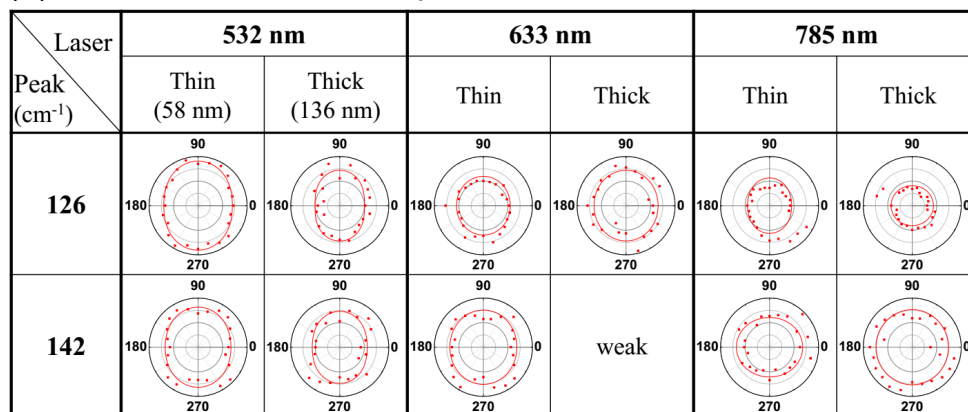


Figure 4-6: The experimental Raman intensity polar plot for the (a) first (107, 115, 161, 208, 268, and 280 cm⁻¹) and (b) second (126 and 142 cm⁻¹) order Raman spectrum peaks. Two samples with different thickness (58 and 136 nm) for three laser excitation energies (532, 633, and 785 nm) are shown. The angle 0° (90°) corresponds to x- (y-) polarization.

Table 4.3: Selection rules of Raman scattering for the A_g mode. $|i\rangle$, $|m\rangle$ and $|m'\rangle$ are the initial state and two intermediate states, respectively. xx (yy) are polarization vectors for the incident and scattered light: both are x - (y -) polarized. These selection rules correspond to the product of the matrix elements: $\langle f|H_{\text{opt}}^x|m'\rangle\langle m'|H_{\text{ep}}(A_g)|m'\rangle\langle m|H_{\text{opt}}^x|i\rangle$ and $\langle f|H_{\text{opt}}^x|m'\rangle\langle m'|H_{\text{ep}}(A_g)|m'\rangle\langle m|H_{\text{opt}}^y|i\rangle$.

xx		yy	
$ i\rangle = f\rangle$	$ m\rangle = m'\rangle$	$ i\rangle = f\rangle$	$ m\rangle = m'\rangle$
A_g	B_u	A_g	A_u
B_g	A_u	B_g	B_u
A_u	B_g	A_u	A_g
B_u	A_g	B_u	B_g

Table 4.4: Selection rules of Raman scattering for the B_g mode. The polarization is different for the incident and scattered light for the B_g mode. xy means that the incident light is y -polarized, and the scattered light is x -polarized. These selection rules correspond to the product of the matrix elements $\langle f|H_{\text{opt}}^x|m'\rangle\langle m'|H_{\text{ep}}(B_g)|m'\rangle\langle m|H_{\text{opt}}^y|i\rangle$ and $\langle f|H_{\text{opt}}^y|m'\rangle\langle m'|H_{\text{ep}}(B_g)|m'\rangle\langle m|H_{\text{opt}}^x|i\rangle$.

xy			yx		
$ i\rangle = f\rangle$	$ m\rangle$	$ m'\rangle$	$ i\rangle = f\rangle$	$ m\rangle$	$ m'\rangle$
A_g	A_u	B_u	A_g	B_u	A_u
B_g	B_u	A_u	B_g	A_u	B_u
A_u	A_g	B_g	A_u	B_g	A_g
B_u	B_g	A_g	B_u	A_g	B_g

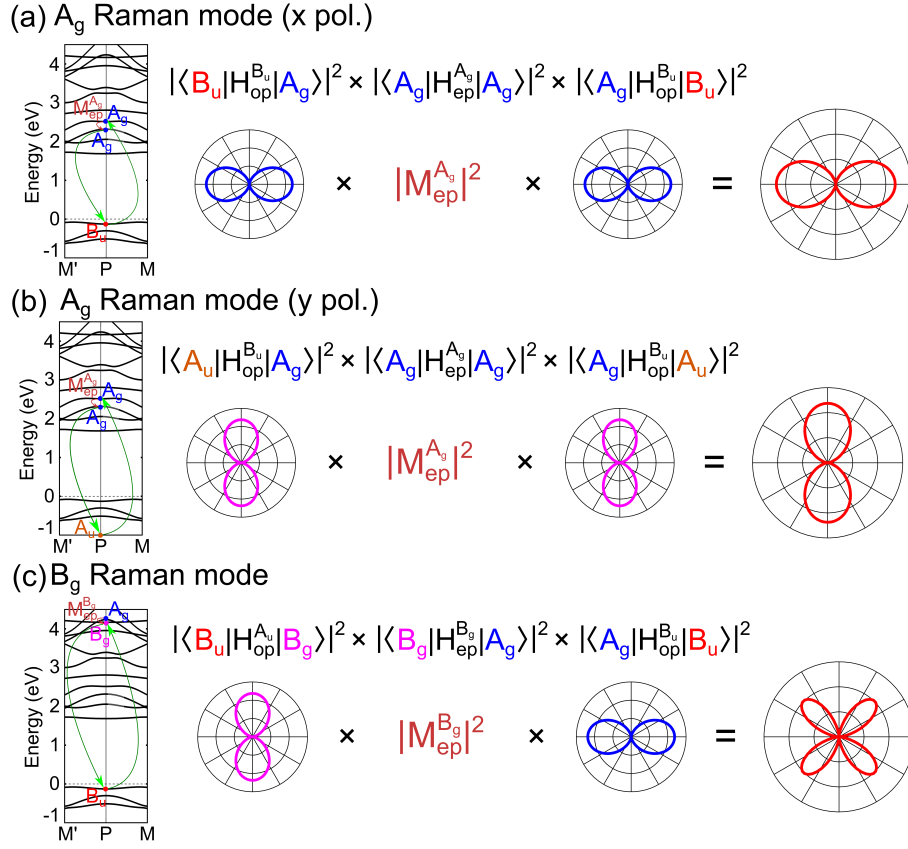


Figure 4-7: One of the expected transition process for Raman scattering and the expected polarization shape for the A_g and B_g modes at the P point.

polarization is only included in the electron-photon matrix element and we assume that the electron-phonon matrix element does not have anisotropy. Within this assumption, the anisotropy of Raman intensity is originated from the production of the two matrix elements. The electron-phonon matrix element only gives the selection rule of the transition connecting the two electron-photon matrix elements. In Fig. 4-7, we show an example of the transition corresponding to the A_g and B_g mode at the P point. The selection rule of the process for Raman scattering can be determined by group theory which is shown in Table 4.3 and 4.4. For the A_g mode, the intermediate m and m' states have the same symmetry, and thus the two electron-photon matrix elements in Eq. (2.89) has same polarization direction. Then the Raman intensity is polarized for 0° or 90° direction. On the other hand, the intermediate m and m' states for B_g mode have the different pattern that has the maximum at 45° polarization direction. Using the above analyses, we can explain the phenomena of change of the pattern. As shown in the polar plots of Fig. 4-6 (a), the major axis of A_g peaks for 532

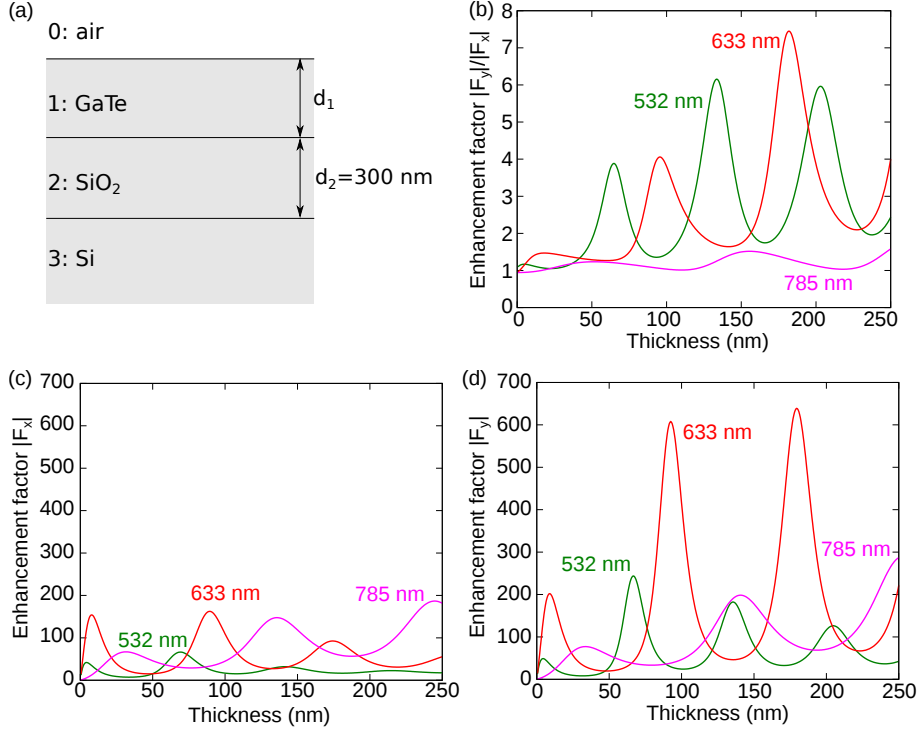


Figure 4-8: Calculated results for the enhancement factor for the interference effect on the Raman intensity. (a) Geometrical arrangement of the experiment. (b) The ratio of the enhancement factor for x - and y -polarized light as a function of GaTe thickness. (c-d) GaTe thickness dependence of the enhancement factor for x - (c) and y - (d) polarized light. Calculated results for the three laser wavelengths (532, 633 and 785 nm) are shown.

nm is 0° while that for 633 and 785 nm is 90° . This is because 532 nm (2.33 eV) laser can excite the electrons to higher energy bands with the polarization of 90° direction. As discussed in the part of the optical absorption, the electron-photon matrix elements near the Fermi energy have the value for x - (0°) polarization and the Raman intensities for 633 nm (1.96 eV) and 785 nm (1.57 eV) have the values for x - (0°) polarization.

Anisotropy of the Raman intensity depends on the thickness, too. We have to consider effect of the interference to explain the thickness dependence. We assume that the geometry of the experimental set up is given as shown in Fig. 4-8 (a). When we consider the interference effect with the substrate, net Raman intensity is given by $I = I_i \cdot F$ where I_i is the intrinsic Raman intensity originated from the structure of the material with the enhancement factor F .⁹⁷⁻⁹⁹⁾ The enhancement factor F is given by

(see Appendix B for the derivation)

$$F = \int_0^{d_1} |F_{ex} \cdot F_{sc}|^2 dz, \quad (4.10)$$

with the term of excitation and scattering as follows,

$$F_{ex} = t_{01} \frac{(1 + r_{12}r_{23}e^{-2i\beta_2}) e^{-i\beta z} + (r_{12} + r_{23}e^{-2i\beta_2}) e^{-2i(\beta_1 - \beta z)}}{1 + r_{12}r_{23}e^{-2i\beta_2} + (r_{12} + r_{23}e^{-2i\beta_2}) r_{01}e^{-2i\beta_1}}. \quad (4.11)$$

$$F_{sc} = t_{10} \frac{(1 + r_{12}r_{23}e^{-2i\beta_2}) e^{-i\beta z} + (r_{12} + r_{23}e^{-2i\beta_2}) e^{-2i(\beta_1 - \beta z)}}{1 + r_{12}r_{23}e^{-2i\beta_2} + (r_{12} + r_{23}e^{-2i\beta_2}) r_{01}e^{-2i\beta_1}}. \quad (4.12)$$

where r_{ij} and t_{ij} is the reflection and transmission coefficient from medium i to j . In the calculation of the enhancement factor, we use the refractive index obtained from the first-principles calculation which is shown in Table 4.2. Figs. 4-8 (b)-(d) are the GaTe thickness dependence of the calculated enhancement factor. As seen in Figs. 4-8 (b), which shows the calculated ratio of the enhancement factors in the x - and y -directions for the Raman intensity, the interference effect suppresses the Raman intensity in the x -direction compared with that in the y -direction for both excitation wavelengths 532 and 633 nm, and almost the same intensity in the x and y -directions for the wavelength 785 nm. These differ from the experimental observations, suggesting that the anisotropy of the Raman intensity cannot be mainly attributed to the interference effect, but is mostly due to the anisotropy of the light-matter interactions.

4.2 Black phosphorus

Black phosphorus is (BP) the atomic layer material of phosphorus. BP is attracted interests by its high mobility while it is easy to be oxidized in the air which is the difficulty to synthesize for the application. BP is known as the atomic layer material to show the strong in-plane anisotropy in optical property (see Sec. 1.3.1 and 1.3.3). In this section, we discuss the anisotropy of optical absorption and Raman spectra of BP by the same analysis as GaTe.

4.2.1 Crystal structure of black phosphorus

In Fig. 4-9, we show the crystal structure of BP which belongs to D_{2h}^7 space group. There are 4 phosphorus atoms in the unit cell which also has three dimensional structure. The each layer is attracted by van der Waals force which constructs the atomic

Fig. 4-9: fig/ch4-structure-bp.eps

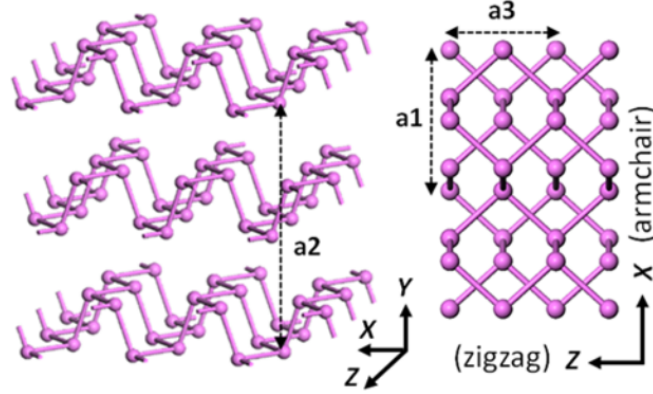


Figure 4-9: Crystal structure of BP: (a) side view and (b) top view.⁷¹⁾ a_1 , a_2 , and a_3 are the primitive lattice vectors of BP.

layer. We adopt the conventional notation of the label of x , y , z coordinates: x (z) axis is in-plane armchair (zigzag) direction of BP. The direct energy band gap of BP is at the Γ point with 0.3-1.5 eV which strongly depends on the number of layers where the electronic energy bands are shown in Fig. 4-11.

4.2.2 Optical absorption of black phosphorus

In Fig. 4-10, we show the absorption spectra given by the (a) first-principles calculation and (b) experiment.⁷¹⁾ BP shows the strong in-plane anisotropy of optical absorption that the absorption for the polarization along the armchair direction is stronger than that along the zigzag direction as shown in Fig. 4-10 (b). This result is in good agreement with the theoretical calculation and the experiment each other. This anisotropic optical absorption is understood by considering the electron-photon matrix elements in BP. In Fig.4-11, we show the band symmetry with D_{2h}^7 of the space group for monolayer, bilayer, trilayer, and bulk BP. The optical selection rule of optical transition is given by the group theory. In Fig. 4-12, we show the optical selection rule of trilayer BP. As shown in Fig. 4-12, the electron-photon matrix element for small E_L is large for x - (90°) polarization while the z - (0°) polarized matrix element appears in larger E_L . The difference from the GaTe is that BP has a valley structure in electronic energy band at the Γ point and thus the optical transition for low E_L occurs only around the Γ point. This means that the x -polarized electron-photon matrix element near the Γ point can only contribute to the optical absorption for low E_L . Such a situation of electronic energy band structure appears also in monolayer, bilayer, and

Fig. 4-10: fig/ch4-absorption-bp.eps

Fig. 4-11: fig/ch4-symmetry-bp.eps

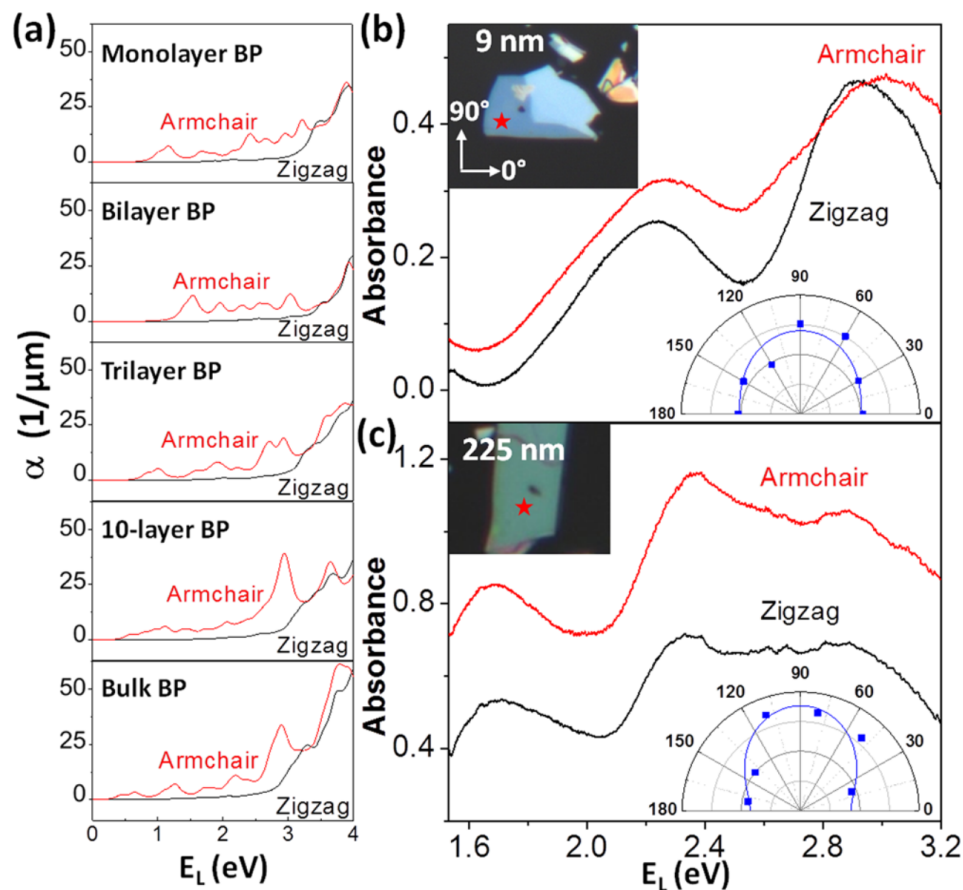


Figure 4-10: Anisotropic absorption of BP flakes with different thicknesses.⁷¹⁾ (a) Calculated absorption coefficient α as a function of laser energy for monolayer, bilayer, trilayer, 10-layer, and bulk BP. (b)-(c) Typical absorbance spectra of (b) a thin and (c) a thick BP flake with incident light polarization along the armchair and zigzag directions. Insets: optical images and corresponding polar plots of the absorbance at 633 nm ($E_L = 1.96$ eV) versus the sample rotation angle in a plane normal to the flake. The symbols are the experimental values, and the lines are least-squares fittings. The red stars in the insets label the sample measurement positions. 0° and 90° corresponds to the zigzag and armchair directions, respectively.

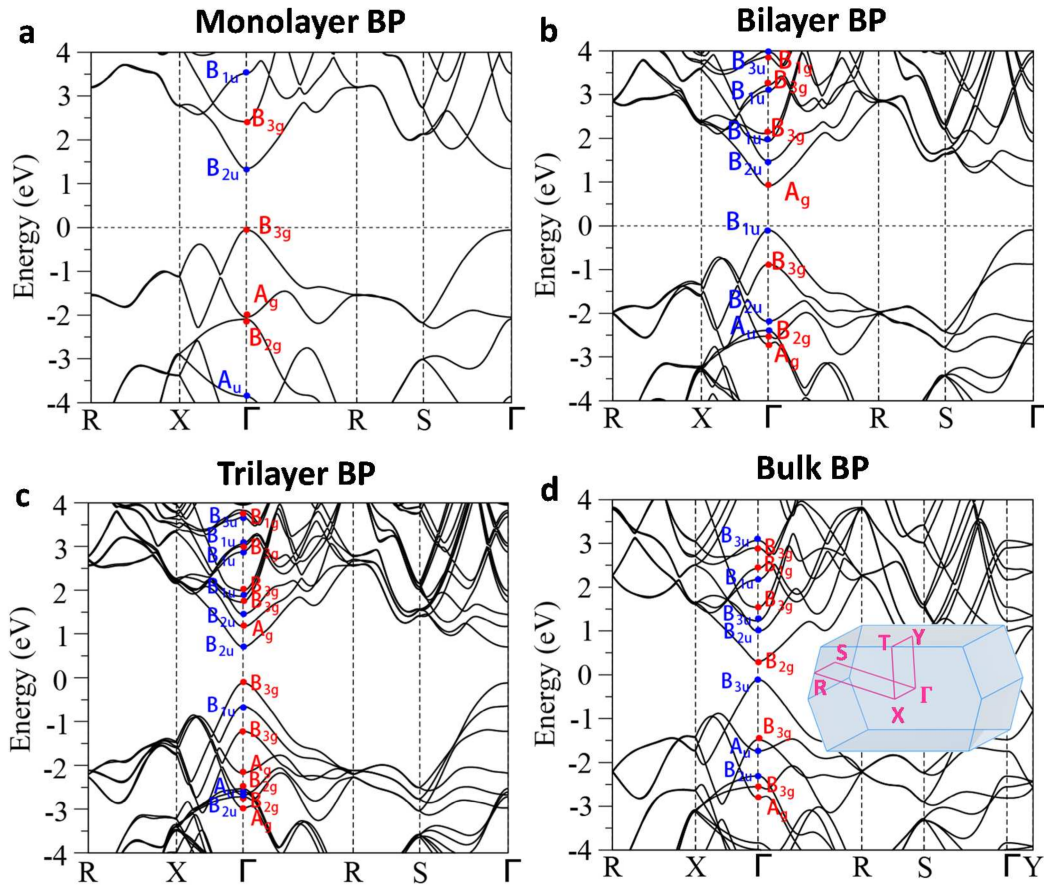


Figure 4-11: Band structures and band symmetry of BP with different number of layer.⁷¹⁾ (a) monolayer BP; (b) bilayer BP; (c) trilayer BP; (d) bulk BP. Red (blue) labels of irreducible representation correspond to symmetric (anti-symmetric) states under inversion symmetry. Inset of (d): Brillouin zone of bulk BP with high symmetry points labeled. The coordinates of high symmetry points in the Brillouin zone in (a)-(c) are labeled in the inset of Fig. 4-12.

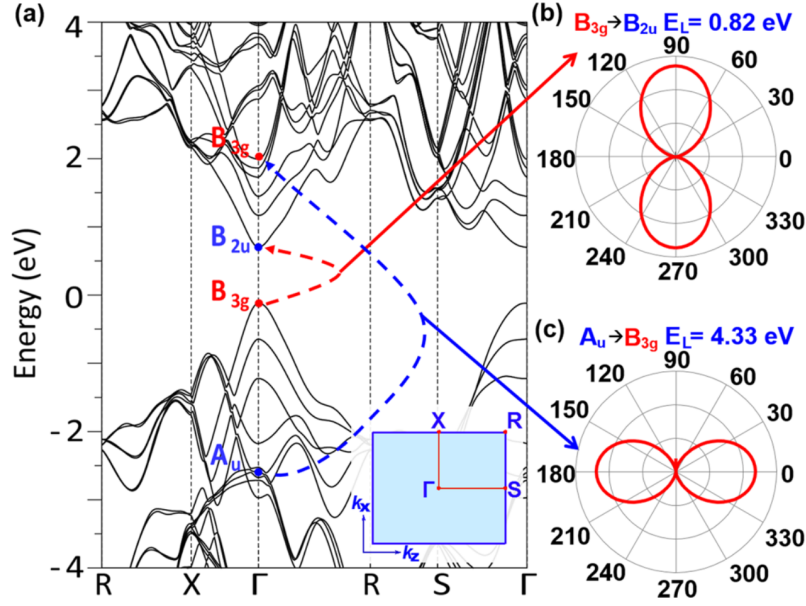


Figure 4-12: Optical selection rules in black phosphorus and the calculated anisotropic absorption.⁷¹⁾ (a) Calculated electronic band structure $E(k)$ of trilayer BP. B_{3g} bands are indicated by red labels, while B_{2u} and A_u bands are indicated by blue labels at the Γ point. Inset: 2D Brillouin zone of trilayer BP. (b)-(c) Calculated polarization dependence of the optical transition probability (b) from B_{3g} to B_{2u} and (c) from A_u to B_{3g} as indicated in panel (a). Here, 0° (90°) corresponds to the zigzag (armchair) direction of BP.

bulk BP and becomes the origin of the strong anisotropy of BP.

4.2.3 Raman spectra of black phosphorus

In BP, we can observe the three typical Raman peak: A_g^1 , B_{2g} , and A_g^1 at around 361, 438, and 466 cm^{-1} , respectively. The selection rule of polarized Raman intensity is given by the group theory which is already discussed in GaTe (Sec. 1.2.2), but for D_{2h}^7 symmetry as shown in Table 4.5 and 4.6. The B_{2g} Raman intensity has the main axis of polar plot for Raman intensity in 45° , 135° , and 225° , 315° direction whose shape does not depend on the thickness and laser excitation energy. The change of the main axis in the polar plots of the Raman intensity can be found in the A_g Raman peaks as shown in Fig. 4-13. Thickness dependence of BP is also discussed by calculating the enhancement factor of Raman intensity in Eqs. (4.10). We consider the experimental set up as same with Fig. 4-8. As shown in Fig. 4-14, for the three laser lines we used, the interference enhancement is stronger when the incident polarization is along the

Fig. 4-12: fig/ch4-selection-rule-bp.eps

Fig. 4-13: fig/ch4-aniso-raman-bp.eps

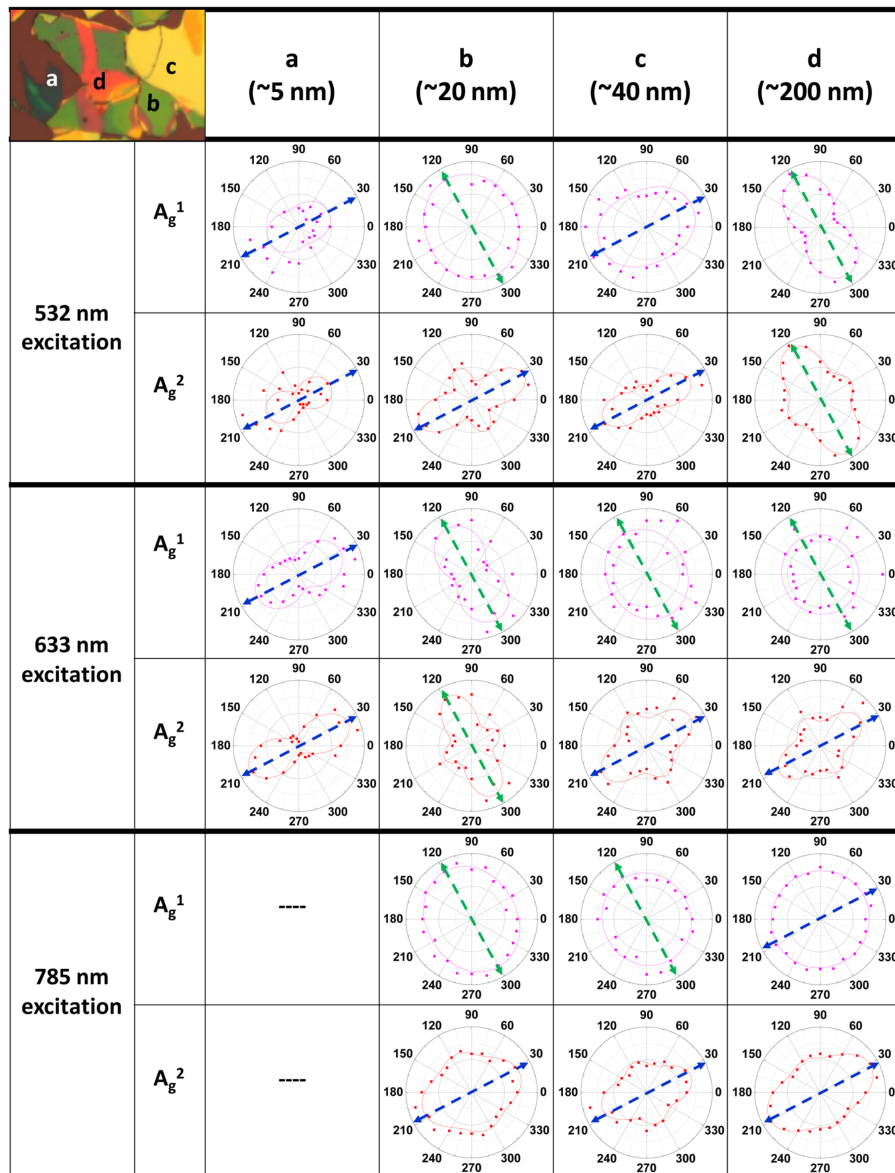


Figure 4-13: Four typical categories of the BP flakes with the anisotropic Raman scattering under different incident laser wave lengths.⁷¹⁾ The blue and green arrows indicate the main axes of the polar plots. The data for the 5 nm flake under 785 nm laser excitation is not included in the figure because of the weak Raman signal.

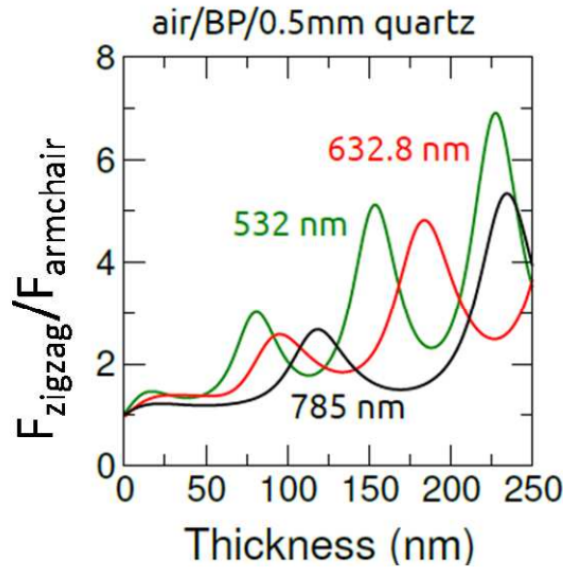


Figure 4-14: Calculated ratio of interference enhancement factor for zigzag to armchair as a function of the thickness of the sample for different E_L (in nm) for air/BP/0.5-mm-quartz⁷¹⁾

zigzag direction. The ratio of the enhancement factors between the zigzag and the armchair directions varies significantly with the thickness of BP, which in turn can influence the thickness dependence of Raman intensity ratio between the directions of zigzag and the armchair. The ratio of enhancement factor for zigzag and armchair direction is oscillating, which depends on the BP thickness while the value of ratio is always larger than unity for any E_L , which means that the Raman intensity for zigzag direction is always more enhanced than that of the armchair direction. As discussed in Fig. 4-12, the electron-photon matrix elements of BP is x -polarized for small E_L , however, the anisotropy of A_g Raman intensity in Fig. 4-13 is not so large even for low excitation energy (785 nm). This fact indicates that the anisotropy of Raman intensity in BP becomes simpler by the enhancement factor.

Table 4.5: Selection rules of Raman scattering for the A_g mode in D_{2h}^7 symmetry. $|i\rangle$, $|m\rangle$ and $|m'\rangle$ are the initial state and two intermediate states, respectively. xx (yy) are polarization vectors for the incident and scattered light which are parallel to each other. These selection rules correspond to the product of the matrix elements: $\langle f|H_{\text{opt}}^x|m'\rangle\langle m'|H_{\text{ep}}(A_g)|m'\rangle\langle m|H_{\text{opt}}^x|i\rangle$ and $\langle f|H_{\text{opt}}^x|m'\rangle\langle m'|H_{\text{ep}}(A_g)|m'\rangle\langle m|H_{\text{opt}}^y|i\rangle$.

xx		yy	
$ i\rangle = f\rangle$	$ m\rangle = m'\rangle$	$ i\rangle = f\rangle$	$ m\rangle = m'\rangle$
A_g	B_{1u}	A_g	B_{3u}
B_{1g}	A_u	B_{1g}	B_{2u}
B_{2g}	B_{3u}	B_{2g}	B_{1u}
B_{3g}	B_{2u}	B_{3g}	A_u
A_u	B_{1g}	A_u	B_{3g}
B_{1u}	A_g	B_{1u}	B_{2g}
B_{2u}	B_{3g}	B_{2u}	B_{1g}
B_{3u}	B_{2g}	B_{3u}	A_g

Table 4.6: Selection rules of Raman scattering for the B_{2g} phonon in D_{2h}^7 symmetry. The polarization is different for the incident and scattered light for the B_{2g} mode. xy means that the incident light is y -polarized, and the scattered light is x -polarized. These selection rules correspond to the product of the matrix elements $\langle f|H_{\text{opt}}^x|m'\rangle\langle m'|H_{\text{ep}}(B_{2g})|m'\rangle\langle m|H_{\text{opt}}^y|i\rangle$ and $\langle f|H_{\text{opt}}^y|m'\rangle\langle m'|H_{\text{ep}}(B_{2g})|m'\rangle\langle m|H_{\text{opt}}^x|i\rangle$.

xy			yx		
$ i\rangle = f\rangle$	$ m\rangle$	$ m'\rangle$	$ i\rangle = f\rangle$	$ m\rangle$	$ m'\rangle$
A_g	B_{1u}	B_{3u}	A_g	B_{3u}	B_{1u}
B_{1g}	A_u	B_{2u}	B_{1g}	B_{2u}	A_u
B_{2g}	B_{3u}	B_{1u}	B_{2g}	B_{1u}	B_{3u}
B_{3g}	B_{2u}	A_u	B_{3g}	A_u	B_{2u}
A_u	B_{1g}	B_{3g}	A_u	B_{3g}	B_{1g}
B_{1u}	A_g	B_{2g}	B_{1u}	B_{2g}	A_g
B_{2u}	B_{3g}	B_{1g}	B_{2u}	B_{1g}	B_{3g}
B_{3u}	B_{2g}	A_g	B_{3u}	A_g	B_{2g}

Chapter 5

Helicity exchange in the first-order Raman scattering for graphene and TMDs

In this chapter, we discuss the helicity exchange of photon in the first-order Raman scattering for graphene and TMDs. In TMDs, there are two strong Raman peaks that are called the IMC and OC modes.^{97,100–104)} Chen *et al.* observed the helicity exchange of scattered light only in the IMC mode.²⁶⁾ We develop the program to calculate the first-order Raman spectra by using first-principles calculation in which the effect of helicity exchange is taken into account.

In Sec. 5.1, we show calculated results of first-order Raman spectra for TMD to explain the experimental results by Chen *et al.*²⁶⁾ as shown in Fig. 1-11. We also show the calculated result of the G band in graphene that is found to be also helicity-exchanged. In Sec. 5.2, we discuss the selection rule of Raman scattering for circular polarized light by considering the symmetry of the matrix elements. In Sec. 5.3, we further discuss the symmetry of the matrix elements by group theory. In Sec. 5.5, we show the calculated results of strain-induced graphene and discuss how the helicity changes in the Raman scattering.

5.1 Helicity-resolved Raman spectra

5.1.1 Electronic and phonon structure of graphene and TMDs

In Figs. 5-1(a)-(c), we show the electronic energy bands of graphene, monolayer, and bilayer MoS₂. The electronic energy bands in Figs. 5-1(a)-(c) are given by the Wannier functions which are obtained from the plane wave DFT-SCF calculation, by using

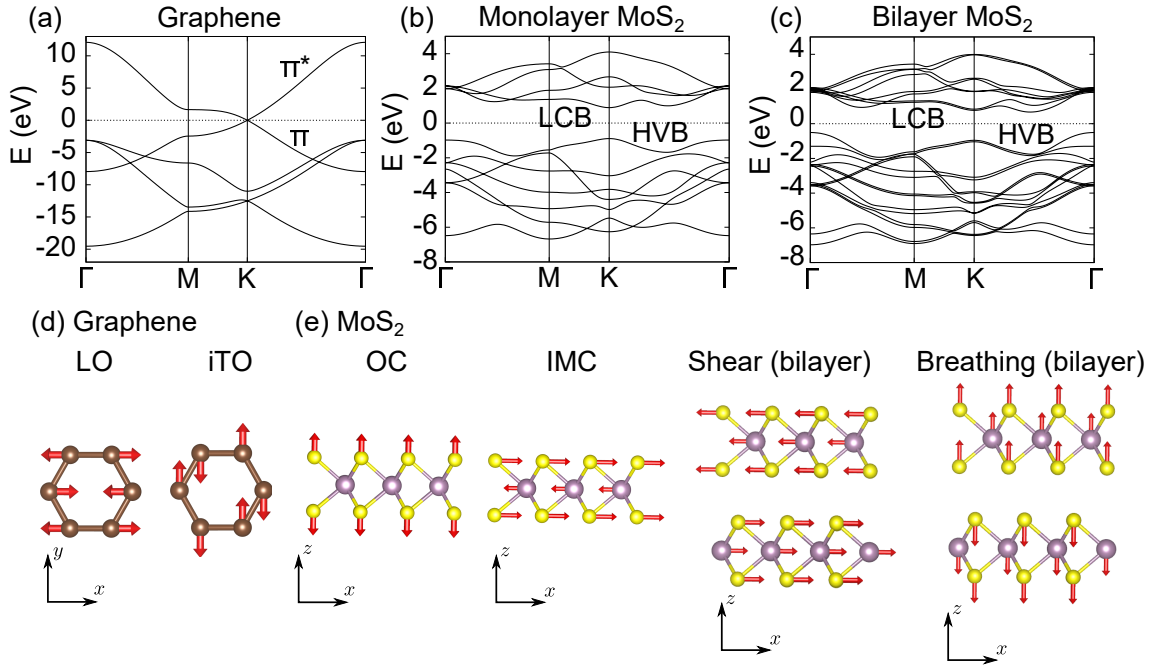


Figure 5-1: (a)-(c) Electronic energy bands of (a) graphene, (b) monolayer, and (c) bilayer MoS_2 . (d)-(e) Atomic vibrations of (d) iTO and LO modes in graphene, (e) OC, IMC, shear, and breathing modes in MoS_2 . Shear and breathing modes are observed only in multilayer MoS_2 .

Wannier 90 package.¹⁰⁵) In the calculation by Wannier90, we select two π and three sp^2 orbitals for graphene, and $3s$ orbitals of sulfur and $4d$ orbitals of molybdenum for MoS_2 as Wannier orbitals.

In this thesis, we focus on the first-order (one phonon) Raman process, in which only $\mathbf{q} = 0$ phonon is emitted. Thus, we calculate the energy of $\mathbf{q} = 0$ phonon for graphene, monolayer, and bilayer MoS_2 in Table 5.1. In graphene, Raman active E_{2g} mode that corresponds to the G band is doubly-degenerate, in-plane vibrating mode [see Fig. 5-1(d)] at around the 1585 cm^{-1} in graphene. In MoS_2 , there are two Raman active phonon modes at around 389 and 407 cm^{-1} for monolayer MoS_2 , which are denoted by IMC and OC Raman peaks, respectively.^{97,100-104}) The IMC mode is the in-plane vibration of the transition metal and chalcogen atoms, while the OC mode is the out-of-plane vibration of chalcogen atoms [see Fig. 5-1(e)]. In bilayer MoS_2 , there are interlayer vibrating modes [see Fig. 5-1(e)] which is called the shear mode (C band) and layer breathing mode (LBM) with small energy values (~ 20 and 30 cm^{-1} , respectively).^{26,106}) These interlayer modes are also Raman active modes.

Table 5.1: Calculated phonon modes and frequency ω_{ph} in units of cm^{-1} at the Γ point for graphene, monolayer (1L), and bilayer (2L) MoS_2 . IR/R denotes infrared active or Raman active modes.

	Mode	ω_{ph} (cm^{-1})	IR/R
Graphene	A_{2u}	0	IR
	E_{1u}	0	IR
	B_{1g}	905.7	
	E_{2g} (iTO + LO)	1618.8	R
1L MoS_2	A_2''	0	IR
	E'	0	R
	E''	287.4	R
	E' (IMC)	388.5	IR+R
	A_1' (OC)	407.3	R
	E_2''	472.3	IR
2L MoS_2	A_{2u}	0	IR
	E_u	0	IR
	E_g (Shear)	21.9	R
	A_{1g} (Breathing)	30.4	R
	E_u	286.7	IR
	E_g	288.7	R
	E_u	388.3	IR
	E_g (IMC)	388.9	R
	A_{2u}	406.6	IR
	A_{1g} (OC)	408.0	R
	A_{2u}	471.0	IR
	A_{1g}	472.6	R

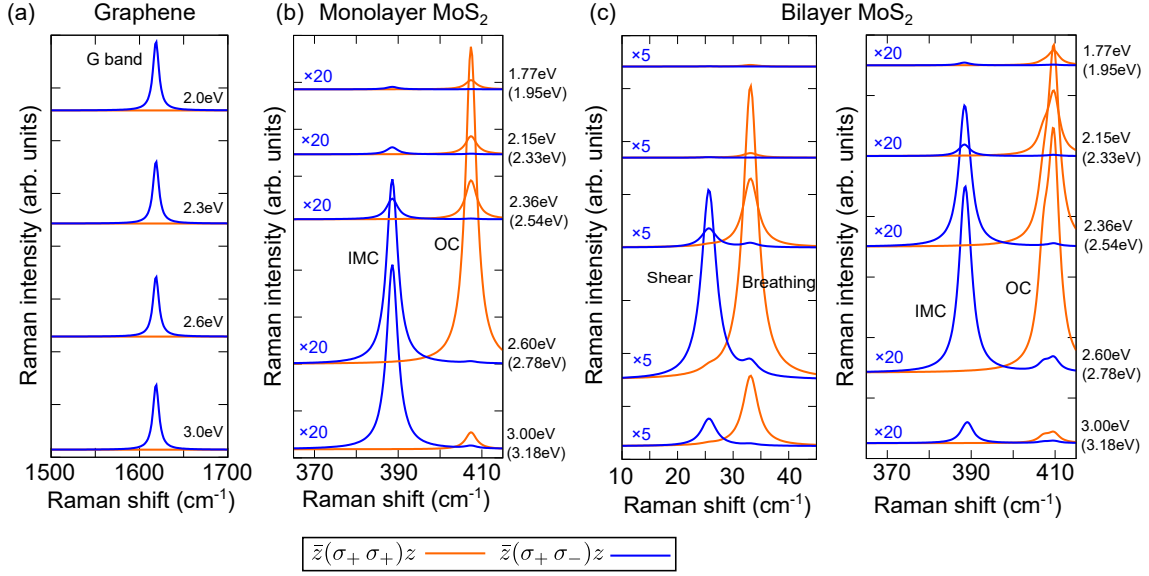


Figure 5-2: Calculated helicity-dependent Raman spectra of (a) the G band in graphene, (b) the IMC (E') and OC (A'_1) modes in monolayer MoS_2 , and (c) IMC, OC, shear, and breathing modes in bilayer MoS_2 . We show the spectra for the incident laser energies: $E_L = 2.0, 2.3, 2.6,$ and 3.0 eV for graphene and $E_L = 1.77, 2.15, 2.36, 2.60,$ and 3.00 eV for MoS_2 . The value of energy in bracket is the corresponding energy by shifting the conduction band to match with the experimental energy gap of monolayer MoS_2 : 1.83 eV.²⁷⁾

5.1.2 Helicity-resolved Raman spectra of graphene and MoS_2

In Fig. 5-2, we show the calculated Raman spectra of (a) the G band of graphene and (b) the IMC and OC modes of monolayer and bilayer MoS_2 in the case of same helicity [$\bar{z}(\sigma_+ \sigma_+)z$, orange line] and different [$\bar{z}(\sigma_+ \sigma_-)z$, blue line] helicity of photon for the incident and scattered light, calculated by using Eq. (2.89). Here the symbol $\bar{z}(\sigma_+ \sigma_+)z$ denotes (1) the incident light propagating in the direction of z with circular polarized light σ_+ and (2) the scattered light in the direction of $-z$ (or \bar{z}) with σ_+ . As shown in Fig. 5-2, the G band in graphene and the IMC peak in monolayer MoS_2 show non-zero (zero) Raman intensity for $\bar{z}(\sigma_+ \sigma_-)z$ [$\bar{z}(\sigma_+ \sigma_+)z$] scattering while the OC peak shows non-zero (zero) Raman intensity for $\bar{z}(\sigma_+ \sigma_+)z$ [$\bar{z}(\sigma_+ \sigma_-)z$] scattering. It means that the G band and the IMC mode exhibit the helicity exchange while the OC mode does not, which is consistent with the experimental results by Chen *et al.*²⁶⁾ and Raman tensor analysis discussed in Sec. 1.3.3. This result is also consistent with the conservation of angular momentum which implies that the doubly-degenerate phonon mode (E') can change the helicity of circular polarized light.

In Fig. 5-2(b), we show the E_L dependence of Raman spectra in monolayer MoS_2 ,

too. The resonant Raman spectra of monolayer MoS₂ strongly depends on the E_L . In the case of the E_L around the energy gap ($E_L \sim 1.65$ eV by the DFT calculation) at the K (K') point, the Raman intensity of the IMC mode is relatively small since the optical transition of absorption and emission in the first-order Raman process occurs within the same valley, in which only σ_+ (σ_-) light can be absorbed or scattered at the K (K') valley. It means that even though the IMC mode can change the helicity of light, the scattered photon with the opposite helicity is forbidden within the same valley, which is the reason why the intensity of IMC is small. Thus, the intensity of the helicity exchange Raman scattering around the K (K') valley is small for the structure without inversion symmetry that has the valley-selective optical absorption by circular polarized light, as discussed in Chapter 3.

In the case of $E_L = 2.60$ eV, which corresponds to the gap energy around the so-called Λ valley between Γ and K (K') points, the Raman spectra are enhanced for both the IMC and OC modes. This behavior appears because of the enhancement of optical absorption due to the large joint density of states around the Λ valley by the nesting of the energy bands^{62,63,107}) that is discussed in Sec. 3.2.3. When we further increase the E_L to the gap energy at around the M point ($E_L \sim 3.0$ eV), intensity of the IMC peak becomes strong due to the 2D van Hove singularity (see Sec. 3.2.3), since both the σ_+ and σ_- light can excite the electrons at the K and K' points. In the experiments, however, the IMC and OC peaks do not much depend on E_L and the peak intensities are almost comparable¹⁰²⁻¹⁰⁴). One possible reason is that the contribution of the higher-order Raman processes for the IMC mode might exist by the intervalley scattering of the photo-excited electron from K to K' (or K' to K) by defects, which is not considered in our calculation. The intensity of the IMC mode might be enhanced by the higher order process like that the electron in the K valley is excited and scattered to the K' valley by the defect, and finally emit the photon in the K' valley by changing the helicity. Furthermore, a recent study reported that the inclusion of many body effects (or exciton effects) by GW-BSE calculation influences the ratio of Raman intensity for IMC and OC modes in MoTe₂.¹⁰⁸) The GW-BSE calculation makes the Raman intensity of IMC and OC mode more comparable to the experimental results.¹⁰⁸) In order to reproduce the experiment, we also have to evaluate correctly the broadening factor γ in Eq. (2.89). In our calculation, we assume that γ is constant. However, the life time of photo-excited electron for the IMC mode which changes the helicity would become longer than the OC mode because of the helicity-selective optical transition. In order to evaluate γ , we have to calculate the electron-phonon interaction for all q phonon which would be the future work. For the bilayer MoS₂, we can observe the interlayer vibration which is called the shear

mode (C band) and breathing mode (LBM) which are shown in Fig. 5-1(e). From the numerical calculation shown in Fig. 5-2(c), helicity exchange for the Raman scattering is also observed in the shear mode which is doubly-degenerate, while the breathing mode without degeneracy does not change the helicity of photon. This result is also in good agreement with the experiment by Chen *et al.*²⁶⁾, too.

5.2 Raman matrix element

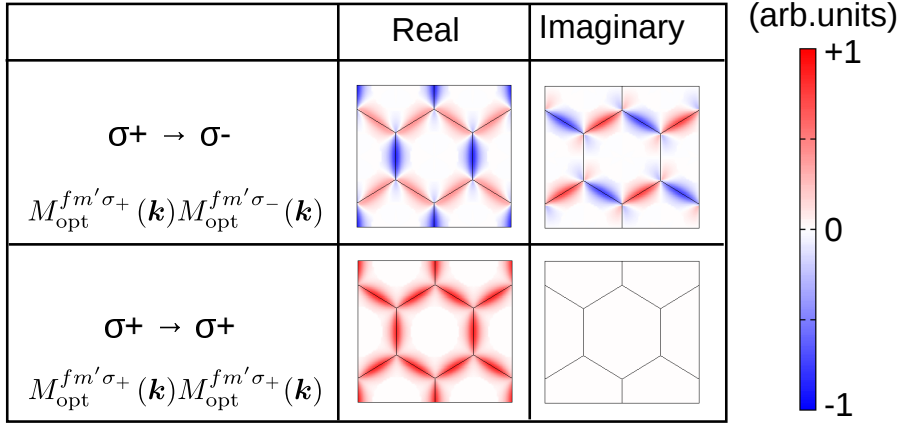
In this section, We discuss the reason why the G band of graphene and the IMC mode in monolayer MoS₂ exchange the helicity of light by Raman scattering. For this purpose, we consider the symmetry of the Raman matrix element $\mathcal{M}_R(\mathbf{k})$, which is the numerator of Eq. (2.89),

$$\mathcal{M}_R(\mathbf{k}) = M_{\text{opt}}^{fm'\sigma'}(\mathbf{k})M_{\text{ep}}^{m'\nu}(\mathbf{k})M_{\text{opt}}^{mi\sigma}(\mathbf{k}). \quad (5.1)$$

In the resonant scattering, the intermediate (or virtual) state [m or m' in Eq. (5.1)] is given by the linear combination of the eigen states. The contribution of the eigen states to the virtual state is large if the energy of an eigen state is close to the virtual state. Since the energy of the phonon (~ 0.2 eV for G band and ~ 0.05 eV for IMC and OC mode) is small compared with the separation of the electronic energy bands, we can take $m = m'$ in Eq. (5.1) for the first-order Raman process. It means that we approximate the virtual states after scattering to the states before the scattering. In Fig. 5-3(a), we show the product of the two electron-photon matrix elements with the helicity switching [$M_{\text{opt}}^{fm'\sigma_+}(\mathbf{k})M_{\text{opt}}^{mi\sigma_-}(\mathbf{k})$] for the case of $i = f = \text{HVB}$ (the highest valence band) and $m = m' = \text{LCB}$ (lowest conduction band). Since the dipole vector $\mathbf{D}^{mi(fm')}(\mathbf{k})$ in electron-photon matrix element [Eq. (2.39)] can be expressed only by the real number for graphene,⁷⁸⁾ we get the relation of $M_{\text{opt}}^{fm'\sigma_+}(\mathbf{k}) = M_{\text{opt}}^{mi\sigma_-}(\mathbf{k})$. In fact, $M_{\text{opt}}^{fm'\sigma_+}(\mathbf{k})M_{\text{opt}}^{mi\sigma_-}(\mathbf{k})$ for graphene shown in Fig. 5-3(a) has both the real and imaginary parts, while $M_{\text{opt}}^{fm'\sigma_+}(\mathbf{k})M_{\text{opt}}^{mi\sigma_+}(\mathbf{k})$ in Fig. 5-3(a) is a real number. In Fig. 5-3(b), we plot the electron-phonon matrix elements [$M_{\text{ep}}^{m'\nu}(\mathbf{k})$] for the iTO and LO Γ point phonons of graphene in the case of $m = m' = \text{LCB}$. Note that the electron-phonon matrix element for $m = m'$ has only the real part since the deformation potential in Eq. (2.72) is a real number. The iTO and LO modes in graphene belong to the E_{2g} (Γ_6^+) symmetry of D_{6h} with the basis of xy and $x^2 - y^2$, respectively. The character table of D_{6h} is given in Appendix C. Then, as shown in Fig. 5-3 (b), the real (imaginary) part of $\mathcal{M}_R(\mathbf{k})$ for the iTO (LO) mode of $\bar{z}(\sigma_+ \sigma_-)z$ has a finite value after the integration

Fig. 5-3: fig/ch5-raman-matele-graphene.eps

(a) Electron-photon matrix elements



(b) Electron-phonon and Raman matrix elements

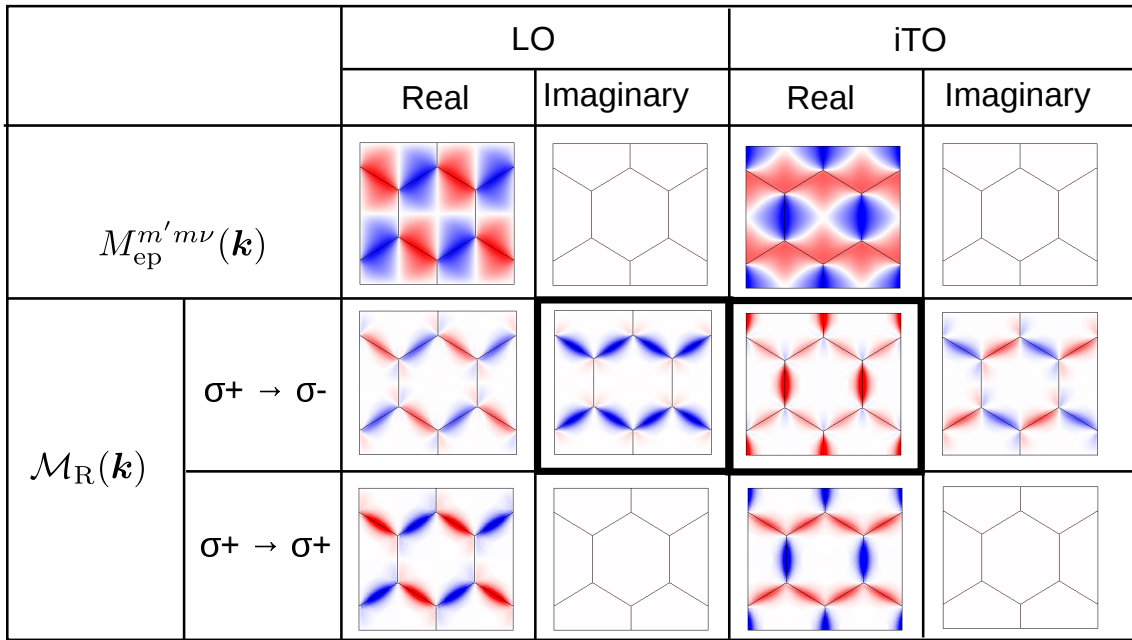


Figure 5-3: (a) The real and imaginary parts of the electron-photon matrix element in graphene of incident and scattered light for $\bar{z}(\sigma_- \sigma_+)z$ and $\bar{z}(\sigma_+ \sigma_+)z$. (b) The real and imaginary parts of the electron-phonon matrix and Raman matrix elements for the LO and iTO modes of graphene. The red and blue areas denote positive and negative values, respectively. The $\mathcal{M}_{\text{R}}(\mathbf{k})$ which survive after the integration in BZ are shown in bold black box.

in the first Brillouin zone, while the imaginary (real) part of $\mathcal{M}_R(\mathbf{k})$ for the iTO (LO) mode vanishes after the integration because of the presence of an odd function in the k space.¹⁰⁸⁾ The Raman matrix element for $\bar{z}(\sigma_+ \sigma_+)z$ vanishes for both the LO and iTO modes [see Fig. 5-3(b)] by the integration in the first Brillouin zone. Thus, only the $\bar{z}(\sigma_- \sigma_+)z$ scattering can be observed for the G band of graphene.

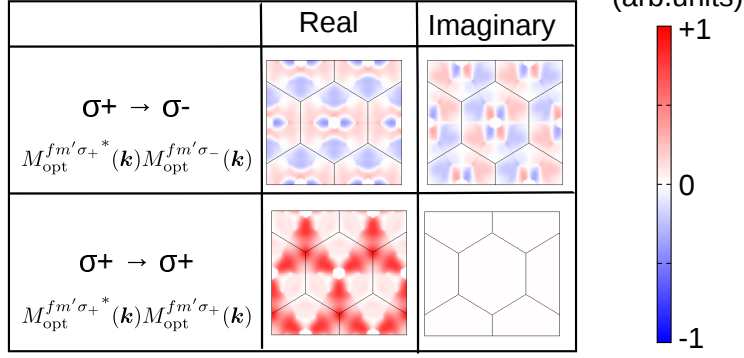
We also discuss the symmetry of the matrix elements for monolayer MoS₂ as shown in Fig. 5-4. The matrix elements displayed are for $i = f = \text{HVB}$ and $m = m' = \text{LCB}$ in Eq. (5.1). The electron-phonon matrix elements for the IMC mode have same symmetries with the LO and iTO modes of graphene and we can do the same discussion with the G band of graphene. Since the K and the K' points are inequivalent for the optical transition in MoS₂ for circular polarized light, the inequivalent electron-photon matrix elements for MoS₂ appear as shown in Fig. 5-4. Finally, only the imaginary part of the IMC (LO) mode and the real part of the IMC (TO) mode have the finite value by the integration in the first Brillouin zone for $\bar{z}(\sigma_- \sigma_+)z$ scattering. On the other hand, only the real part of the OC mode has the finite value by the integration in the first Brillouin zone for $\bar{z}(\sigma_+ \sigma_+)z$ scattering. Group theory discussion in Sec. 5.4 confirms which matrix elements have the finite value after the integration in the first Brillouin zone.

5.3 Discussion by group theory

The selection rule of the helicity switching can be discussed by the symmetry of the matrix elements with use of the group theory. The symmetry of graphene (monolayer MoS₂) belongs to D_{6h} (D_{3h}) point group. We show the symmetry of the matrix elements for graphene and monolayer MoS₂ in Table 5.2. The polarization vectors belong to the irreducible representation Γ_5^- (Γ_6) for D_{6h} (D_{3h}), which has two basis functions denoted by $|5, 1\rangle^-$ and $|5, 2\rangle^-$ ($|6, 1\rangle^-$ and $|6, 2\rangle^-$). The two basis functions correspond to the left- and right-handed circular polarization. In order to discuss the selection rule for \mathcal{M}_R , we need to consider not only the direct product of the irreducible representation, but also the product of the basis functions. The product tables of D_{3h} and D_{6h} are shown in Appendix C. We derive the shape of the dipole vector of TMDs near the K and K' point in Chapter 3. The shape of the dipole vectors for $\pi - \pi^*$ transition in graphene and HVB-LCB transition around the K (K') point in monolayer MoS₂ are given in Figs. 3-2(c)-(d) and (a)-(b), respectively, and we obtain the symmetry of dipole vectors as Γ_4^- for graphene and $\Gamma_1 + \Gamma_2$ for monolayer MoS₂. Only the \mathcal{M}_R that belongs to Γ_1^+ ($|1, 1\rangle^+$) or Γ_1 ($|1, 1\rangle$) symmetry has the finite value after the integration in the

Fig. 5-4: fig/ch5-raman-matele-tmd.eps

(a) Electron-photon matrix element



(b) Electron-photon and Raman matrix element

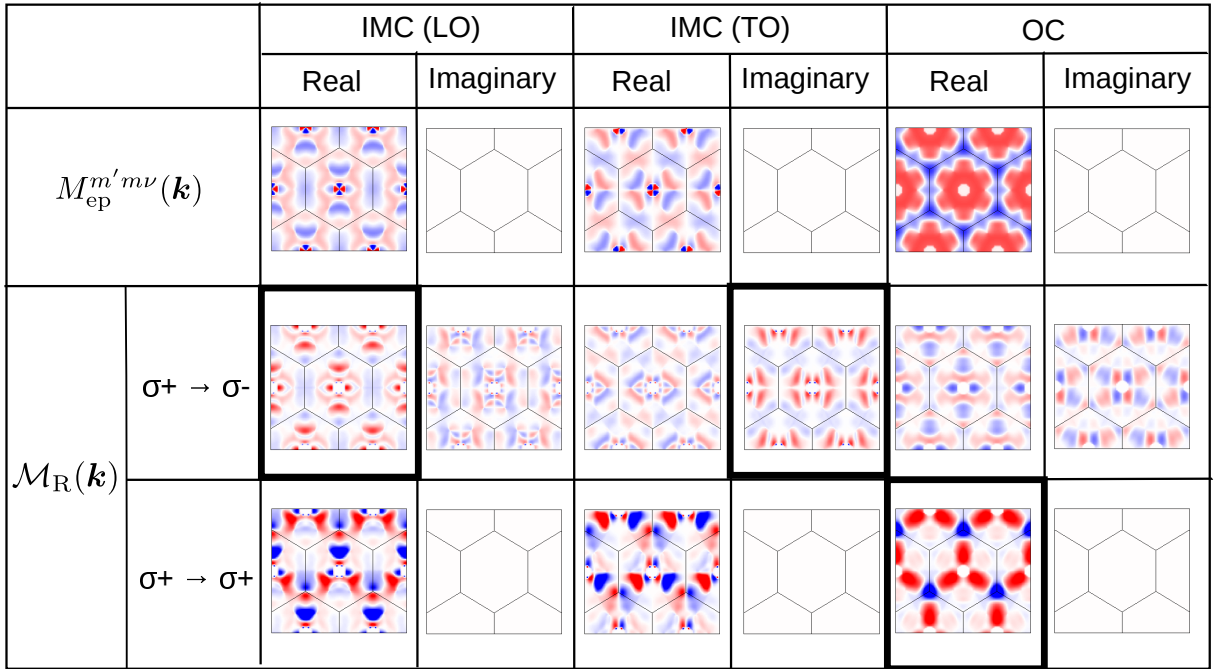


Figure 5-4: (a) The real and imaginary parts of the electron-photon matrix elements in monolayer MoS₂ of incident and scattered light for $\bar{z}(\sigma_- \sigma_+)z$ and $\bar{z}(\sigma_+ \sigma_+)z$. (b) The real and imaginary parts of the electron-phonon and Raman matrix elements for the IMC and OC modes of monolayer MoS₂. The red and blue areas denote positive and negative values, respectively. The $\mathcal{M}_{\text{R}}(\mathbf{k})$ which survives after the integration in BZ are shown in bold black box.

Table 5.2: The symmetry of the matrix elements for graphene (D_{6h}) and monolayer MoS₂ (D_{3h}). We assume $i = f = \pi$ band (HVB) and $m = \pi^*$ band (LCB) for graphene (monolayer MoS₂). The $|p, q\rangle^\pm$ is the q -th basis of the Γ_p^\pm symmetry.

		$M_{\text{opt}}^{fm\sigma}$	$M_{\text{ep}}^{mm\nu}$	$M_{\text{opt}}^{mi\sigma}$		\mathcal{M}_R	
	P	D		D	P		
Graphene, D_{6h} (G band)	$\bar{z}(\sigma_+ \sigma_+)z$	$ 5, 1\rangle^-$	$ 4, 1\rangle^-$	$(6, 1\rangle^+ + 6, 2\rangle^+)$	$ 4, 1\rangle^-$	$ 5, 2\rangle^-$	$(6, 1\rangle^+ + 6, 2\rangle^+)$
	$\bar{z}(\sigma_+ \sigma_-)z$	$ 5, 1\rangle^-$	$ 4, 1\rangle^-$	$(6, 1\rangle^+ + 6, 2\rangle^+)$	$ 4, 1\rangle^-$	$ 5, 1\rangle^-$	$(1, 1\rangle^+ + 2, 1\rangle^+ + 6, 1\rangle^+ + 6, 2\rangle^+)$
1L MoS ₂ , D_{3h} (IMC mode)	$\bar{z}(\sigma_+ \sigma_+)z$	$ 6, 1\rangle$	$(1, 1\rangle + 2, 1\rangle)$	$(6, 1\rangle + 6, 2\rangle)$	$(1, 1\rangle + 2, 1\rangle)$	$ 6, 2\rangle$	$(6, 1\rangle + 6, 2\rangle)$
	$\bar{z}(\sigma_+ \sigma_-)z$	$ 6, 1\rangle$	$(1, 1\rangle + 2, 1\rangle)$	$(6, 1\rangle + 6, 2\rangle)$	$(1, 1\rangle + 2, 1\rangle)$	$ 6, 1\rangle$	$(1, 1\rangle + 2, 1\rangle + 6, 1\rangle + 6, 2\rangle)$
1L MoS ₂ , D_{3h} (OC mode)	$\bar{z}(\sigma_+ \sigma_+)z$	$ 6, 1\rangle$	$(1, 1\rangle + 2, 1\rangle)$	$ 1, 1\rangle$	$(1, 1\rangle + 2, 1\rangle)$	$ 6, 2\rangle$	$(1, 1\rangle + 2, 1\rangle)$
	$\bar{z}(\sigma_+ \sigma_-)z$	$ 6, 1\rangle$	$(1, 1\rangle + 2, 1\rangle)$	$ 1, 1\rangle$	$(1, 1\rangle + 2, 1\rangle)$	$ 6, 1\rangle$	$ 6, 2\rangle$

Brillouin zone because Γ_1^+ and Γ_1 do not change the sign by any symmetry operations. Therefore, $\bar{z}(\sigma_+ \sigma_-)z$ for the G band and the IMC mode and $\bar{z}(\sigma_+ \sigma_+)z$ for the OC mode can be observed in the Raman spectra as is listed in the rightmost column in Table 5.2

5.4 Raman spectra in strain-induced graphene

According to the discussion of chiral phonon with the angular momentum,^{75,109)} the G band in graphene can switch the helicity of the photon in the Raman process since the two modes (iTO and LO) are degenerate. Then, the helicity selection rule would change if the degeneracy of the G band is lifted by applying the strain in the direction of the y axis. Experimentalists could observe the splitting of the G band by 10 cm⁻¹ through the application of 0.6 % strain in graphene.¹¹⁰⁻¹¹²⁾ In Fig. 5-5, we show the calculated Raman spectra of the G band in graphene with the uniaxial strain to the direction of the y axis in Fig. 5-1. The G band splits into two bands (G^+ and G^-) by the strain induction and the peak position shifts to the lower wave number. By increasing the strain, the Raman intensity of G^- band for $\bar{z}(\sigma_+ \sigma_+)z$ becomes larger. By strain induction, the symmetry of graphene (D_{6h}) changes to D_{2h} , and the G band with E_{2g} symmetry splits into A_g (G^-) and B_{1g} (G^+) symmetry modes. The Raman

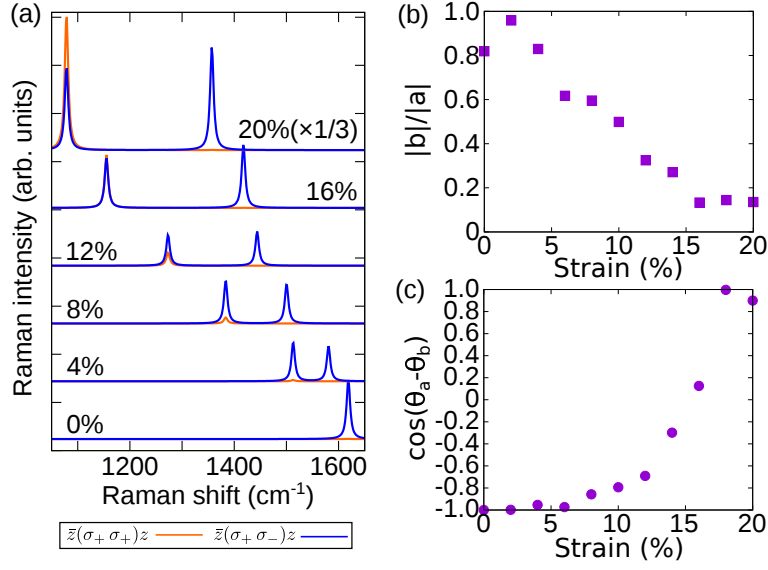


Figure 5-5: (a) Calculated Raman spectra of strain-induced graphene with 0, 4, 8, 12, and 20 % strain to the y direction in Figure 5-1 (e). (b)-(c) Parameters of Raman tensor for strain induced graphene (b) $|b|/|a|$ and (c) $\cos(\theta_a - \theta_b)$. The laser energy in this calculation is 2 eV.

tensors of A_g and B_{1g} phonon modes in D_{2h} symmetry are written by (see Table 2.1)

$$\overleftrightarrow{R}(A_g) = \begin{pmatrix} a & 0 & 0 \\ 0 & b & 0 \\ 0 & 0 & c \end{pmatrix}, \quad (5.2)$$

$$\overleftrightarrow{R}(B_{1g}) = \begin{pmatrix} 0 & d & 0 \\ d & 0 & 0 \\ 0 & 0 & 0 \end{pmatrix}. \quad (5.3)$$

The Raman tensor for B_{1g} is the same as one of the E' modes and the helicity changes in the Raman scattering process. Thus, the G^+ band in Fig. 5-1 changes the helicity even when the strain increases. The Raman intensity of A_g mode in D_{2h} symmetry is calculated as follows;

$$I_s = \left| \mathbf{P}_{\sigma_-}^* \overleftrightarrow{R}(A_g) \mathbf{P}_{\sigma_+} \right|^2 = (a - b)^2, \quad (5.4)$$

$$I_s = \left| \mathbf{P}_{\sigma_+}^* \overleftrightarrow{R}(A_g) \mathbf{P}_{\sigma_+} \right|^2 = (a + b)^2. \quad (5.5)$$

Thus the Raman intensity for $\bar{z}(\sigma_- \sigma_+)z$ [$\bar{z}(\sigma_+ \sigma_+)z$] is zero in the case of $a \sim b$ ($a = -b$). This result indicates that the helicity selection rule for nondegenerate A_g mode

in D_{2h} symmetry can not be known only by the Raman tensor but depends on the value of the parameter a and b , which clearly shows the limitation of the application of Raman tensor. In the case of graphene, $a \sim -b$ is satisfied for small strain, but the difference between a and b ($|a - b|$) becomes small by increasing strain and the selection rule changes not to switch the helicity.

We calculate the parameter of Raman tensor from the first-principles calculation by using Eq. (2.91). Generally, the parameters of Raman tensor are complex numbers since the matrix elements are complex numbers ($a = |a|e^{i\theta_a}$, $b = |b|e^{i\theta_b}$, and $c = |c|e^{i\theta_c}$). Then, the Raman intensity for A_g symmetry in Eqs. (5.4) and (5.5) is expressed by

$$\begin{aligned} I_s &= |a \pm b|^2 \\ &= |a|^2 \left(1 + \left| \frac{b}{a} \right|^2 \pm 2 \left| \frac{b}{a} \right| \cos(\theta_a - \theta_b) \right). \end{aligned} \quad (5.6)$$

The positive (negative) sign in Eq. (5.6) corresponds to the helicity-conserving (-changing) case. In Fig. 5-5 (b) and (c), we show the calculated $|b|/|a|$ and $\cos(\theta_a - \theta_b)$ as a function of strain. The Raman intensity for helicity-changing and helicity-conserving cases for $\sim 16\%$ strain in Fig. 5-5 are almost same since $|b|/|a| \sim 0$ and $\cos(\theta_a - \theta_b) \sim 0$ for 16% strain. such a parameter-changing occurs since the parameter for y direction b in Eq. (5.2) is modulated by the strain along the y direction. It is thus interesting if we observe Raman spectra of the G band for circular polarized light by applying the pressure in which the degeneracy of the G band is lifted. The helicity selection rule of Raman spectra for D_{2h} symmetry can not be determined only by Raman tensor. Thus the materials with D_{2h} symmetry for example black phosphorus are good subjects of research for helicity-resolved Raman spectroscopy which should be a future work.

Finally, we discuss the conservation of angular momentum for the strain-induced graphene. Our calculated results for the spin-split G^+ and G^- bands exhibit the changes of helicity even though these modes are not degenerate. We note that the time-dependent perturbation theory in our calculation does not consider the conservation of angular momentum. Thus, if we assume the conservation of angular momentum among the photon and phonon in the Raman process, the helicity-changing Raman intensities for spin-split G^- and G^+ bands become zero. However, the crystal structures in our calculation do not have continuous rotational symmetry and thus the conservation of angular momentum is generally broken.^{113,114)} The angular momentum of photon can be exchanged with the mechanical rotation around the center of mass or spin angular momentum. Then the helicity-changing Raman spectra would be observed also in nondegenerate modes and this behavior should be confirmed by experimentalists for black phosphorus, strain-induced graphene, and other materials with D_{2h} symmetry.

Chapter 6

Conclusions

In this thesis, we have theoretically discussed the polarization dependence of optical absorption and Raman spectra for atomic layer materials. We performed the theoretical analysis accompanied with the numerical calculation for three subjects: (1) valley polarization in TMDs (Chapter 3), (2) optical anisotropy of GaTe and BP (Chapter 4), and (3) helicity exchange of the first order Raman spectra in graphene and TMDs (Chapter 5). We have developed new programs to calculate (1) the laser-energy-dependent optical absorption and (2) the first-order Raman spectra, based on the first-principles calculation. The electron-photon matrix elements are obtained by the program updated from the previous work,¹¹⁵⁾ putting the wave function calculated within the Quantum Espresso package. The electron-phonon matrix elements are obtained by extracting from the EPW package and modify its source code. We summarize the original points found in this thesis as follows.

Valley polarization in TMDs

We derived the shape of dipole vector of TMDs near the K and K' points by the simple tight-binding analytical calculation. The analytical form of dipole vector of TMDs are compared with that of graphene derived by Grüneis *et al.*⁷⁸⁾ It is clarified that the essential point of dipole vector to give the valley polarization is the existence of the imaginary part that is 90 (−90) degree rotated from the real part at the K (K') point.

By performing the numerical calculation, we clarified the valley polarization of optical transition in the high energy region around E_L that corresponds to the Λ valley. The valley polarization occurs not only at the K and K' valleys, but also at the Λ and Λ' valleys. The degree of the valley polarization at the Λ valley is smaller than that at the K valley. However, the advantage of the Λ valley is that it has a large difference of the intensity of the optical transition due to the strong optical absorption by the

nesting of the energy bands. The valley polarization at the Λ valley would be observed by lifting the degeneracy by magnetic field^{20,23)} or pump-probe method.²⁴⁾

Optical anisotropy of GaTe and BP

We performed the theoretical analysis of anisotropic optical absorption and Raman intensity for GaTe and BP, that is collaborated with experimentalists. The anisotropies of optical absorption and Raman spectra depend on the laser excitation energy and the sample thickness, which can not be explained by the classical theory such as Raman tensor analysis.

We found that the laser energy dependence can be explained by considering the electronic energy band structure combined with the symmetry of the wave function. We also performed the theoretical calculation by the transfer matrix method and the Raman enhancement factor, and clarify that the interference of light in the sample with the substrate is the origin of the thickness dependence of the anisotropy.

Helicity-exchange of the first order Raman spectra in graphene and TMDs

We performed numerical calculations of helicity-dependent Raman spectra of graphene and TMDs based on the first-principles calculation. The calculation results of MoS₂ reproduced the helicity selection rule of TMDs that was experimentally reported by Chen *et al.*²⁶⁾ We also systematically showed the matrix elements to give the helicity exchange in the first-order Raman scattering. Based on our calculation, we gave the theoretical prediction to change the helicity dependence of Raman scattering of the G band of graphene by inducing the in-plane strain. We show that only one of the splitted peaks, i.e. the G⁻ band (from the degenerate G band) gradually changes the helicity dependence by increasing the strain, which implies that the helicity selection rule of Raman scattering of nondegenerate A_g mode in D_{2h} symmetry can not be predicted only from the Raman tensor.

Appendix A

Selection rule for optical dipole transition

In this Appendix, we derive the selection rule of the optical dipole transition for circular polarized light by considering the transition dipole moment.

A.1 Transition Dipole moment

In order to discuss the dipole transition rule, we discuss about the transition dipole moment \mathbf{d} for electric dipole $-e\mathbf{r}$ written by

$$\mathbf{d} = \langle f | (-e)\mathbf{r} | i \rangle = \int \psi_f(\mathbf{r})^* (-e)\mathbf{r} \psi_i(\mathbf{r}) d\mathbf{r}. \quad (\text{A.1})$$

The transition dipole moment in Eq. (A.1) is directly associated with the dipole vector \mathbf{D} as follows;

$$\begin{aligned} \langle f | \nabla | i \rangle &= \frac{i}{\hbar} \langle f | \mathbf{p} | i \rangle \\ &= \frac{im}{\hbar} \langle f | \frac{d\mathbf{r}}{dt} | i \rangle \\ &= \frac{m}{\hbar^2} \langle f | [\mathbf{r}, H] | i \rangle \\ &= \frac{m}{\hbar^2} \langle f | (\mathbf{r}H - H\mathbf{r}) | i \rangle \\ &= \frac{m}{\hbar^2} (\langle f | \mathbf{r}E_i | i \rangle - \langle f | E_f \mathbf{r} | i \rangle) \\ &= \frac{m}{e\hbar^2} (E_f - E_i) \langle f | (-e)\mathbf{r} | i \rangle, \end{aligned} \quad (\text{A.2})$$

where E_i and E_f is eigen energy of the state $|i\rangle$ and $|f\rangle$, respectively. From line two to three in Eq. (A.2), we use the definition of the Heisenberg equation of motion $\frac{d\mathcal{O}}{dt} = \frac{i}{\hbar}[H, \mathcal{O}]$. Then we discuss the symmetry of the transition dipole moment $\mathbf{d} = \langle f|(-e)\mathbf{r}|i\rangle$ to obtain the selection rule of dipole transition.

By using main, azimuthal, magnetic, and spin quantum numbers (n, ℓ, m, s_z , respectively) of an atom, we write the wave function as follows;

$$\psi_{n,\ell,m,s_z}(r, \theta, \phi, s_z) = R_{n,\ell}(r)Y_{\ell,m}(\theta, \phi)\sigma_s(s_z), \quad (\text{A.3})$$

where $R_{n,\ell}(r)$, $Y_{\ell,m}(\theta, \phi)$, and $\sigma_s(s_z)$ are the radial wave function, spherical harmonics, and spin wave function, respectively. The spherical harmonics is further decomposed by the function of θ and ϕ as follows;

$$Y_{\ell,m}(\theta, \phi) = \Theta_{\ell,m}(\theta) \cdot \Phi_m(\phi), \quad (\text{A.4})$$

$$\Theta_{\ell,m}(\theta) = (-1)^m \cdot \sqrt{\frac{2\ell+1}{2}} \cdot \sqrt{\frac{(\ell-m)!}{(\ell+m)!}} \cdot P_{\ell}^m(\cos\theta) \quad (|m| \leq \ell), \quad (\text{A.5})$$

$$\Phi_m(\phi) = \frac{1}{\sqrt{2\pi}} e^{im\phi}, \quad (\text{A.6})$$

where $P_{\ell}^m(\cos\theta)$ is the associated Legendre polynomial. Furthermore, the electric dipole $(-e)\mathbf{r}$ in cartesian coordinate is written by using r, θ, ϕ as follows;

$$(-e)\mathbf{r} = (-e)(r \sin\theta \cos\phi, r \sin\theta \sin\phi, r \cos\theta). \quad (\text{A.7})$$

By using Eqs. (A.3)-(A.7), the transition dipole moment \mathbf{d} is written by

$$\begin{aligned} \mathbf{d} &= \langle f|(-e)\mathbf{r}|i\rangle \\ &= \psi_{n',\ell',m',s'_z}(r, \theta, \phi, s'_z)|(-e)\mathbf{r}|\psi_{n,\ell,m,s_z}(r, \theta, \phi, s_z) \\ &\propto \langle \sigma_s(s'_z)|\sigma_s(s_z)\rangle \int_{r=0}^{\infty} \int_{\theta=0}^{\pi} \int_{\phi=0}^{2\pi} R_{n',\ell'}^*(r)R_{n,\ell}(r)P_{\ell'}^{m'}(\cos\theta)P_{\ell}^m(\cos\theta)e^{i(m-m')\phi} \\ &\quad \times r^3 \sin\theta \begin{pmatrix} \sin\theta \cos\phi \\ \sin\theta \sin\phi \\ \cos\theta \end{pmatrix} drd\theta d\phi \end{aligned}$$

$$\begin{aligned}
&= \delta_{s'_z, s_z} \int_{r=0}^{\infty} R_{n', \ell'}^*(r) R_{n, \ell}(r) r^3 dr \cdot \int_{\theta=0}^{\pi} P_{\ell'}^{m'}(\cos \theta) P_{\ell}^m(\cos \theta) \begin{pmatrix} \sin \theta \\ \sin \theta \\ \cos \theta \end{pmatrix} \sin \theta d\theta \\
&\quad \times \int_{\phi=0}^{2\pi} \begin{pmatrix} \cos \phi \\ \sin \phi \\ 1 \end{pmatrix} e^{i(m-m')\phi} d\phi. \tag{A.8}
\end{aligned}$$

The $\delta_{s'_z, s_z}$ appears since the space integral does not affect the spin wave function and we just use the orthogonality of the spin wave function. Then we obtain the selection rule for spin:

$$\Delta s_z = s'_z - s_z = 0. \tag{A.9}$$

The selection rules for ℓ and m are given from the integral for θ and ϕ in Eq. (A.8). We confirm the selection rule for x , y , and z components as below.

z component of the transition dipole moment

We start from the z component of the transition dipole moment in Eq. (A.8). From Eq. (A.8), the z component of the \mathbf{d} which is related with θ and ϕ can be written as,

$$d_z \propto \int_{\theta=0}^{\pi} P_{\ell'}^{m'}(\cos \theta) P_{\ell}^m(\cos \theta) \cos \theta \sin \theta d\theta \cdot \int_{\phi=0}^{2\pi} e^{i(m-m')\phi} d\phi. \tag{A.10}$$

The integral for ϕ ($\int_{\phi=0}^{2\pi} e^{i(m-m')\phi} d\phi$) directly becomes the delta function $\delta_{m, m'}$ which gives the selection rule $\Delta m = m' - m = 0$. For the integral of θ , defining $z = \cos \theta$ and $dz = -\sin \theta d\theta$, we obtain

$$\int_{\theta=0}^{\pi} P_{\ell'}^m(\cos \theta) P_{\ell}^m(\cos \theta) \cos \theta \sin \theta d\theta = \int_{-1}^1 P_{\ell'}^m(z) P_{\ell}^m(z) z dz. \tag{A.11}$$

Here we use the recurrence relation for associated Legendre polynomial;

$$z \cdot P_{\ell}^m(z) = \frac{\ell - m + 1}{2\ell + 1} \cdot P_{\ell+1}^m(z) \frac{\ell + m}{2\ell + 1} \cdot P_{\ell-1}^m(z). \tag{A.12}$$

Using Eqs. (A.11) and (A.12), we obtain

$$\begin{aligned}
\int_{\theta=0}^{\pi} P_{\ell'}^{m'}(z) P_{\ell}^m(z) z dz &= \frac{\ell - m + 1}{2\ell + 1} \int_{-1}^1 P_{\ell'}^{m'}(z) P_{\ell+1}^m(z) dz + \frac{\ell + m}{2\ell + 1} \int_{-1}^1 P_{\ell'}^{m'}(z) P_{\ell-1}^m(z) dz \\
&= \frac{\ell - m + 1}{2\ell + 1} \delta_{\ell+1, \ell'} + \frac{\ell + m}{2\ell + 1} \delta_{\ell-1, \ell'}. \tag{A.13}
\end{aligned}$$

From the first to second line in Eq. (A.13), we use the orthogonality of associated Legendre polynomial;

$$\int_{-1}^1 P_{\ell'}^m(z) P_{\ell}^m(z) dz = \delta_{\ell, \ell'}. \quad (\text{A.14})$$

From Eq. (A.13), we obtain the selection rule for azimuthal quantum number: $\Delta\ell = \ell' - \ell = \pm 1$. By summarizing the selection rule for z component of the transition dipole moment, we can write,

$$d_z : \begin{cases} \Delta\ell = \pm 1, \\ \Delta m = 0, \\ \Delta s_z = 0, \end{cases} \quad (\text{A.15})$$

x and y components of the transition dipole moment

For the x and y components of the transition dipole moment, in Eq. (A.8). From Eq. (A.8), the x and y components of the \mathbf{d} which are related with θ and ϕ can be written, respectively, as,

$$d_x \propto \int_{\theta=0}^{\pi} P_{\ell'}^{m'}(\cos\theta) P_{\ell}^m(\cos\theta) \sin^2\theta d\theta \cdot \int_{\phi=0}^{2\pi} e^{i(m-m')\phi} \cos\phi d\phi, \quad (\text{A.16})$$

$$d_y \propto \int_{\theta=0}^{\pi} P_{\ell'}^{m'}(\cos\theta) P_{\ell}^m(\cos\theta) \sin^2\theta d\theta \cdot \int_{\phi=0}^{2\pi} e^{i(m-m')\phi} \sin\phi d\phi. \quad (\text{A.17})$$

The integral for ϕ in Eqs. (A.16) and (A.17) are, respectively, written as;

$$\begin{aligned} \int_{\phi=0}^{2\pi} e^{i(m-m')\phi} \cos\phi d\phi &= \frac{1}{2} \int_{\phi=0}^{2\pi} e^{i(m-m')\phi} (e^{i\phi} + e^{-i\phi}) d\phi \\ &= \frac{1}{2} \int_{\phi=0}^{2\pi} (e^{i(m-m'+1)\phi} + e^{i(m-m'-1)\phi}) d\phi \\ &= \pi(\delta_{m+1, m'} + \delta_{m-1, m'}), \end{aligned} \quad (\text{A.18})$$

$$\begin{aligned} \int_{\phi=0}^{2\pi} e^{i(m-m')\phi} \sin\phi d\phi &= \frac{1}{2i} \int_{\phi=0}^{2\pi} e^{i(m-m')\phi} (e^{i\phi} - e^{-i\phi}) d\phi \\ &= \frac{1}{2i} \int_{\phi=0}^{2\pi} (e^{i(m-m'+1)\phi} - e^{i(m-m'-1)\phi}) d\phi \\ &= -\pi i(\delta_{m+1, m'} - \delta_{m-1, m'}). \end{aligned} \quad (\text{A.19})$$

Thus we obtain the selection rule for m in the x and y components of transition dipole moment as $\Delta m = m' - m = \pm 1$. From Eqs. (A.18) and (A.19), we can understand the dipole transition by circular polarized σ_+ (σ_-) light corresponds to the $\Delta m = +1$ (-1).

From Eqs. (A.18) and (A.19), the transition matrix element $\mathbf{p}_{\sigma_+} \cdot \mathbf{d}$ and $\mathbf{p}_{\sigma_-} \cdot \mathbf{d}$ are, respectively, written by

$$\begin{aligned} \mathbf{P}_{\sigma_+} \cdot \mathbf{d} &= (1, i, 0) \begin{pmatrix} d_x \\ d_y \\ d_z \end{pmatrix} \\ &\propto \pi(\delta_{m+1, m'} + \delta_{m-1, m'}) + i \cdot (-\pi i)(\delta_{m+1, m'} - \delta_{m-1, m'}) \\ &= 2\pi\delta_{m+1, m'}, \end{aligned} \quad (\text{A.20})$$

$$\begin{aligned} \mathbf{P}_{\sigma_-} \cdot \mathbf{d} &= (1, -i, 0) \begin{pmatrix} d_x \\ d_y \\ d_z \end{pmatrix} \\ &\propto \pi(\delta_{m-1, m'} + \delta_{m+1, m'}) + (-i) \cdot (-\pi i)(\delta_{m+1, m'} - \delta_{m-1, m'}) \\ &= 2\pi\delta_{m-1, m'}. \end{aligned} \quad (\text{A.21})$$

Thus the dipole transition by circular polarized σ_+ (σ_-) light corresponds to the transition by $\Delta m = +1$ (-1).

Finally we derive the selection rule for ℓ in the x and y components. The x and y components of the integral for θ of the transition dipole moment in Eq. (A.16) and (A.17) are the same ($= \int_{\theta=0}^{\pi} P_{\ell'}^{m'}(\cos\theta) P_{\ell}^m(\cos\theta) \sin^2\theta d\theta$). We already obtain the selection rule for $m : m' = m \pm 1$ in Eqs. (A.18) and (A.19). Firstly let us consider the case of $m' = m + 1$. We use the recurrence formula for associated Legendre polynomial;

$$(1 - z^2)^{1/2} P_{\ell}^m(z) = \frac{1}{2\ell + 1} \{P_{\ell+1}^{m+1}(z) - P_{\ell-1}^{m+1}(z)\}. \quad (\text{A.22})$$

Using Eq. (A.22) and the transformation of variable $z = \cos\theta$, we obtain

$$\begin{aligned} \int_{\theta=0}^{\pi} P_{\ell'}^{m+1}(\cos\theta) P_{\ell}^m(\cos\theta) \sin^2\theta d\theta &= \int_{-1}^1 P_{\ell'}^{m+1}(z) P_{\ell}^m(z) (1 - z^2)^{1/2} dz \\ &= \frac{1}{2\ell + 1} \int_{-1}^1 P_{\ell'}^{m+1} \{P_{\ell+1}^{m+1}(z) - P_{\ell-1}^{m+1}(z)\} dz \\ &= \frac{1}{2\ell + 1} (\delta_{\ell+1, \ell'} - \delta_{\ell-1, \ell'}). \end{aligned} \quad (\text{A.23})$$

In the case of $m' = m - 1$, we use the recurrence relation for associated Legendre polynomial which we change $m \rightarrow m - 1$ and $\ell \rightarrow \ell'$ in Eq. (A.22) as follows;

$$(1 - z^2)^{1/2} P_{\ell'}^{m-1}(z) = \frac{1}{2\ell' + 1} \{P_{\ell'+1}^m(z) - P_{\ell'-1}^m(z)\}. \quad (\text{A.24})$$

Using Eq. (A.24) and the transformation of variable $z = \cos \theta$, we obtain

$$\begin{aligned}
\int_{\theta=0}^{\pi} P_{\ell'}^{m-1}(\cos \theta) P_{\ell}^m(\cos \theta) \sin^2 \theta d\theta &= \int_{-1}^1 P_{\ell'}^{m-1}(z) P_{\ell}^m(z) (1-z^2)^{1/2} dz \\
&= \frac{1}{2\ell'+1} \int_{-1}^1 \left\{ P_{\ell'+1}^m(z) - P_{\ell'-1}^m(z) \right\} P_{\ell}^m(z) dz \\
&= \frac{1}{2\ell'+1} (\delta_{\ell, \ell'+1} - \delta_{\ell, \ell'-1}). \tag{A.25}
\end{aligned}$$

From Eqs. (A.23) and (A.25), we obtain the selection rule for x and y components of the transition dipole moment and we can write,

$$d_x, d_y : \begin{cases} \Delta \ell = \pm 1, \\ \Delta m = \pm 1, \\ \Delta s_z = 0. \end{cases} \tag{A.26}$$

Summary of the selection rule

From Eqs. (A.15) and (A.26), we summarize the selection rule in the dipole transition as follows;

$$\Delta s_z = 0, \tag{A.27}$$

$$\Delta \ell = \pm 1, \tag{A.28}$$

$$\Delta m = 0, \pm 1. \tag{A.29}$$

In the case of many body system, the selection rule for total azimuthal quantum number L , total spin quantum number S_z , and the total angular momentum $J = L + S$, the z component of total angular momentum m_J are given as follows;

$$\Delta S_z = 0, \tag{A.30}$$

$$\Delta L = 0, \pm 1, \tag{A.31}$$

$$\Delta J = 0, \pm 1 \text{ (the transition } j = 0 \rightarrow 0 \text{ is excluded),} \tag{A.32}$$

$$\Delta m_J = 0, \pm 1, \tag{A.33}$$

which we need the further general discussion by using the representation of rotation group (see for example Ref. 116).

A.2 Dipole selection rule under the rotational symmetry

The dipole selection rule discussed in Sec. A.1 is modified under the rotational symmetry. If Bloch states at a high symmetry point when we consider a q -fold rotation are invariant for $R\left(\frac{2\pi}{q}, \hat{\mathbf{z}}\right)$, we can write the wave function $|\psi_{c(v)}(\mathbf{k})\rangle$ as follows⁵⁵;

$$R\left(\frac{2\pi}{q}, \hat{\mathbf{z}}\right) |\psi_{c(v)}(\mathbf{k})\rangle = e^{-i\frac{2\pi}{q}m^c(v)} |\psi_{c(v)}(\mathbf{k})\rangle. \quad (\text{A.34})$$

Using Eqs.(A.34), the $\langle\psi_c(\mathbf{k})|\mathbf{r}|\psi_v(\mathbf{k})\rangle$ can be calculated as follows;

$$\begin{aligned} \langle\psi_c(\mathbf{k})|\mathbf{r}|\psi_v(\mathbf{k})\rangle &= \langle\psi_c(\mathbf{k})|R^{-1}R\mathbf{r}R^{-1}R|\psi_v(\mathbf{k})\rangle \\ &= e^{i\frac{2\pi}{q}(m_J-c-m_J^v)} \langle\psi_c(\mathbf{k})|R\mathbf{r}R^{-1}|\psi_v(\mathbf{k})\rangle \\ &= e^{i\frac{2\pi}{q}(m_J-c-m_J^v)} \langle\psi_c(\mathbf{k})| \begin{pmatrix} x \cos \frac{2\pi}{q} - y \sin \frac{2\pi}{q} \\ x \sin \frac{2\pi}{q} + y \cos \frac{2\pi}{q} \\ 0 \end{pmatrix} |\psi_v(\mathbf{k})\rangle \\ &= e^{i\frac{2\pi}{q}(m_J-c-m_J^v)} \begin{pmatrix} \langle\psi_c(\mathbf{k})|x|\psi_v(\mathbf{k})\rangle \cos \frac{2\pi}{q} - \langle\psi_c(\mathbf{k})|y|\psi_v(\mathbf{k})\rangle \sin \frac{2\pi}{q} \\ \langle\psi_c(\mathbf{k})|x|\psi_v(\mathbf{k})\rangle \sin \frac{2\pi}{q} + \langle\psi_c(\mathbf{k})|y|\psi_v(\mathbf{k})\rangle \cos \frac{2\pi}{q} \\ 0 \end{pmatrix}. \end{aligned} \quad (\text{A.35})$$

By using Eq. (A.35), the electron-photon matrix element for circular polarized light $\langle\psi_c(\mathbf{k})|\mathbf{r} \cdot \mathbf{P}_{\sigma\pm}|\psi_v(\mathbf{k})\rangle$ is calculated as follows;

$$\begin{aligned} \langle\psi_c(\mathbf{k})|\mathbf{r} \cdot \mathbf{P}_{\sigma\pm}|\psi_v(\mathbf{k})\rangle &= e^{i\frac{2\pi}{q}(m_J-c-m_J^v)} \langle\psi_c(\mathbf{k})|(x \pm iy)|\psi_v(\mathbf{k})\rangle \left(\cos \frac{2\pi}{q} \pm i \sin \frac{2\pi}{q} \right) \\ &= e^{i\frac{2\pi}{q}(m_J-c-m_J^v \pm 1)} \langle\psi_c(\mathbf{k})|(x \pm iy)|\psi_v(\mathbf{k})\rangle \\ &= e^{i\frac{2\pi}{q}(m_J-c-m_J^v \pm 1)} \langle\psi_c(\mathbf{k})|\mathbf{r} \cdot \mathbf{P}_{\sigma\pm}|\psi_v(\mathbf{k})\rangle. \end{aligned} \quad (\text{A.36})$$

When the relation in Eq. (A.36) is identically satisfied, we can obtain the following relation;

$$e^{i\frac{2\pi}{q}(m_J-c-m_J^v \pm 1)} = 1. \quad (\text{A.37})$$

Thus the following relation is expected in q -fold rotational system;

$$m_J^c - m_J^v = \pm 1 + qN \quad (N = 0, \pm 1, \pm 2, \dots), \quad (\text{A.38})$$

where N is the arbitrary integer and $+1$ (-1) in the right-hand side in Eq. (A.38) corresponds to the σ_+ (σ_-) light.

Appendix B

Interference effect of optical absorption and Raman scattering

B.1 Interference effect of optical measurements

B.1.1 Interference effect for optical absorption

The interference effect of the sample and substrate contributes to the dependence of the observed optical extinction and Raman scattering on thickness of the sample and wavelength of the laser. We evaluate the interference effect by calculating the transition probability with use of the transfer matrix method for the optical absorption/extinction.

In Fig. B-1, we show the geometry which we consider now for the transfer matrix. The electromagnetic wave propagates from the $-z$ to $+z$ direction. Here we consider four media labeled by $u = 1$ (air), 2 (sample), 3 (substrate), and 4 (air). Let us derive the reflection, transmission, and absorption probability. We assume the electromagnetic wave oscillating with a frequency ω and we obtain the relation between the electric field and magnetic field from the Maxwell equation $\nabla \times E = -\mu_0 \frac{\partial H}{\partial t}$ as,

$$i\omega\mu_0 H_{i,x}(z) = -\frac{\partial E_{i,y}(z)}{\partial z}, \quad (\text{B.1})$$

where x and y are taken as in-plane directions, z is taken as the direction perpendicular to the substrate layer, and μ_0 denotes the magnetic permeability in vacuum. The electric field in the i -th medium at the position of z is written as

$$E_{i,y}(z) = E_{i,+} e^{-ik_{i,z}(z-L_i)} + E_{i,-} e^{ik_{i,z}(z-L_i)}, \quad (\text{B.2})$$

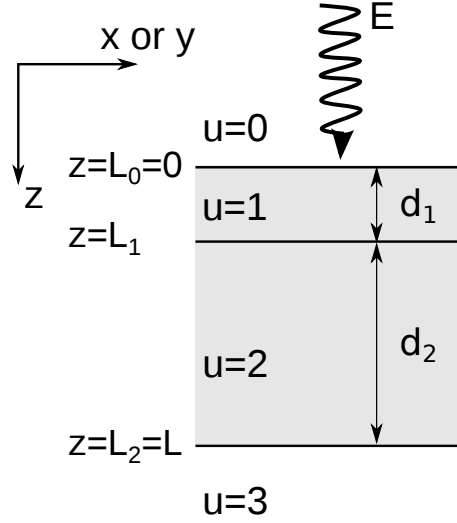


Figure B-1: Geometry of the system which we consider for the transfer matrix.

where $E_{i,+}$ ($E_{i,-}$) is the amplitude of the electric field propagating in the $+z$ ($-z$) direction and $L_i = \sum_{u=1}^{i-1} d_u$ is the thickness of the u -th medium. From Eqs. (B.1) and (B.2), we can also obtain the expression for the magnetic field as

$$H_{i,x} = -\Gamma_i \left(-E_{i,+} e^{-ik_{i,z}(z-L_i)} + E_{i,-} e^{ik_{i,z}(z-L_i)} \right), \quad (\text{B.3})$$

where $\Gamma_i = \frac{k_{i,z}}{\omega\mu_0} = n_i \sqrt{\frac{\epsilon_0}{\mu_0}}$ is the wave impedance of the medium in units of Ω . Using $E_{i,y}(L_i)$ and $H_{i,x}(L_i)$, E_+ and E_- are written as

$$E_{i,+} = \frac{1}{2} \left(E_{i,y}(L_i) + \frac{H_{i,x}(L_i)}{\Gamma_i} \right), \quad (\text{B.4})$$

$$E_{i,-} = \frac{1}{2} \left(E_{i,y}(L_i) - \frac{H_{i,x}(L_i)}{\Gamma_i} \right), \quad (\text{B.5})$$

Using Eqs. (B.4) and (B.5), we can obtain the conditions of propagating the fields in the i -th medium ($L_i < z < L_{i+1}$) as follows;

$$\begin{pmatrix} E_{i,y}(z) \\ H_{i,x}(z) \end{pmatrix} = \begin{pmatrix} \frac{1}{2}(e^{-ik_{i,z}(z-L_i)} + e^{ik_{i,z}(z-L_i)}) & \frac{1}{2\Gamma_i}(e^{-ik_{i,z}(z-L_i)} - e^{ik_{i,z}(z-L_i)}) \\ \frac{\Gamma_i}{2}(e^{-ik_{i,z}(z-L_i)} - e^{ik_{i,z}(z-L_i)}) & \frac{1}{2}(e^{-ik_{i,z}(z-L_i)} + e^{ik_{i,z}(z-L_i)}) \end{pmatrix} \begin{pmatrix} E_{i,y}(L_i) \\ H_{i,x}(L_i) \end{pmatrix}. \quad (\text{B.6})$$

When we use the boundary conditions for $E_{i,y}$ and $H_{i,x}$ at the $z = L_i$ that are $E_{i,y}(L_i) = E_{i+1,y}(L_i)$ and $H_{i,x}(L_i) = H_{i+1,x}(L_i)$, the transfer matrix of the boundary conditions becomes an identity matrix. Therefore the relations of $E_{i,y}$ and $H_{i,x}$ between the depth

at $z = L_i$ and $z = L_{i+1}$ are given by

$$\begin{aligned} \begin{pmatrix} E_{i,y}(L_{i+1}) \\ H_{i,x}(L_{i+1}) \end{pmatrix} &= \begin{pmatrix} \frac{1}{2}(e^{-ik_{i,z}(z-L_i)} + e^{ik_{i,z}(z-L_i)}) & \frac{1}{2\Gamma_i}(e^{-ik_{i,z}(z-L_i)} - e^{ik_{i,z}(z-L_i)}) \\ \frac{\Gamma_i}{2}(e^{-ik_{i,z}(z-L_i)} - e^{ik_{i,z}(z-L_i)}) & \frac{1}{2}(e^{-ik_{i,z}(z-L_i)} + e^{ik_{i,z}(z-L_i)}) \end{pmatrix} \begin{pmatrix} E_{i,y}(L_i) \\ H_{i,x}(L_i) \end{pmatrix} \\ &\equiv \mathcal{M}_i \begin{pmatrix} E_{i,y}(L_i) \\ H_{i,x}(L_i) \end{pmatrix}. \end{aligned} \quad (\text{B.7})$$

Using the relation of Eq. (B.7) repeatedly, we can obtain the relations for $E_{i,y}$ and $H_{i,x}$ between the depth at $z = 0$ and $z = L$ as follows;

$$\begin{aligned} \begin{pmatrix} E_{0,y}(0) \\ H_{0,x}(0) \end{pmatrix} &= \mathcal{M}_1^{-1} \mathcal{M}_2^{-1} \begin{pmatrix} E_{3,y}(L) \\ H_{3,x}(L) \end{pmatrix} \\ &= \mathcal{M} \begin{pmatrix} E_{3,y}(L) \\ H_{3,x}(L) \end{pmatrix}. \end{aligned} \quad (\text{B.8})$$

The \mathcal{M} is called the transfer matrix written by

$$\mathcal{M} = \mathcal{M}_1^{-1} \mathcal{M}_2^{-1} = \begin{pmatrix} M_{11} & M_{12} \\ M_{21} & M_{22} \end{pmatrix}. \quad (\text{B.9})$$

The reflection and transmission coefficients, r and t , are associated with $E_{i,+}$ and $E_{i,-}$ as follows;

$$r = \frac{E_{0,-}}{E_{0,+}}, \quad (\text{B.10})$$

$$t = \frac{E_{3,+}}{E_{0,+}}, \quad (\text{B.11})$$

Using Eq. (B.10) and (B.11), we can obtain the expression for r and t as follows:

$$r = \frac{M_{11}\Gamma_0 + M_{12}\Gamma_0\Gamma_3 - M_{21} - M_{22}\Gamma_3}{M_{11}\Gamma_0 + M_{12}\Gamma_0\Gamma_3 + M_{21} + M_{22}\Gamma_3}, \quad (\text{B.12})$$

$$t = \frac{2\Gamma_0}{M_{11}\Gamma_0 + M_{12}\Gamma_0\Gamma_3 - M_{21} - M_{22}\Gamma_3}. \quad (\text{B.13})$$

By using Eqs. (4.1) and (4.2), reflection, transmission, and absorption probabilities (\mathcal{R} , \mathcal{T} , and \mathcal{A}) are given by,

$$\mathcal{R} = |r|^2, \quad (\text{B.14})$$

$$\mathcal{T} = |t|^2, \quad (\text{B.15})$$

$$\mathcal{A} = 1 - \mathcal{R} - \mathcal{T}. \quad (\text{B.16})$$

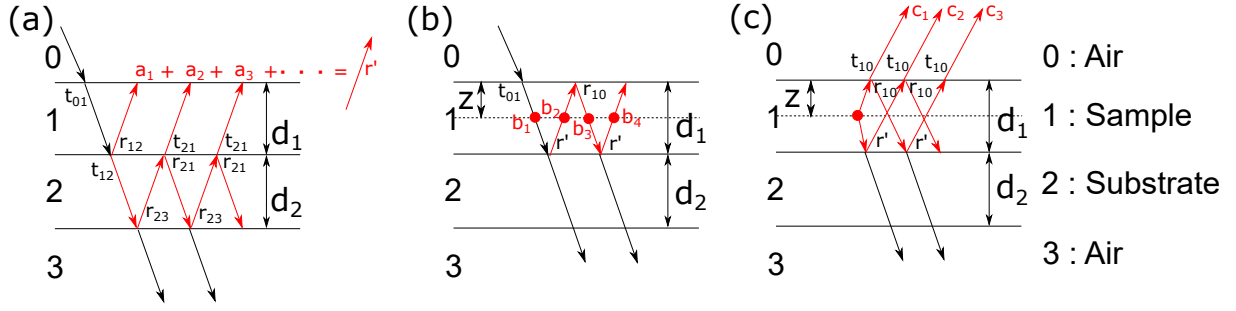


Figure B-2: (a) Calculation of the effective reflection at the sample($i = 1$)/substrate($i = 2$) interface, including multiple reflections in the lower substrate. (b)-(c) Calculation of the amplitudes of (b) the excitation and (c) the scattering light at depth z in the sample ($i = 1$).

B.1.2 Interference effect of Raman scattering

In this section, we derive the enhancement factor of Raman intensity by the interference effect.⁹⁷⁾ We assume the geometry of the sample on the substrate as shown in Fig. B-2, that is, we consider four media labeled by $i = 0, 1, 2$, and 3 : air, sample, SiO₂, and Si, respectively. The sample thicknesses of media 1 and 2 are defined by d_1 and d_2 , respectively. We consider the reflection and transmission at the interface between the media, and the absorption by the sample and substrates. The scattering event occurs at the depth x from the interface between the media 1 and 2.

We first derive the effective reflection coefficient at the interference between 1 and 2 defined by r' as shown in Fig. B-2 (a). r' is given by the summation of a_j as follows,

$$\begin{aligned}
 a_1 &= r_{12} \\
 a_2 &= t_{12}e^{-i\beta_2}r_{23}e^{-i\beta_2}t_{21} = t_{12}t_{21}r_{23}e^{-2i\beta_2} \\
 a_3 &= t_{12}e^{-i\beta_2}r_{23}e^{-i\beta_2}t_{21}r_{23}e^{-i\beta_2}t_{21} = a_2r_{21}r_{23}e^{-2i\beta_2} \\
 &\dots \\
 a_n &= a_2 \cdot (r_{21}r_{23}e^{-2i\beta_2})^n.
 \end{aligned} \tag{B.17}$$

Then the total effective reflectance is given by the summation of geometric series as

follows;

$$\begin{aligned}
r' &= r_{12} + t_{12}t_{21}r_{23}e^{-2i\beta_2} \cdot \sum_{n=0}^{\infty} (r_{21}r_{23}e^{-2i\beta_2})^n \\
&= r_{12} + \frac{t_{12}t_{21}r_{23}e^{-2i\beta_2}}{1 - r_{21}r_{23}e^{-2i\beta_2}} \\
&= \frac{r_{12} + r_{23}e^{-2i\beta_2}}{1 + r_{12}r_{23}e^{-2i\beta_2}}.
\end{aligned} \tag{B.18}$$

We use the relations : $r_{21} = -r_{12}$ and $t_{12}t_{21} = 1 - r_{12}^2$ from the second to third line in Eq. B.18.

Secondly, we derive the total amplitude of excitation light at depth x in the sample as shown in Fig. (B-2) (b). Using r' in Eq. (B.18), we sum up all path shown in Fig. B-2 (b) as follows;

$$\begin{aligned}
b_1 &= t_{01}e^{-i\beta_z} \\
b_2 &= t_{01}e^{-i\beta_z}r'e^{-i(\beta_1-\beta_x)} = t_{01}r'e^{-i(2\beta_1-\beta_z)} \\
b_3 &= t_{01}e^{-i\beta_z}r'e^{-i\beta_1}r_{10}e^{-i\beta_z} = b_1 (r'r_{10}e^{-2i\beta_1})^1 \\
b_4 &= t_{01}e^{-i\beta_z}r'e^{-i\beta_1}r_{10}e^{-i\beta_z}r'e^{-i(\beta_1-\beta_z)} = b_2 (r'r_{10}e^{-2i\beta_1})^1 \\
&\dots \\
b_{2n+1} &= b_1 (r'r_{10}e^{-2i\beta_1})^n
\end{aligned} \tag{B.19}$$

$$b_{2n+2} = b_2 (r'r_{10}e^{-2i\beta_1})^n. \tag{B.20}$$

Thus, the total amplitude of the excitation light at the depth z from the top of sample is given by the summation of geometric series as follows;

$$\begin{aligned}
F_{ex}(z) &= \sum_{n=0}^{\infty} (b_{2n+1} + b_{2n+2}) \\
&= \sum_{n=0}^{\infty} (t_{01}e^{-i\beta_z} (r'r_{10}e^{-2i\beta_1})^n + t_{01}e^{-i\beta_z}r'e^{-i(\beta_1-\beta_x)} (r'r_{10}e^{-2i\beta_1})^n) \\
&= t_{01} \frac{e^{-i\beta_z} + r'e^{-i(2\beta_1-\beta_x)}}{1 + r'r_{10}e^{-2i\beta_1}} \\
&= t_{01} \frac{(1 + r_{12}r_{23}e^{-2i\beta_2})e^{-i\beta_z} + (r_{12} + r_{23}e^{-2i\beta_2})e^{-2i(\beta_1-\beta_z)}}{1 + r_{12}r_{23}e^{-2i\beta_2} + (r_{12} + r_{23}e^{-2i\beta_2})r_{01}e^{-2i\beta_1}}.
\end{aligned} \tag{B.21}$$

The light scattered at depth z interferes in the path through the sample to be observed by the detector. The total amplitude of Raman scattering light from depth

z in the sample [Fig. B-2 (c)] is calculated as follows;

$$c_1 = e^{-i\beta z} \cdot t_{10} = t_{10}e^{-i\beta z}$$

$$c_2 = e^{-i(\beta_1 - \beta z)} \cdot r' \cdot e^{-i\beta_1} \cdot t_{10} = t_{10}r'e^{-i(2\beta_1 - \beta z)}$$

$$c_3 = e^{-i\beta z} \cdot r_{10} \cdot e^{-i\beta_1} \cdot r' \cdot e^{-i\beta z} \cdot t_{10} = c_1 (r'r_{10}e^{-2i\beta_1})^1$$

$$c_4 = e^{-i(\beta_1 - \beta z)} \cdot r' \cdot e^{-i\beta_1} \cdot r_{10} \cdot e^{-i\beta_1} \cdot t_{10} = c_2 (r'r_{10}e^{-2i\beta_1})^1$$

...

$$c_{2n+1} = c_1 \cdot (r'r_{10}e^{-2i\beta_1})^n \quad (\text{B.22})$$

$$c_{2n+2} = c_2 \cdot (r'r_{10}e^{-2i\beta_1})^n. \quad (\text{B.23})$$

Thus the total amplitude of Raman scattering light from depth z in the sample is calculated by the summation of geometric series as follows;

$$\begin{aligned} F_{sc}(z) &= \sum_{n=0}^{\infty} (c_{2n+1} + c_{2n+2}) \\ &= \sum_{n=0}^{\infty} (t_{10} \cdot e^{-i\beta z} \cdot (r'r_{10}e^{-2i\beta_1})^n + t_{10} \cdot e^{-i\beta z} \cdot r' \cdot e^{-i(\beta_1 - \beta z)} \cdot (r'r_{10}e^{-2i\beta_1})^n) \\ &= t_{10} \frac{(1 + r_{12}r_{23}e^{-2i\beta_2}) e^{-i\beta z} + (r_{12} + r_{23}e^{-2i\beta_2}) e^{-2i(\beta_1 - \beta z)}}{1 + r_{12}r_{23}e^{-2i\beta_2} + (r_{12} + r_{23}e^{-2i\beta_2}) r_{01}e^{-2i\beta_1}}. \end{aligned} \quad (\text{B.24})$$

Then the total enhancement factor F is written as follows;

$$F = \int_0^{d_1} |F_{ex} \cdot F_{sc}|^2 s z, \quad (\text{B.25})$$

and Raman intensity I is written as $I = I_i \cdot F$, with the intrinsic Raman intensity denoted by I_i .

Appendix C

Character table

In this chapter, we show the character table and the product table which we need in this thesis.

Table C.1: Character table of the D_{6h} point group. Graphene belongs to this symmetry group.

	E	$2C_6$	$2C_3$	C_2	$3C'_2$	$3C''_2$	i	$2S_3$	$2S_6$	σ_h	$3\sigma_d$	$3\sigma_v$
$\Gamma_1^+(A_{1g})$	1	1	1	1	1	1	1	1	1	1	1	1
$\Gamma_2^+(A_{2g})$	1	1	1	1	-1	-1	1	1	1	1	-1	-1
$\Gamma_3^+(B_{1g})$	1	-1	-1	1	-1	1	-1	1	-1	1	-1	1
$\Gamma_4^+(A_{2g})$	1	-1	1	-1	-1	1	1	-1	1	-1	-1	1
$\Gamma_5^+(E_{1g})$	2	1	-1	-2	0	0	2	1	-1	-2	0	0
$\Gamma_6^+(E_{2g})$	2	-1	-1	2	0	0	2	-1	-1	-2	0	0
$\Gamma_1^-(A_{1u})$	1	1	1	1	1	1	-1	-1	-1	-1	-1	-1
$\Gamma_2^-(A_{2u})$	1	1	1	1	-1	-1	-1	-1	-1	-1	1	1
$\Gamma_3^-(B_{1u})$	1	-1	1	-1	1	-1	-1	1	-1	1	-1	1
$\Gamma_4^-(A_{2u})$	1	-1	1	-1	-1	1	-1	1	-1	1	1	-1
$\Gamma_5^-(E_{1u})$	2	1	-1	-2	0	0	-2	-1	1	2	0	0
$\Gamma_6^-(E_{2u})$	2	-1	-1	2	0	0	-2	1	1	-2	0	0

Table C.2: Character table of the D_{3h} point group. TMDs belong to this symmetry group.

	E	$2C_3$	$3C'_2$	σ_h	$2S_3$	$3\sigma_v$
$\Gamma_1(A'_1)$	1	1	1	1	1	1
$\Gamma_2(A'_2)$	1	1	-1	1	1	-1
$\Gamma_3(E')$	2	-1	0	2	-1	0
$\Gamma_4(A''_1)$	1	1	1	-1	-1	-1
$\Gamma_5(A''_2)$	1	1	-1	-1	-1	1
$\Gamma_6(E'')$	2	-1	0	-2	1	0

Table C.3: Character table of the D_{2h}^7 space group. Monolayer BP belongs to this symmetry group. By $\boldsymbol{\tau}_x = \boldsymbol{\tau}_{xz} = \boldsymbol{\tau}_z = 0$, we can directly apply this character table for D_{2h} point group to which strain-induced graphene belongs.

	$\{E 0\}$	$\{C_{2x}(z=1/4) \boldsymbol{\tau}_x^{(1)}\}$	$\{C_{2y}(x=z=1/4) 0\}$	$\{C_{2z} 0\}$	$\{i 0\}$	$\{\sigma_{xy} 0\}$	$\{\sigma_{xz} \boldsymbol{\tau}_{xz}^{(2)}\}$	$\{\sigma_{yz}(x=1/4) \boldsymbol{\tau}_z^{(3)}\}$
$\Gamma_1^+(A_g)$	1	1	1	1	1	1	1	1
$\Gamma_2^+(B_{1g})$	1	1	-1	-1	1	-1	-1	1
$\Gamma_3^+(B_{2g})$	1	-1	1	-1	1	-1	1	-1
$\Gamma_4^+(B_{3g})$	1	-1	-1	1	1	1	-1	-1
$\Gamma_1^-(A_u)$	1	1	1	1	-1	-1	-1	-1
$\Gamma_2^-(B_{1u})$	1	1	-1	-1	-1	1	1	-1
$\Gamma_3^-(B_{2u})$	1	-1	1	-1	-1	1	-1	1
$\Gamma_4^-(B_{3u})$	1	-1	-1	1	-1	-1	1	1

⁽¹⁾ $\boldsymbol{\tau}_x = \mathbf{a}_1/2$; ⁽²⁾ $\boldsymbol{\tau}_{xz} = (\mathbf{a}_1 + \mathbf{a}_3)/2$; ⁽³⁾ $\boldsymbol{\tau}_z = \mathbf{a}_3/2$, where \mathbf{a}_1 and \mathbf{a}_3 are the lattice vectors for x and z direction, respectively.

Table C.4: Character table of the C_{2h} point group. GaTe belongs to this symmetry group.

	E	$C_2(z)$	i	σ_h
Γ_1^+	1	1	1	1
Γ_1^+	1	-1	1	-1
Γ_1^+	1	1	-1	-1
Γ_1^+	1	-1	-1	1

Table C.5: Multiplication table of the D_{3h} and D_{6h} point group.

\otimes	Γ_1	Γ_2	Γ_3	Γ_4	Γ_5	Γ_6
Γ_1	Γ_1	Γ_2	Γ_3	Γ_4	Γ_5	Γ_6
Γ_2	Γ_2	Γ_1	Γ_4	Γ_3	Γ_5	Γ_6
Γ_3	Γ_3	Γ_4	Γ_1	Γ_2	Γ_6	Γ_5
Γ_4	Γ_4	Γ_3	Γ_2	Γ_1	Γ_6	Γ_5
Γ_5	Γ_5	Γ_5	Γ_6	Γ_6	$\Gamma_1 \oplus \Gamma_2 \oplus \Gamma_6$	$\Gamma_3 \oplus \Gamma_4 \oplus \Gamma_5$
Γ_6	Γ_6	Γ_6	Γ_5	Γ_5	$\Gamma_3 \oplus \Gamma_4 \oplus \Gamma_5$	$\Gamma_1 \oplus \Gamma_2 \oplus \Gamma_6$

Table C.6: Multiplication table for the basis between Γ_4 and Γ_5 of the D_{3h} and D_{6h} point group. $|i, j\rangle$ denotes the j -th eigen function of Γ_i symmetry

\otimes	$ 5, 1\rangle$	$ 5, 2\rangle$
$ 4, 1\rangle$	$ 6, 1\rangle$	$ 6, 2\rangle$

Table C.7: Multiplication table for the basis between Γ_1 , Γ_2 , Γ_6 , and Γ_6 of the D_{3h} and D_{6h} point group. $|i, j\rangle$ denotes the j -th eigen function of Γ_i symmetry

\otimes	$ 6, 1\rangle$	$ 6, 2\rangle$
$ 1, 1\rangle$	$ 6, 1\rangle$	$ 6, 2\rangle$
$ 2, 1\rangle$	$ 6, 1\rangle$	$ 6, 2\rangle$
$ 6, 1\rangle$	$ 6, 2\rangle$	$ 1, 1\rangle + 1, 2\rangle$
$ 6, 2\rangle$	$ 1, 1\rangle + 1, 2\rangle$	$ 6, 1\rangle$

Appendix D

Details of numerical calculations

Here we show the details of the parameters used in the numerical calculations in Chapters 3 and 5.

D.1 Optical absorption in TMDs (Chap. 3)

We perform the numerical calculation based on density functional theory (DFT) by using Quantum Espresso package¹¹⁷⁾ to calculate the electronic energy bands and the wave functions. We adopt ultrasoft pseudopotential (USPP) generated with a fully relativistic calculation including spin-orbit interaction in the DFT calculation. The exchange and correlation potential is described by the generalized gradient approximation (GGA) proposed by Perdew, Burke, and Ernzerhof (PBE)¹¹⁸⁾. The cut off energy is selected to be 50 Ry and we use $50 \times 45 \times 1$ grid for sample \mathbf{k} -points to calculate the optical absorption. We adopt a super cell for calculating monolayer TMD in which the size of the super cell in the calculation perpendicular to the layer is taken as $c/a = 10$ (a : lattice constant, c : interlayer distance) so that we can avoid the interlayer interaction.

The electron-photon matrix element $M_{\text{opt}}^{fi}(\mathbf{k})$ and the absorption coefficient $\alpha(E_L)$ is calculated by using Eqs. (2.39) and (2.55), respectively. We approximate the delta function in Eq. (2.55) as a Gaussian function $\frac{1}{\sqrt{2\pi}\gamma} \exp\left\{-\frac{(E_f - E_i - E_L)^2}{2\gamma^2}\right\}$ where γ is a broadening factor corresponding to a lifetime of the photo-excited electron. The value of γ affects the spectra line width of the optical absorption. Here we adopt the value of $\gamma = 0.03$ eV in our calculation. Though the γ value generally depends on E_L ,⁸²⁾ we assume that γ is a constant for simplicity.

D.2 Helicity-resolved Raman spectra (Chap. 5)

Electron-photon interaction

In order to obtain the electron-photon interaction given in Eq. (2.39), we calculate the wave functions based on the first-principles density functional theory (DFT) calculation by using **Quantum Espresso** package.¹¹⁷⁾ We use local density approximation (LDA) for the exchange-correlation functional in the norm-conserving pseudopotential. The wave function is described by the plane wave basis employed by the cutoff energy of 25 Ry. We use a $10 \times 10 \times 1$ Monkhorst-Pack k-mesh to sample a Brillouin zone for self consistent field (SCF) calculation. After the SCF calculation, we perform the non-SCF calculation for $51 \times 45 \times 1$ k-mesh without Monkhorst-Pack mesh and obtain the wave functions for 2295 sample K-points. To avoid the interlayer interaction for mono and bilayer structure, we construct a supercell with the lattice parameter of $c/a = 4$ (10) for graphene (MoS_2) where a and c are the lattice constant of in-plane and out-of-plane direction, respectively.

Electron-phonon interaction

We calculate the electron-phonon interaction by using EPW package⁸⁰⁾ which applies the maximally localized Wannier function (MLWF) combined with the phonon calculation at the Γ point by **Quantum Espresso** package.¹¹⁷⁾ The converging parameter for phonon calculation is more strict than the calculation for electronic energy band. We use the cut-off energy of 600, 240, and 400 Ry with $32 \times 32 \times 1$, $42 \times 42 \times 1$, and $48 \times 48 \times 1$ Monkhorst-pack sample K-mesh for graphene, monolayer, and bilayer MoS_2 , respectively. From EPW package, we extract the electron-phonon matrix elements of the $q = 0$ phonon for $51 \times 45 \times 1$ k-mesh in the first Brillouin zone and obtain the electron-phonon matrix elements for 2295 sample k-points.

Raman spectra calculation

The resonant Raman intensity for the first order scattering is calculated by Eq. (2.89). We assume the broadening factor γ for the resonant condition is constant and use $\gamma = 0.1$ eV from an estimated Raman excitation profile.¹¹⁹⁾ The delta function in Eq. (2.89) is approximated by Lorentzian curve $\frac{1}{\pi} \frac{\Gamma}{(E_L - (E_m - E_i))^2 + \Gamma^2}$ with the broadening factor Γ related with the life time of phonon. We use $\Gamma = 0.2$ (0.5) meV for MoS_2 (graphene). In the numerical calculation, in order to take into account the resonant condition in Eq. (2.89), we increase the number of the k -points to $201 \times 177 \times 1 = 35577$ points in the first Brillouin zone by employing the linear interpolation for

the electron-photon and electron-phonon matrix elements.

Appendix E

Program

In this chapter, we present the procedure of numerical calculation for the main results of this thesis and the detail of developed program in this work. In Table E.1, we show the procedure of the calculation for optical absorption and Raman spectra which is discussed in the main text. All our original programs used for the calculation in this thesis are putted in

tatsumi/for/program-opt/

in FLEX workstation. Hereafter we define this directory as ROOT/ for the explanation.

We prepare the example of the calculation of optical absorption and Raman spectra for monolayer MoS₂ in ROOT/example/mos2-1L/.

E.1 Electron-photon matrix element and optical absorption

The electron-photon matrix element and optical absorption is calculated in four steps: (1) SCF calculation, (2) NSCF calculation, (3) Output of wave function, and (4) calculation of matrix element and optical absorption. Step (1)-(3) is the part to obtain the wave function by using Quantum Espresso package and step (4) is the part to calculate the electron-photon matrix element by using original program. We note that process (3) is done twice if we calculate with considering spin-orbit interaction.

absorption.x

This program calculates electron-photon matrix elements and absorption spectra by wave functions obtained from first-principles calculation. We can compile and obtain absorption.x by make command.

```
# cd ROOT/absorption
```

Table E.1: Procedure of calculating optical absorption and Raman spectra using developed program.

	Command	Input Files	Output Files
1. Electron-photon matrix element			
1-1. SCF calculation	pw.x	scf.in	scf.out wfc.save/
1-2. NSCF calculation	pw.x	nscf.in wfc_save/	nscf.out wfc_save/
1-3. Output of wave function	pw_export.x	pw_export.in wfc.save/	index.xml
1-4. Calculation of absorption	absorption.x	absorption.in	absorption_outdata
2. Phonon			
2-1. SCF calculation	pw.x	scf.in	scf.out wfc_save/
2-2. Phonon calculation	ph.x	ph.in wfc_save/	ph.out _ph0/
2-3. Obtain input files of EPW	python	pp.py _ph0/	save/
3. Electron-phonon matrix element			
3-1. SCF calculation	pw.x	scf.in	scf.out wfc_save/
3-2. NSCF calculation	pw.x	nscf.in wfc_save/	nscf.out wfc_save/
3-3. EPW calculation	epw.x (modified)	epw.in wfc_save/	phabnd.dat ep_matele.dat save/
4. First-order resonant Raman spectra			
4-1. Raman calculation	raman.x	raman.in index.xml ep_matele.dat phband.dat	raman.out raman_outdata

```
# make
```

& main

input_type : CHARACTER

DEFAULT: 'pw_export'

File type of input file of wave function.

'pw_export': index.xml file obtained from pw_export calculation by Quantum Espresso

'arrange_binary': binary file to decrease reading time of input file

calctype : CHARACTER

DEFAULT: 'absorption'

Calculation type. Please choose the job:

'absorption': Calculate the absorption spectra. 'make_input_binary': Make the new input file in binary style by reading index.xml file. in order to decrease the file size and get the faster reading time of input file. Only one file is generated even when spinorb = .TRUE.

'absorption_el': Calculate the degree of valley polarization and valley polarized intensity of optical transition. This calculation is only for hexagonal lattice.

'poldep': Calculate the polar plot of electron-photon matrix element.

outfil_arr_input : CHARACTER

DEFAULT: index_binary.dat

The name of generated binary input file of wave function

spinorb : LOGICAL

DEFAULT: .FALSE.

Set .TRUE. if the calculation considers the spin-orbit interaction. We need two file (up and down spin) for input file of wave function.

circular_pol : LOGICAL

DEFAULT: .FALSE.
.TRUE. if we calculate the absorption for circular polarized light.

& pwfn

input_pw_export1 : CHARACTER

DEFAULT:
File name of input file of wave function for the case if you use undex.xml file generated by pw_export calculation.

input_pw_export2 : CHARACTER

DEFAULT:
Second file of input file of wave function only when circular_pol = .TRUE.

input_data_arr : CHARACTER

DEFAULT:
File name of input file of wave function when we use generated binary file.

n_bi : INTEGER

DEFAULT: 1
Number of valence band in SCF and NSCF calculation by Quantum Espresso.

bi_start : CHARACTER

DEFAULT: 1
The band index for minimum energy bands in this calculation. The energy bands with index smaller than bi_start are not considered in the calculation.

fit_func : CHARACTER

DEFAULT: 'lorentzian'

Function to approximate the delta function in Fermi's golden rule.

'lorentzian'

'gaussian'

gamma : INTEGER

DEFAULT: 0.03D0

Broadening factor of gaussian or lorentzian which approximates delta function in Fermi's golden rule.

unitcell_type : INTEGER

DEFAULT: 4

Parameter for evaluating absorption coefficient (nm^{-1}) in 2D materials. We have to evaluate the volume of unit cell to calculate the absorption coefficient [see Eq. (2.55)]. Then for 2D material, we use the volume of bulk material.0: Bulk 1: 1L-BP 2: 2L-BP 3: 3L-BP 4: 1L-MoS₂ 5: 1L-MoSe₂ 6: 1L-MoTe₂ 7: 1L-WS₂ 8:1L-WSe₂ 8:1L-WTe₂*Exapmle for monolayer MoS₂*

Move to work directory.

```
# cd ROOT/example/mos2-1L/absorption/scf/
```

SCF calculation

```
# pw.x < scf.in > scf.out
```

NSCF calculation

```
# pw.x < nscf.in > nscf.out
```

The pw_export calculation for spin up state

```
# pw_export.x < pw_export.in > pw_export.out
```

Change the name of output file for spin up state

```
# mv ./wfc_save/mos2-1L.export/index.xml ./wfc_save/mos2-1L.export/index_ispin=1.xml
```

The `pw_export.x` makes output only for spin up state by reading only `./wfc_save/mos2-1L.save/K****/evc1.dat`. Then we exchange the name of `evc1.dat` and `evc2.dat` by shell script.

```
# cp ./fa.sh ./wfc_save/mos2-1L.save/
```

```
# cd ./wfc_save/mos2-1L.save/
```

```
# ./fa.sh
```

```
# ../../
```

Then, run `pw_expot.x` again for spin down state and change the name of output file.

```
# pw_export.x < pw_export.in > pw_export.out
```

```
# mv ./wfc_save/mos2-1L.export/index.xml ./wfc_save/mos2-1L.export/index_ispin=2.xml
```

The two files (`index_ispin=1.xml` and `index_ispin=2.xml`) including the information of wave function are input of the calculation of optical absorption.

Finally, move to working directory and run the calculation for optical absorption.

```
# cd ../absorption/
```

```
# ROOT/absorption/absorption.x < absorption.in > absorption.out
```

E.2 Phonon

Phonon calculation for getting electron-phonon matrix element is executed by using `pw.x` and `ph.x` in Quantum Espresso. Calculation is only for $\mathbf{q} = 0$ phonon for first-order Raman spectra. After finishing phonon calculation, we generate the input files for electron-phonon calculation by EPW package by python file “pp.py”.

Exapmle for monolayer MoS₂

Move to work directory.

```
# cd ROOT/example/mos2-1L/raman/phonon/
```

SCF calculation.

```
# pw.x < scf.in > scf.out
```

Phonon calculation.

```
# ph.x < ph.in > ph.out
```

Generate the input files for the calculation of electron-phonon matrix element by modified EPW package.

```
# python pp.py
Enter the prefix used for PH calculation (e.g. diam)
mos2-1L
Enter the number of irreducible q-points
1
```

Generated save/ directory becomes input file in the calculation of electron-phonon matrix element.

E.3 Electron-phonon matrix element

The calculation for the electron-phonon matrix element is done in 3 steps: (1) SCF calculation, (2) NSCF calculation, (3) calculation of electron-phonon matrix element by modified EPW package. EPW is the program basically for the calculation of superconductivity. EPW calculates the electron-phonon matrix element in the process. However there was not output of electron-phonon matrix element. (new variable for the output of electron-phonon matrix element is implemented from EPW version 4.3. We plan to update our original program to read the output of latest EPW.) Thus we modify the source code of EPW and extract the information of Γ point phonon in the file of “ep_matele.dat”.

Example for monolayer MoS₂

This calculation should be executed after phonon calculation and obtain the save/ directory.

Move to work directory.

```
# cd ROOT/example/mos2-1L/raman/epw/
```

SCF calculation.

```
# pw.x < scf.in > scf.out
```

NSCF calculation.

```
# pw.x < nscf.in > nscf.out
```

EPW calculation. Be careful that epw.x is not default execution file, but the file compiled with the modification to output the electron-phonon matrix element. Modified epw.x is putted in ROOT/raman/ or we can obtain modified epw.x by replacing selfen_elec.f90 file of default EPW to ROOT/raman/selfen_elec.f90. Set the variable in epw.in as elecselfen = .TRUE., parallel_k = .TRUE., and parallel_q = .FALSE.

```
# ROOT/raman/epw.x < epw.in > epw.out
```

We obtain the output file ep_matele.dat and phband.freq which are the input file in the calculation of Raman spectra.

E.4 First-order resonant Raman spectra

Using the output of the wave function and electron-phonon matrix element, our original program “raman.x” calculate the first-order Raman intensity for linearly or circularly polarized light.

raman.x

This program calculates Raman spectra, using electron-photon and electron-phonon matrix elements obtained by first-principles calculation. We can compile and obtain raman.x by make command.

```
# cd ROOT/raman
```

```
# make
```

outdir : CHARACTER

DEFAULT: 'outdata'

Directory name of output files.

circular_pol : LOGICAL

DEFAULT: .FALSE.

If .TRUE., Raman spectra for circular polarized light is calculated.

nonpol : LOGICAL

DEFAULT: .FALSE.

If .TRUE., Raman spectra for non-polarized light is calculated.

input_pw_export : CHARACTER

DEFAULT: ./index.xml

File name of wave function calculated by Quantum Espresso (Output of pw_export.x).

fil_phband : CHARACTER

DEFAULT: 'phband.freq'

File name of phonon frequency calculated by modified EPW.

fil_matele_elph : CHARACTER

DEFAULT: 'ep_matele.dat'

File name of electron-phonon matrix element calculated by modified EPW.

gamma : REAL(8)

DEFAULT: 0.1D0

Broadening factor of resonance condition γ (eV).**gamma_raman : REAL(8)**

DEFAULT: 0.00005D0

Broadening factor of Raman spectra Γ (eV).**elaser1 : REAL(8)**

DEFAULT: 0.1D0

Laser energy (eV).

elaser2, elaser3, elaser4, elaser5, elaser6, elaser7 : REAL(8)

We can calculate up to 7 laser energy in one calculation.

nbv : INTEGER

DEFAULT: 1

Number of valence bands after Wannier interpolation in EPW calculation.

nscf_occ : INTEGER

DEFAULT: 1

Number of valence bands calculated in Quantum Espresso.

nqs : INTEGER

DEFAULT: 1

Number of phonon q points. Please use 1 for current version (calculation is only for first-order Raman spectra).

nmode : INTEGER

DEFAULT: 1

Number of phonon modes.

nel : INTEGER

DEFAULT: 1

Number of calculated laser energies.

nrs : INTEGER

DEFAULT: 500

Number of calculated points of Raman shift.

n_kinterp : INTEGER

DEFAULT: 0

Matrix elements are linearly interpolated. The number of calculated k points, respectively, becomes $n_k \times n_k$, $(2n_k - 1) \times (2n_k - 1)$, $2(2n_k - 1) - 1 \times 2(2n_k - 1) - 1$, ... when we use $n_k \times n_k$ mesh to calculate the matrix elements and $n_kinterp = 0, 1, 2, \dots$

rs_start : REAL(8)

DEFAULT: 0.0D0

Region of calculated Raman shift from rs_start to rs_end (eV).

rs_end : REAL(8)

DEFAULT: 0.01D0

Region of calculated Raman shift from rs_start to rs_end (eV).

plot_matele_elph : LOGICAL

DEFAULT: .FALSE.

3D plot of electron-phonon matrix element.

plot_matele_opt : LOGICAL

DEFAULT: .FALSE.

3D plot of electron-photon matrix element.

plot_raman_k : LOGICAL

DEFAULT: .FALSE.

3D plot of Raman matrix element.

Example for monolayer MoS₂

This calculation should be executed after obtaining the input files of electron-phonon matrix element `ep_matele.dat` and `phband.freq`.

Generate the index.xml file which includes the information of wave function by similar way of the calculation of optical absorption.

```
# cd ROOT/example/mos2-1L/raman/scf/
```

```
# pw.x < scf.in > scf.out
```

```
# pw.x < nscf.in > nscf.out
```

```
# pw_export.x < pw_export.in > pw_export.out
```

Calculation of Raman spectra

```
# ROOT/raman/raman.x < raman.in > raman.out
```

Publication list

1. X. Ling, S. Huang, E.H. Hasdeo, L. Liang, W.M. Parkin, **Y. Tatsumi**, A.R.T. Nugraha, A.A. Puzos, P.M. Das, B.G. Sumpter, D.B. Geohegan, J. Kong, R. Saito, M. Drndic, V.Meunier, and M.S. Dresselhaus: “Anisotropic Electron-phonon and electron-phonon interactions in Black Phosphorus”, *Nano Lett.* 16, 2260 (2016).
2. R. Saito, **Y. Tatsumi**, S.Huang, X. Ling, and M. S. Dresselhaus: “Raman spectroscopy of transition metal dichalcogenides”, *J. Phys.: Condens. Matter* 28, 353002 (2016).
3. S. Huang, **Y. Tatsumi**, X. Ling, H. Guo, Z. Wang, G. Watson, A.A. Puzos, D.B. Geohegan, J. Kong, J. Li, T. Yang, R. Saito, and M.S. Dresselhaus: “In-Plane Optical Anisotropy of Layered Gallium Telluride” *ACS Nano* 10, 8964 (2016).
4. **Y. Tatsumi**, K. Ghalamkari, and R. Saito: “Laser energy dependence of valley polarization in transition metal dichalcogenides”, *Phys. Rev. B* 94, 235408 (2016).
5. N. Sato, **Y. Tatsumi**, and R. Saito: “Circular dichroism of single-wall carbon nanotubes”, *Phys. Rev. B* 95, 155436 (2017).
6. L. Zhou, S. Huang, **Y. Tatsumi**, L. Wu, H. Guo, Y.-Q. Bie, K. Ueno, T. Yang, Y. Zhu, J. Kong, R. Saito, and M. Dresselhaus: “Sensitive Phonon-Based Probe for Structure Identification of 1T’ MoTe₂”, *J. Am. Chem. Soc.* 139, 8396 (2017)

Conferences

Oral presentation

1. Yuki Tatsumi and Riichiro Saito: “Laser energy dependence of valley polarization in transition metal dichalcogenides”, Japan Physical Society 71th Annual Meeting, Tohoku-Gakuin University, Sendai, Miyagi (2016.03.22).
2. Yuki Tatsumi: “右巻きと左巻きの使い方 -光バレー トロニクスに向けて-”, Science and Life Science Joint Symposium 2017, Tohoku University, Sendai, Miyagi (2017.02.17)

Poster presentations

1. Yuki Tatsumi, Wataru Izumida and Riichiro Saito : “Vernier spectrum in finite-length armchair carbon nanotubes”, The 44th Fullerenes-Nanotubes-Graphene General symposium, The University of Tokyo, Tokyo (2013.03.13).
2. Yuki Tatsumi, Pourya Ayria, Huaihong Guo, Teng Yang and Riichiro Saito : “Anisotropy of optical absorption spectrum of phosphorene”, The 44th Fullerenes-Nanotubes-Graphene General symposium, Kitakyusyu International Conference Center, Kitakyusyu, Hukuoka (2015.09.09).
3. Yuki Tatsumi, Shengxi Huang, Xi Ling, Huaihong Guo, Teng Yang, Mildred S. Dresselhaus and Riichiro Saito : “Anisotropic optical absorption and Raman spectrum in GaTe”, The 50th Fullerenes-Nanotubes-Graphene General symposium, The University of Tokyo, Tokyo (2016.02.20).
4. Yuki Tatsumi, Shengxi Huang, Xi Ling, Huaihong Guo, Teng Yang, Mildred S. Dresselhaus and Riichiro Saito : “Anisotropic optical absorption and Raman spectra in GaTe with the interference effect of the substrates”, The 51th

- Fullerenes-Nanotubes-Graphene General symposium, Hokkaido Citizens Actives Center Kaderu 2·7, Sapporo, Hokkaido (2016.9.08).
5. Yuki Tatsumi and Riichiro Saito : “Laser energy dependence of the valley polarization in transition metal dichalcogenides”, 7th A3 Symposium on Emerging Materials : Nanomaterials for Electronics, Energy and Environment, Lotte Buyeo Resort, Baekjemun-ro, Gyuan-myeon, Buyeo-gun, Chungcheongnam-do, Korea (2016.11.03).
 6. Yuki Tatsumi and Riichiro Saito : “Helicity-resolved first order resonant Raman spectra of graphene and transition metal dichalcogenides”,The 52th Fullerenes-Nanotubes-Graphene General symposium, The University of Tokyo, Tokyo (2017.03.01).
 7. Yuki Tatsumi and Riichiro Saito : “Chiral phonon modes in the first order Raman spectra for transition metal dichalcogenides and strain-induced graphene”, 18th International Conference on the Science and Application of Nanotubes and Low-dimensional Materials (NT17), Belo Horizonte, Brazil (2017.06.27)

Bibliography

- [1] K.S. Novoselov, A.K. Geim, S.V. Morozov, D. Jiang, Y. Zhang, S.V. Dubonos, I.V. Grigorieva, A.A. Firsov, *Science* **306**, 666 (2004)
- [2] L. Britnell, R.M. Ribeiro, A. Eckmann, R. Jalil, B.D. Belle, A. Mishchenko, Y.J. Kim, R.V. Gorbachev, T. Georgiou, S.V. Morozov, A.N. Grigorenko, A.K. Geim, C. Casiraghi, A.H.C. Neto, K.S. Novoselov, *Science* **340**(6138), 1311 (2013)
- [3] O. Lopez-Sanchez, D. Lembke, M. Kayci, A. Radenovic, A. Kis, *Nat. Nanotechnol.* **8**, 497 (2013)
- [4] F. Wang, Z. Wang, K. Xu, F. Wang, Q. Wang, Y. Huang, L. Yin, J. He, *Nano Lett.* **15**(11), 7558 (2015)
- [5] R. Cheng, D. Li, H. Zhou, C. Wang, A. Yin, S. Jiang, Y. Liu, Y. Chen, Y. Huang, X. Duan, *Nano Lett.* **14**(10), 5590 (2014)
- [6] H.S. Lee, S.W. Min, Y.G. Chang, M.K. Park, T. Nam, H. Kim, J.H. Kim, S. Ryu, S. Im, *Nano Lett.* **12**(7), 3695 (2012)
- [7] Z. Yin, H. Li, H. Li, L. Jiang, Y. Shi, Y. Sun, G. Lu, Q. Zhang, X. Chen, H. Zhang, *ACS Nano* **6**(1), 74 (2012)
- [8] J.S. Ross, P. Klement, A.M. Jones, N.J. Ghimire, J. Yan, D.G. Mandrus, T. Taniguchi, K. Watanabe, K. Kitamura, W. Yao, D.H. Cobden, X. Xu, *Nat. Nanotechnol.* **9**, 268 (2014)
- [9] H.Z. Lu, W. Yao, D. Xiao, S.Q. Shen, *Phys. Rev. Lett.* **110**, 016806 (2013)
- [10] G. Berghäuser, E. Malic, *Phys. Rev. B* **89**, 125309 (2014)
- [11] K.F. Mak, K. He, J. Shan, T.F. Heinz, *Nat. Nanotechnol.* **7**, 494 (2012)
- [12] K.F. Mak, K. He, C. Lee, G.H. Lee, J. Hone, T.F. Heinz, J. Shan, *Nat. Mater.* **12**, 207 (2013)

- [13] H. Zeng, J. Dai, W. Yao, D. Xiao, X. Cui, *Nat. Nanotechnol.* **7**, 490 (2012)
- [14] T. Cao, G. Wang, W. Han, H. Ye, C. Zhu, J. Shi, Q. Niu, P. Tan, E. Wang, B. Liu, J. Feng, *Nat. Commun.* **3**, 887 (2012)
- [15] A.M. Jones, H. Yu, N.J. Ghimire, S. Wu, G. Aivazian, J.S. Ross, B. Zhao, J. Yan, D.G. Mandrus, D. Xiao, W. Yao, X. Xu, *Nat. Nanotechnol.* **8**, 634 (2013)
- [16] S. Wu, J.S. Ross, G.B. Liu, G. Aivazian, A. Jones, Z. Fei, W. Zhu, D. Xiao, W. Yao, D. Cobden, X. Xu, *Nat. Phys.* **9**, 149 (2013)
- [17] R. Suzuki, M. Sakano, Y.J. Zhang, R. Akashi, D. Morikawa, A. Harasawa, K. Yaji, K. Kuroda, K. Miyamoto, T. Okuda, K. Ishizaka, R. Arita, Y. Iwasa, *Nat. Nanotechnol.* **9**, 611 (2014)
- [18] W.T. Hsu, Y.L. Chen, C.H. Chen, P.S. Liu, T.H. Hou, L.J. Li, W.H. Chang, *Nat. Commun.* **6**, 8963 (2015)
- [19] T. Yan, X. Qiao, P. Tan, X. Zhang, *Sci. Rep.* **5**, 15625 (2015)
- [20] G. Aivazian, Z. Gong, A.M. Jones, R.L. Chu, J. Yan, D.G. Mandrus, C. Zhang, D. Cobden, W. Yao, X. Xu, *Nat. Phys.* **11**, 148 (2015)
- [21] K. Hao, G. Moody, F. Wu, C.K. Dass, L. Xu, C.H. Chen, L. Sun, M.Y. Li, L.J. Li, A.H. MacDonald, X. Li, *Nat. Phys.* **12**, 677 (2016)
- [22] J. Huang, T.B. Hoang, M.H. Mikkelsen, *Sci. Rep.* **6**, 22414 (2016)
- [23] T. Smoleński, M. Goryca, M. Koperski, C. Faugeras, T. Kazimierczuk, A. Bogucki, K. Nogajewski, P. Kossacki, M. Potemski, *Phys. Rev. X* **6**, 021024 (2016)
- [24] E.J. Sie, J.W. McIver, Y.H. Lee, L. Fu, J. Kong, N. Gedik, *Nat. Mater.* **14**, 290 (2015)
- [25] Y.J. Zhang, T. Oka, R. Suzuki, J.T. Ye, Y. Iwasa, *Science* **344**(6185), 725 (2014)
- [26] S.Y. Chen, C. Zheng, M.S. Fuhrer, J. Yan, *Nano Lett.* **15**(4), 2526 (2015), PMID: 25719859
- [27] A. Splendiani, L. Sun, Y. Zhang, T. Li, J. Kim, C.Y. Chim, G. Galli, F. Wang, *Nano Lett.* **10**(4), 1271 (2010)

- [28] K.F. Mak, C. Lee, J. Hone, J. Shan, T.F. Heinz, *Phys. Rev. Lett.* **105**, 136805 (2010)
- [29] K.K. Kam, B.A. Parkinson, *J. Phys. Chem.* **86**(4), 463 (1982)
- [30] T. Böker, R. Severin, A. Müller, C. Janowitz, R. Manzke, D. Voß, A.M. P. Krüger, J. Pollmann, *Phys. Rev. B* **64**, 235305 (2001)
- [31] Y. Zhang, T.R. Chang, B. Zhou, Y.T. Cui, H. Yan, Z. Liu, F. Schmitt, J. Lee, R. Moore, Y. Chen, H. Lin, H.T. Jeng, S.K. Mo, Z. Hussain, A. Bansil, Z.X. Shen, *Nat. Nanotechnol.* **9**, 111 (2014)
- [32] C. Ruppert, O.B. Aslan, T.F. Heinz, *Nano Lett.* **14**(11), 6231 (2014)
- [33] W. Zhao, Z. Ghorannevis, L. Chu, M. Toh, C. Kloc, P.H. Tan, G. Eda, *ACS Nano* **7**(1), 791 (2013)
- [34] A. Castellanos-Gomez, L. Vicarelli, E. Prada, J.O. Island, K.L. Narasimha-Acharya, S.I. Blanter, D.J. Groenendijk, M. Buscema, G.A. Steele, J.V. Alvarez, *2D Mater.* **1**, 025001 (2014)
- [35] R.W. Keyes, *Phys. Rev.* **92**, 580 (1953)
- [36] D. Warschauer, *J. Appl. Phys.* **34**, 1853 (1963)
- [37] A. Yamamoto, A. Syouji, T. Goto, E. Kulatov, K. Ohno, Y. Kawazoe, K. Uchida, N. Miura, *Phys. Rev. B* **64**, 035210 (2001)
- [38] G. Long, D. Maryenko, J. Shen, S. Xu, J. Hou, Z. Wu, W.K. Wong, T. Han, J. Lin, Y. Cai, R. Lortz, N. Wang, *Nano Letters* **16**(12), 7768 (2016), pMID: 27960491
- [39] D. Sun, G. Aivazian, A.M. Jones, J.S. Ross, W. Yao, D. Cobden, X. Xu, *Nat. Nanotechnol.* **7**, 114 (2012)
- [40] W. Choi, M.Y. Cho, A. Konar, J.H. Lee, G.B. Cha, S.C. Hong, S. Kim, J. Kim, D. Jena, J. Joo, S. Kim, *Adv. Mater.* **24**, 5832 (2012)
- [41] N. Perea-Lopez, A.L. Elias, A. Berkdemir, A. Castro-Beltran, H.R. Gutierrez, S. Feng, R. Lv, T. Hayashi, F. Lopez-Urias, S. Ghosh, B. Muchharla, S. Talapatra, H. Terrones, M. Terrones, *Adv. Funct. Mater.* **23**(44), 5511 (2013)

- [42] P. Hu, J. Zhang, M. Yoon, X.F. Qiao, X. Zhang, W. Feng, P. Tan, W. Zheng, J. Liu, X. Wang, J.C. Idrobo, D.B. Geohegan, K. Xiao, *Nano Res.* **7**(5), 694 (2014)
- [43] F. Liu, H. Shimotani, H. Shang, T. Kanagasekaran, V. Zólyomi, N. Drummond, V.I. Fal'ko, K. Tanigaki, *ACS Nano* **8**(1), 752 (2014)
- [44] J. Ribeiro-Soares, R.M. Almeida, L.G. Cançado, M.S. Dresselhaus, A. Jorio, *Phys. Rev. B* **91**, 205421 (2015)
- [45] F. Xia, H. Wang, Y. Jia, *Nat. Commun.* **5**, 4458 (2014)
- [46] A. Jain, A.J.H. McGaughey, *Sci Rep.* **5**, 8501 (2015)
- [47] H. Yuan, X. Liu, F. Afshinmanesh, W. Li, G. Xu, J. Sun, B. Lian, A.G. Curto, G. Ye, Y. Hikita, Z. Shen, S.C. Zhang, X. Chen, M. Brongersma, H.Y. Hwang, Y. Cui, *Nat. Nanotechnol.* **10**, 707 (2015)
- [48] T. Low, A.S. Rodin, A. Carvalho, Y. Jiang, H. Wang, F. Xia, A.H.C. Neto, *Phys. Rev. B* **90**, 075434 (2014)
- [49] V. Tran, R. Soklaski, Y. Liang, L. Yang, *Phys. Rev. B* **89**, 235319 (2014)
- [50] S. Yuan, A.N. Rudenko, M.I. Katsnelson, *Phys. Rev. B* **91**(11), 115436 (2015)
- [51] J. Kim, J.U. Lee, J. Lee, H.J. Park, Z. Lee, C. Lee, H. Cheong, *Nanoscale* **7**, 18708 (2015)
- [52] X. Ling, L. Liang, S. Huang, A.A. Puretzky, D.B. Geohegan, B.G. Sumpter, J. Kong, V. Meunier, M.S. Dresselhaus, *Nano Lett.* **15**(6), 4080 (2015)
- [53] H.B. Ribeiro, M.A. Pimenta, C.J.S. de Matos, R.L. Moreira, A.S. Rodin, J.D. Zapata, E.A.T. de Souza, A.H.C. Neto, *ACS Nano* **9**(4), 4270 (2015)
- [54] S. Huang, Y. Tatsumi, X. Ling, H. Guo, Z. Wang, G. Watson, A.A. Puretzky, D.B. Geohegan, J. Kong, J. Li, T. Yang, R. Saito, M.S. Dresselhaus, *ACS Nano* **10**(9), 8964 (2016), pMID: 27529802
- [55] W. Yao, D. Xiao, Q. Niu, *Phys. Rev. B* **77**, 235406 (2008)
- [56] Z.Y. Zhu, Y.C. Cheng, U. Schwingenschlögl, *Phys. Rev. B* **84**, 153402 (2011)
- [57] D. Xiao, G.B.L. nad Wanxiang Feng, X. Xu, W. Yao, *Phys. Rev. Lett.* **108**, 196802 (2012)

- [58] G.B. Liu, W.Y. Shan, Y. Yao, W. Yao, D. Xiao, Phys. Rev. B **88**, 085433 (2013)
- [59] K. Kořmider, J.W. González, J. Fernández-Rossier, Phys. Rev. B **88**, 245436 (2013)
- [60] A. Kormányos, V. Zólyomi, N.D. Drummond, G. Burkard, Phys. Rev. X **4**, 011034 (2014)
- [61] R. Roldán, M.P. López-Sancho, F. Guinea, E. Cappelluti, J.A. Silva-Guillén, P. Ordejón, 2D Mater. **1**, 034003 (2014)
- [62] A. Carvalho, R.M. Ribeiro, A.H. Castro Neto, Phys. Rev. B **88**, 115205 (2013)
- [63] D. Kozawa, R. Kumar, A. Carvalho, K.K. Amara, W. Zhao, S. Wang, M. Toh, R.M. Ribeiro, A.H.C. Neto, K. Matsuda, G. Eda, Nat. Commun. **5**, 4543 (2014)
- [64] M. Selig, G. Berghäuser, A. Raja, P. Nagler, C. Schüller, T.F. Heinz, T. Korn, A. Chernikov, E. Malic, A. Knorr, Nat. Commun. **7**, 13279 (2016)
- [65] L. Malard, M. Pimenta, G. Dresselhaus, M. Dresselhaus, Physics Reports **473**, 51 (2009)
- [66] E.H. Hasdeo, A.R.T. Nugraha, M.S. Dresselhaus, R. Saito, Phys. Rev. B **94**, 075104 (2016)
- [67] P.H. Tan (ed.), *Raman Spectroscopy of Two-Dimensional Materials* (Springer, In Press)
- [68] J. Maultzsch, S. Reich, C. Thomsen, H. Requardt, P. Ordejón, Phys. Rev. Lett. **92**, 075501 (2004)
- [69] M. Mohr, J. Maultzsch, E. Dobardžić, S. Reich, I. Milošević, M. Damnjanović, A. Bosak, M. Krisch, C. Thomsen, Phys. Rev. B **76**, 035439 (2007)
- [70] R. Saito, Y. Tatsumi, S. Huang, X. Ling, M.S. Dresselhaus, J. Phys.: Condens. Matter **28**(35), 353002 (2016)
- [71] X. Ling, S. Huang, E.H. Hasdeo, L. Liang, W.M. Parkin, Y. Tatsumi, A.R.T. Nugraha, A.A. Puretzky, P.M. Das, B.G. Sumpter, D.B. Geohegan, J. Kong, R. Saito, M. Drndić, V. Meunier, M.S. Dresselhaus, Nano Lett. **16**(0), 2260 (2016), pMID: 26963685
- [72] R. Loudon, Advan. Phys. **13**, 423 (1964)

- [73] K.Y. Bliokh, F. Nori, *Physics Reports* **592**, 1 (2015)
- [74] K.Y. Bliokh, F.J. Rodríguez-Fortuño, F. Nori, A.V. Zayats, *Nature Photonics* **9**, 796 (2015)
- [75] L. Zhang, Q. Niu, *Phys. Rev. Lett.* **115**, 115502 (2015)
- [76] K.Y. Bliokh, M.A. Alonso, E.A. Ostrovskaya, A. Aiello, *Phys. Rev. A* **82**, 063825 (2010)
- [77] L. Zhang, Q. Niu, *Phys. Rev. Lett.* **112**, 085503 (2014)
- [78] A. Grüneis, R. Saito, G.G. Samsonidze, T. Kimura, M.A. Pimenta, A. Jorio, A.G.S. Filho, G. Dresselhaus, M.S. Dresselhaus, *Phys. Rev. B* **67**(16), 165402 (2003)
- [79] S. Baroni, S. de Gironcoli, A.D. Corso, P. Giannozzi, *Rev. Mod. Phys.* **73**, 515 (2001)
- [80] J. Noffsinger, F. Giustino, B.D. Malone, C.H. Park, S.G. Louie, M.L. Cohen, *Computer Physics Communications* **181**, 2140 (2010)
- [81] J. Jiang, R. Saito, A. Gruneis, G. Dresselhaus, M. Dresselhaus, *Chemical Physics Letters* **392**(4), 383 (2004)
- [82] A. Jorio, M.S. Dresselhaus, R. Saito, G. Dresselhaus, *Raman Spectroscopy in Graphene-Related Systems* (Wiley, New York, 2011)
- [83] Y.M. Koroteev, G. Bihlmayer, J.E. Gayone, E.V. Chulkov, S. Blügel, P.M. Echenique, P. Hofmann, *Phys. Rev. Lett.* **93**, 046403 (2004)
- [84] E. Cappelluti, R. Roldán, J.A. Silva-Guillén, P. Ordejón, F. Guinea, *Phys. Rev. B* **88**, 075409 (2013)
- [85] S. Fang, R. Kuate Defo, S.N. Shirodkar, S. Lieu, G.A. Tritsarlis, E. Kaxiras, *Phys. Rev. B* **92**, 205108 (2015)
- [86] J.C. Slater, G.F. Koster, *Phys. Rev.* **94**(6), 1498 (1954)
- [87] R. Saito, A. Grüneis, G.G. Samsonidze, G. Dresselhaus, M.S. Dresselhaus, A. Jorio, L.G. Cançado, M.A. Pimenta, A.G.S. Filho, *Appl. Phys. A* **78**(8), 1099 (2004)
- [88] H. Jiang, *J. Phys. Chem. C* **116**(14), 7664 (2012)
- [89] H. Shi, H. Pan, Y.W. Zhang, B.I. Yakobson, *Phys. Rev. B* **87**, 155304 (2013)

- [90] T. Cheiwchanchamnangij, W.R.L. Lambrecht, *Phys. Rev. B* **85**, 205302 (2012)
- [91] W.B. Pearson, *Acta Crystallographica* **17**(1), 1 (1964)
- [92] J. Camassel, H.M. P. Merle, *Physica B+C* **99**, 309 (1980)
- [93] J.F. Sánchez-Royo, J. Pellicer-Porres, A. Segura, V. Muñoz-Sanjosé, G. Tobías, P. Ordejón, E. Canadell, Y. Huttel, *Phys. Rev. B* **65**, 115201 (2002)
- [94] I.H. Malitson, *J. Opt. Soc. Am.* **55**(10), 1205 (1965)
- [95] G. Vuye, S. Fisson, V.N. Van, Y. Wang, J. Rivory, F. Abeles, *Thin Solid Films* **233**(1), 166 (1993)
- [96] M. Lazzeri, F. Mauri, *Phys. Rev. Lett.* **90**, 036401 (2003)
- [97] S.L. Li, H. Miyazaki, H. Song, H. Kuramochi, S. Nakaharai, K. Tsukagoshi, *ACS Nano* **6**(8), 7381 (2012), pMID: 22838842
- [98] D. Yoon, H. Moon, Y.W. Son, J.S. Choi, B.H. Park, Y.H. Cha, Y.D. Kim, H. Cheong, *Phys. Rev. B* **80**, 125422 (2009)
- [99] Y.Y. Wang, Z.H. Ni, Z.X. Shen, H.M. Wang, Y.H. Wu, *Appl. Phys. Lett.* **92**(4), 043121 (2008)
- [100] C. Lee, H. Yan, L.E. Brus, T.F. Heinz, J. Hone, S. Ryu, *ACS Nano* **4**(5), 2695 (2010), pMID: 20392077
- [101] H. Li, Q. Zhang, C.C.R. Yap, B.K. Tay, T.H.T. Edwin, A. Olivier, D. Baillargeat, *Adv. Funct. Mater.* **22**, 1385 (2012)
- [102] L. Sun, J. Yan, D. Zhan, L. Liu, H. Hu, H. Li, B.K. Tay, J.L. Kuo, C.C. Huang, D.W. Hewak, P.S. Lee, Z.X. Shen, *Phys. Rev. Lett.* **111**, 126801 (2013)
- [103] H.L. Liu, H. Guo, T. Yang, Z. Zhang, Y. Kumamoto, C.C. Shen, Y.T. Hsu, L.J. Li, R. Saito, S. Kawata, *Phys. Chem. Chem. Phys.* **17**, 14561 (2015)
- [104] M.A. Pimenta, E. del Corro, B.R. Carvalho, C. Fantini, L.M. Malard, *Accounts of Chemical Research* **48**(1), 41 (2015), pMID: 25490518
- [105] A.A. Mostofi, J.R. Yates, Y.S. Lee, I. Souza, D. Vanderbilt, N. Marzari, *Computer Physics Communications* **178**(9), 685 (2008)

- [106] Y. Zhao, X. Luo, H. Li, J. Zhang, P.T. Araujo, C.K. Gan, J. Wu, H. Zhang, S.Y. Quek, M.S. Dresselhaus, Q. Xiong, *Nano Lett.* **13**(3), 1007 (2013), pMID: 23432683
- [107] Y. Tatsumi, K. Ghalamkari, R. Saito, *Phys. Rev. B* **94**, 235408 (2016)
- [108] H.P.C. Miranda, S. Reichardt, G. Froehlicher, A. Molina-Sanchez, S. Berciaud, L. Wirtz, *Nano Lett.* **17**(4), 2381 (2017), pMID: 28199122
- [109] S.G. Drapcho, J. Kim, X. Hong, C. Jin, S. Shi, S. Tongay, J. Wu, F. Wang, *Phys. Rev. B* **95**, 165417 (2017)
- [110] T.M.G. Mohiuddin, A. Lombardo, R.R. Nair, A. Bonetti, G. Savini, R. Jalil, N. Bonini, D.M. Basko, C. Galiotis, N. Marzari, K.S. Novoselov, A.K. Geim, A.C. Ferrari, *Phys. Rev. B* **79**, 205433 (2009)
- [111] M. Huang, H. Yan, C. Chen, D. Song, T.F. Heinz, J. Hone, *Proceedings of the National Academy of Sciences* **106**(18), 7304 (2009)
- [112] O. Frank, G. Tsoukleri, J. Parthenios, K. Papagelis, I. Riaz, R. Jalil, K.S. Novoselov, C. Galiotis, *ACS Nano* **4**(6), 3131 (2010), pMID: 20496881
- [113] J. Visser, E.R. Eliel, G. Nienhuis, *Phys. Rev. A* **66**, 033814 (2002)
- [114] T. Higuchi, N. Kanda, H. Tamaru, M. Kuwata-Gonokami, *Phys. Rev. Lett.* **106**, 047401 (2011)
- [115] P. Ayria, A.R.T. Nugraha, E.H. Hasdeo, T.R. Czank, S.i. Tanaka, R. Saito, *Phys. Rev. B* **92**, 195148 (2015)
- [116] J.J. Sakurai, *Modern Quantum Mechanics, 2nd ed.* (Addison-Wesley: Boston, MA, 2011)
- [117] P. Giannozzi, S. Baroni, N. Bonini, M. Calandra, R. Car, C. Cavazzoni, D. Ceresoli, G.L. Chiarotti, M. Cococcioni, I. Dabo, A.D. Corso, S. de Gironcoli, S. Fabris, G. Fratesi, R. Gebauer, U. Gerstmann, C. Gougoussis, A. Kokalj, M. Lazzeri, L. Martin-Samos, N. Marzari, F. Mauri, R. Mazzarello, S. Paolini, A. Pasquarello, L. Paulatto, C. Sbraccia, S. Scandolo, G. Sclauzero, A.P. Seitsonen, A. Smogunov, P. Umari, R.M. Wentzcovitch, *J. Phys.: Condens. Matter* **21**(39), 395502 (2009)
- [118] J.P. Perdew, K. Burke, M. Ernzerhof, *Phys. Rev. Lett.* **77**, 3865 (1996)

- [119] B.R. Carvalho, L.M. Malard, J.M. Alves, C. Fantini, M.A. Pimenta, *Phys. Rev. Lett.* **114**, 136403 (2015)